Improved Detailing in Steel Bridges to Prevent Constraint-Induced Fracture

By

Caroline Bennett, Ph.D., P.E.

William Collins, Ph.D., P.E.

Jaswant Cobos

A Report on Research Sponsored by
The Federal Highway Administration

Structural Engineering and Engineering Materials
SM Report No. 169
December 2025

THE UNIVERSITY OF KANSAS CENTER FOR RESEARCH, INC.

2385 Irving Hill Road – Campus West, Lawrence, Kansas 66045

TECHNICAL REPORT DOCUMENTATION PAGE

1. Report No. SM Report No. 169	2. Government Accession No.	3. Recipient's Catalog No.
4. Title and Subtitle Improved Detailing in Steel Bridges to Prevent Constraint-Induced Fracture		5. Report Date 12/19/2025 6. Performing Organization Code:
7. Author(s) Caroline R. Bennett (ORCID: 0000-0002-2713-0011) William N. Collins (ORCID: 0000-0002-2835-6389) Jaswant I. Cobos (ORCID: 0009-0001-1843-2499)		8. Performing Organization Report No.
9. Performing Organization Name and Address The University of Kansas Center for Research, Inc. 2385 Irving Hill Rd. Lawrence, KS 66045		10. Work Unit No. 11. Contract or Grant No. 693JJ321C000026
12. Sponsoring Agency Name and Address Office of Bridges and Structures Federal Highway Administration 1200 New Jersey Ave SE Washington, DC 20590		13. Type of Report and Period Final Report, September 2021 – December 2025 14. Sponsoring Agency Code
15. Supplementary Notes		

16. Abstract

This report describes an investigation focused on characterizing the phenomenon of constraint-induced fracture (CIF) in steel bridges, specifically considering three classes of details which prior research has not adequately addressed: thick bearing stiffeners, connection plates, and orthogonal stiffeners with varying constraint-relief gap dimensions. The research approach taken in the study included a suite of nonlinear parametric finite element models. To close knowledge gaps regarding the risk of CIF at in existing bridges and new designs, the influence of the following variables were considered: web thicknesses, gap dimensions, stiffener thickness, and in some cases, out-of-plane loading. A series of analyses were conducted to assess CIF susceptibility of the following details: a discontinuous stiffener interrupted by an orthogonal continuous stiffener, and a connection plate continuously welded into the flange/web junction. The modeling effort focused on computation of triaxiality factors to quantify the level of constraint at the details studied, and to compare across the modeling suite.

A series of 16 large-scale tension tests were conducted, in which steel dogbone specimens with welded attachments representing thick bearing stiffeners, connection plates, and orthogonal stiffeners with varying constraint-relief gap dimensions were loaded to failure. The test program captured a range of variables, including detail type, plate thicknesses, gap dimensions, test temperature, inclusion of out-of-plane loading, and steel material properties. Fourteen specimens were tested at low temperatures (LT), and two were tested at room temperature (RT). Each tested specimen was also evaluated using a finite element model executed at the experimentally observed maximum load to enable consideration of triaxiality factors against real observations of fracture.

17. Key Words Steel bridges; constraint-induced fracture; fracture	18. Distribution Statement No restrictions. This document is available to the public through the National Technical Information Service, Springfield, VA 22161. http://www.ntis.gov		
19. Security Classif. (of this report) Unclassified	20. Security Classif. (of this page) Unclassified	21. No. of Pages 134	22. Price

Form DOT F 1700.7 (8-72) Reproduction of completed page authorized.

SI* (MODERN METRIC) CONVERSION FACTORS

APPROXIMATE CONVERSIONS TO SI UNITS

Symbol	When You Know	Multiply By	To Find	Symbol
		LENGTH		
in	inches	25.4	millimeters	mm
ft	feet	0.305	meters	m
yd	yards	0.914	meters	m
mi	miles	1.61	kilometers	km
		AREA		
in^2	square inches	645.2	square millimeters	mm^2
ft^2	square feet	0.093	square meters	m^2
yd^2	square yard	0.836	square meters	m^2
ac	acres	0.405	hectares	ha
mi^2	square miles	2.59	square kilometers	km^2
		VOLUME		
fl oz	fluid ounces	29.57	milliliters	mL
gal	gallons	3.785	liters	L
ft^3	cubic feet	0.028	cubic meters	m^3
yd^3	cubic yards	0.765	cubic meters	m^3
	NOTE: volumes greater than 1000 L shall be shown in m^3			
		MASS		
oz	ounces	28.35	grams	g
lb	pounds	0.454	kilograms	kg
T	short tons (2000 lb)	0.907	megagrams (or "metric ton")	Mg (or "t")
		TEMPERATURE (exact degrees)		
°F	Fahrenheit	5 (F-32)/9 or (F-32)/1.8	Celsius	°C
		ILLUMINATION		
fc	foot-candles	10.76	lux	lx
fl	foot-Lamberts	3.426	$candela/m^2$	cd/m^2
		FORCE and PRESSURE or STRESS		
lbf	poundforce	4.45	newtons	N
lbf/in^2	poundforce per square inch	6.89	kilopascals	kPa

APPROXIMATE CONVERSIONS FROM SI UNITS

Symbol	When You Know	Multiply By	To Find	Symbol
		LENGTH		
mm	millimeters	0.039	inches	in
m	meters	3.28	feet	ft
m	meters	1.09	yards	yd
km	kilometers	0.621	miles	mi
		AREA		
mm^2	square millimeters	0.0016	square inches	in^2
m^2	square meters	10.764	square feet	ft^2
m^2	square meters	1.195	square yards	yd^2
ha	hectares	2.47	acres	ac
km^2	square kilometers	0.386	square miles	mi^2
		VOLUME		
mL	milliliters	0.034	fluid ounces	fl oz
L	liters	0.264	gallons	gal
m^3	cubic meters	35.314	cubic feet	ft^3
m^3	cubic meters	1.307	cubic yards	yd^3
		MASS		
g	grams	0.035	ounces	oz
kg	kilograms	2.202	pounds	lb
Mg (or "t")	megagrams (or "metric ton")	1.103	short tons (2000 lb)	T
		TEMPERATURE (exact degrees)		
°C	Celsius	1.8C+32	Fahrenheit	°F
		ILLUMINATION		
lx	lux	0.0929	foot-candles	fc
cd/m^2	$candela/m^2$	0.2919	foot-Lamberts	fl
		FORCE and PRESSURE or STRESS		
N	newtons	0.225	poundforce	lbf
kPa	kilopascals	0.145	poundforce per square inch	lbf/in^2

TABLE OF CONTENTS

LIST OF FIGURES

LIST OF TABLES

LIST OF ABBREVIATIONS

AASHTO	American Association of State Highway and Transportation Official
ASTM	American Society for Testing and Materials
BDS	Bridge Design Specification
BS	bearing stiffener
CIF	constraint-induced fracture
CP	connection plate
CRG	constraint-relief gap
CVN	Charpy V-notch
DIC	digital image correlation
DLS	discontinuous longitudinal stiffener
DTS	discontinuous transverse stiffener
F	Fahrenheit
FEA	finite element analysis
ft	foot; feet
FHWA	Federal Highway Administration
kip	kilopound
ksi	kilopounds per square inch
KU	University of Kansas
LT	low temperature
L-T	longitudinal-transverse fracture orientation
LRFD	load and resistance factor design
MBE	Manual of Bridge Evaluation
MST	minimum service temperature
min	minute(s)
MTR	material test report
NHI	National Highway Institute
OOP	out-of-plane
RT	room temperature
s	second(s)

LIST OF SYMBOLS

E	Young's modulus / elastic modulus
e_L	Assumed elongation percentage
F_{brace}	Out-of-plane brace force
F_u	Ultimate tensile strength
F_y	Yield strength
h_{gap}	Constraint-relief gap dimension
n	Strain hardening exponent
O_s	Assumed offset for 0.2% offset method
P	Load or Force
$P_{fracture}$	Load at fracture
P_y / P_{yield}	Nominal yield strength of the specimen
S_{tu}	Material ultimate strength
S_{ty}	Tensile yield strength
T_1, T_2	Triaxiality Factors
t_{bf}	Bottom flange thickness
t_{ls}	Longitudinal stiffener thickness
t_{tf}	Top flange thickness
t_{ts}	Transverse stiffener thickness
t_w	Web thickness
ε	Strain
ε_1	Strain in the longitudinal direction
ε_{tr}	True strain
σ	Stress
σ_1, σ_2, σ_3	Principal stresses
σ_{eff}	von Mises stress
σ_E	Engineering stress
$\sigma_{hydrostatic}$	Average of principal stresses (hydrostatic stress)
σ_{tr}	True stress
σ_{ult}	Ultimate tensile strength
σ_y	Yield strength

ACKNOWLEDGEMENTS

The authors gratefully acknowledge the technical guidance provided by Federal Highway Administration staff and the support of the participating fabricator and University of Kansas laboratory staff. The authors also gratefully acknowledge input provided by Mr. Domenic Coletti and Mr. Duncan Paterson, who served as advisers to the project. The contents of this report reflect the views of the authors, who are responsible for the facts and accuracy of the data presented herein.

CHAPTER 1 - EXECUTIVE SUMMARY

This report describes an analytical and experimental investigation focused on characterizing the phenomenon of constraint-induced fracture in steel bridges, specifically considering three classes of details which prior research has not adequately addressed: thick bearing stiffeners, connection plates, and orthogonal stiffeners with varying constraint-relief gap dimensions.

The research approach taken in the study included a suite of nonlinear parametric finite element models. To close knowledge gaps regarding the risk of CIF at attachments (transverse stiffeners, connection plates, bearing stiffeners, and longitudinal stiffeners) in existing bridges and new designs, the influence of the following variables were considered: web thicknesses, gap dimensions, and stiffener thickness. To characterize the performance of stiffeners and connection plates subjected to out-of-plane loading where no cope is present between the stiffener and the flange-to-web weld, the influence of varying levels of out-of-plane loads was also considered. A series of analyses were conducted to assess CIF susceptibility of the following details: a discontinuous stiffener interrupted by an orthogonal continuous stiffener, and a connection plate continuously welded into the flange/web junction. The modeling effort focused on computation of triaxiality factors to quantify the level of constraint at the details studied, and to compare across the modeling suite.

A series of 16 large-scale experimental tension tests were conducted, in which steel dogbone specimens with welded attachments representing thick bearing stiffeners, connection plates, and orthogonal stiffeners with varying constraint-relief gap dimensions were loaded to failure. The test program captured a range of variables, including detail type, plate thicknesses, gap dimensions, test temperature, inclusion of out-of-plane loading, and steel material properties. Fourteen specimens were tested at low temperatures (LT), and two were tested at room temperature (RT). The orthogonal stiffener specimens were subjected to longitudinal tension, applied parallel to the long axis of the dogbones. The bearing stiffener and connection plate specimens were additionally subjected to a constant out-of-plane (OOP) tension force while the primary longitudinal tension was applied; this was done to mimic the presence of cross-frame forces acting laterally on the detail. Each tested specimen was also evaluated using a finite element model executed at the experimentally observed maximum load to enable consideration of triaxiality factors against real observations of fracture.

Findings from the analytical and experimental programs indicate clear differences in behavior between the details studied. The discontinuous longitudinal stiffener (DLS) detail demonstrated the highest CIF vulnerability, with all DLS specimens tested experimentally fracturing, including those tested at room temperature. Fracture loads were affected by the presence or absence of a constraint-relief gap. Even small gaps reduced levels of constraint and increased capacity, while zero-gap configurations exhibited high variability and lower average fracture capacity. Discontinuous transverse stiffener (DTS), bearing stiffener (BS), and connection plate (CP) specimens performed robustly in experimental testing. No DTS, BS, or CP specimen fractured during testing, even under combined tension and out-of-plane loading. Parametric finite element (FE) results generally corroborated these trends.

The research supports several actionable suggestions for assessment of steel bridges and detailing practices. A minimum constraint-relief gap of $^1/_4$ inch is suggested for existing details with discontinuous longitudinal attachments, based on experimental performance and analytical reductions in triaxiality relative to zero-gap configurations. The research also supports adoption of the updated connection plate detail wherein the CP is welded into the junction of the flange and web.

CHAPTER 2 - OVERVIEW AND PROJECT INTRODUCTION

2.1 CONSTRAINT-INDUCED FRACTURE (CIF)

Steel bridges rely on a wide variety of connection details between girder members, stiffeners, and attachments. The specific geometric details can have a large effect on both fatigue and fracture performance. Fatigue performance is related to the severity of stress concentrations from detail geometry, stress range, presence of discontinuities, and other material and loading factors. Fracture performance is typically thought of as a function of material resistance to fracture (fracture toughness), size of discontinuities, and local net tensile stress.

However, it is critical to also consider the influence of constraint on fracture susceptibility. The ability of material to deform under shear stresses dictates its ability to yield. Without that ability, a state of triaxial stress can develop in the material, preventing shear yielding. As a result, local stresses can exceed the material's yield strength and approach the material's tensile strength with little to no deformation until brittle fracture occurs. This occurrence is often referred to as constraint-induced fracture (CIF), a term that can legitimately cause some confusion given that *any* fracture can only occur in the presence of constraint. 'Constraint-induced fracture' is typically used to refer to fractures that can be traced to detailing practices, rather than solely a thickness effect.

Coletti et al. (2021), adopted the following terminology for CIF from Russo et al. (2016b):

> *Constraint-induced fracture (CIF)*: A type of fracture attributed to local constraint conditions in steel under tension, which may occur at details of certain geometries.

2.2 INTERSECTING WELDS AND CONSTRAINT-RELIEF GAPS

The Hoan Bridge in Milwaukee, WS, failure on December 13, 2000, is a classic example of CIF, wherein three girders of the bridge fractured with no evidence of prior fatigue crack development. The failure in the Hoan Bridge initiated at a lateral brace gusset detail that included a slot to accommodate an orthogonal connection plate. The detail resulted in a high level of stress triaxiality due to: a high level of constraint limiting the ability of the web to yield; high tensile stresses from applied loads and welding residual stresses; and a high stress concentration and a crack-like plane of discontinuity perpendicular to the primary flow of tensile stress at the constraint-relief gap between weld toes (Coletti et al., 2021).

In the years since the Hoan fracture, there was a concern that the use of intersecting welds led to an increased susceptibility to CIF, resulting in a hesitancy to use intersecting welds in structural detailing. However, this concern has been over-generalized and somewhat misplaced. Intersecting welds have not been the cause of CIF per se, since some details have been designed in such a way that has not allowed for localized material deformation, resulting in CIF. Structural attachments require careful detailing to avoid CIF when there are multiple orthogonally-oriented elements placed close together, and this scenario often presents itself in the context of stiffener elements (longitudinal, transverse, bearing, connection plates), particularly where intersecting stiffener elements exist.

A major point of emphasis in Coletti et al. (2021) aimed to distinguish between "intersecting welds" and "constraint resulting from the intersection of welded structural elements," to clarify confusion around the topic of intersecting welds that has existed in the industry since the Hoan Bridge fracture. Coletti et al. adopted the following terminology for intersecting welds:

> *Intersecting welds*: "Welds that run across each other, overlap, or touch."

Existing practice for minimum constraint-relief gap (CRG) dimensions are somewhat contradictory and are based on sparse research. The terminology adopted from Coletti et al. for constraint-relief gap is:

Constraint-relief gap (CRG): "An interruption, of sufficient size, provided in a welded structural element, or its connection to a constrained element, to provide localized relief from constraint induced by that element on a constrained element to which it is attached, so that local yielding can occur. The dimension describing the constraint-relief gap is measured between the toes and or ends of the welds attaching the constraining element to the connected, constrained element."

An often cited reference is a study conducted by Mahmoud et al. (2005) that suggests a minimum dimension for constraint relief gaps of ¼ inch, however, the underlying work is based on a limited finite element model, wherein various gap dimensions were not explicitly studied. Other documents have established different limits, ranging from a minimum of ½ inch in the AASHTO Bridge Design Specifications (BDS) (AASHTO, 2017), to a suggested 1 inch in the FHWA/NHI Course on Design and Evaluation of Steel Bridges for Fatigue & Fracture (Russo et al., 2016b). The latter suggestions are loosely based on the research performed by Mahmoud et al. (2005), empirically adjusted to provide adequate constraint relief between intersecting elements without producing perceived distortional problems.

The Federal Highway Administration (FHWA) commissioned a study on the evaluation of steel bridge details for risk of constraint-induced fracture, which established a framework for evaluating susceptibility to CIF based on the presence of (1) net tensile stress, (2) planar discontinuities perpendicular to the direction of primary stress, and (3) triaxial constraint (Coletti et al., 2021). However, there remain structural details for which CIF susceptibility is not currently understood or characterized. Some such details are already in use in steel bridges and have experienced failures that have not been adequately characterized with respect to the role of CIF; thick bearing stiffeners are an important example (Fig. 1a). There also remain questions that have been under-studied regarding the necessary gap dimensions that should be addressed for details in existing bridges (Fig. 1b). Finally, other details *not* yet being used in steel bridges present attractive features, such as transverse stiffeners and connection plates detailed without a cope (shown in Fig 2b in comparison with the traditional detail in Fig 2a); however, concern regarding susceptibility to CIF stands as a barrier to its use.

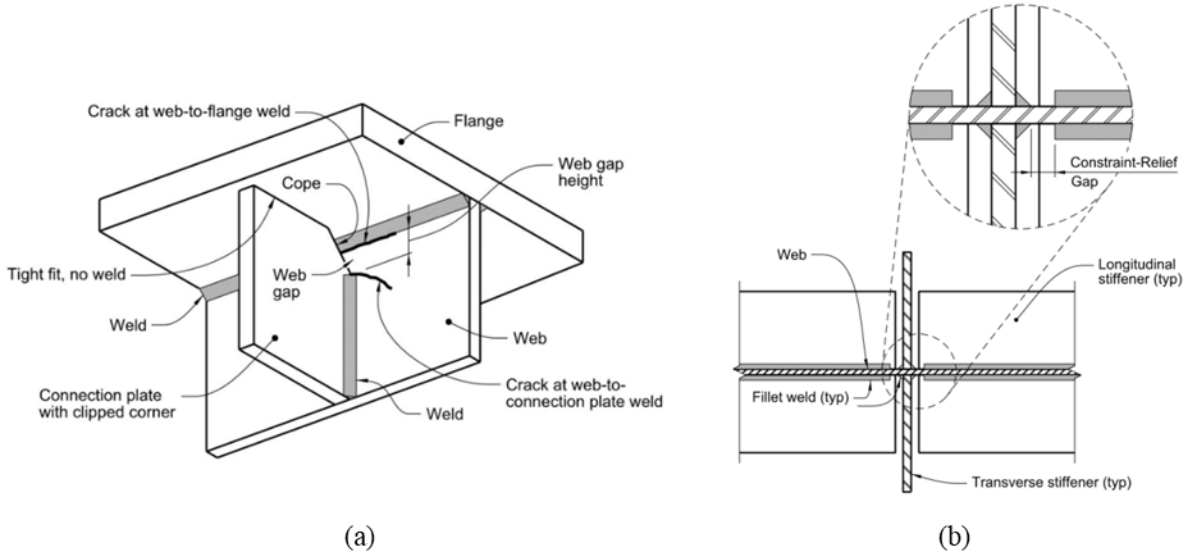

Source: FHWA.

Figure 1. Illustration. (a) Cracking at thick bearing stiffener / connection plate; (b) Constraint-relief gap at a discontinuous longitudinal stiffener.

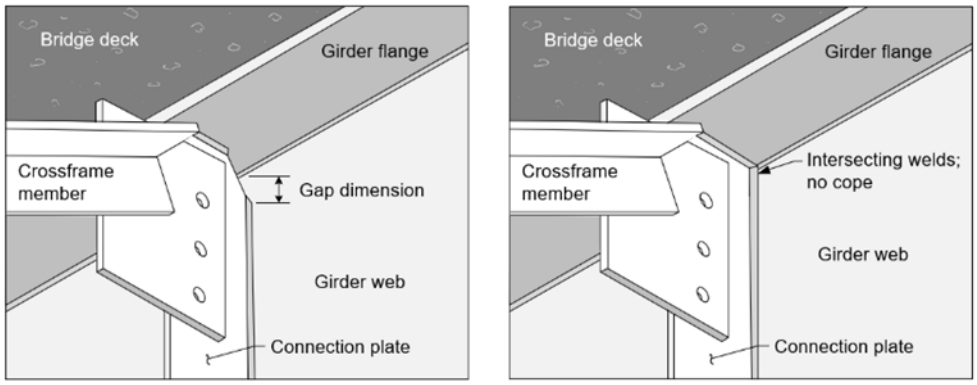

Source: FHWA.

Figure 2. Illustration. (a) Traditional connection plate detailing with a gap; (b) Alternative detailing with intersecting welds and no cope.

2.3 PROJECT OBJECTIVE

The objective of the research was to characterize the susceptibility of structural stiffener details in steel bridges to constraint-induced fracture, for cases in which behavior is not yet well-understood, including: (1) thick bearing stiffeners; (2) different constraint-relief gap distances between intersecting structural components; and (3) continuous welding at the intersection of the flange-web-connection plate.

CHAPTER 3 - BACKGROUND

3.1 APPROACH

The FHWA titled report "Evaluation of Steel Bridge Details for Susceptibility to Constraint-Induced Fracture" (Coletti et al., 2021) summarizes the state-of-the-art understanding of constraint-induced fracture (CIF) in steel bridges and provides a framework for evaluation of details in steel bridges for susceptibility to constraint-induced fracture. The current state of knowledge described and summarized in the Coletti et al. (2021) report was based on a literature review of published research, various owner agency and industry practice documents, review of current practices, and a full day meeting of the panel of experts (representatives from academia, design, fabricators, and owners.). Coletti et al. (2021) provides a description of stress triaxiality, constraint, and susceptibility to constraint-induced fracture; a review of engineering practices including examples of constraint-induced fractures in steel bridges; a detailed framework for evaluating details for susceptibility to constraint-induced fracture, with examples; and a discussion of measures to mitigate elevated susceptibility to constraint-induced fracture.

Coletti et al. (2021) describe a framework for evaluating susceptibility to CIF that is based on elevated susceptibility of steel bridges to CIF being dependent upon three conditions as shown in Figure 3:

- Presence of a high net tensile stress,
- A high degree of constraint, and
- Planar discontinuities approximately perpendicular to the primary flow of tensile stress

Of the three conditions described, evaluating the level of constraint in a particular detail is arguably the most challenging.

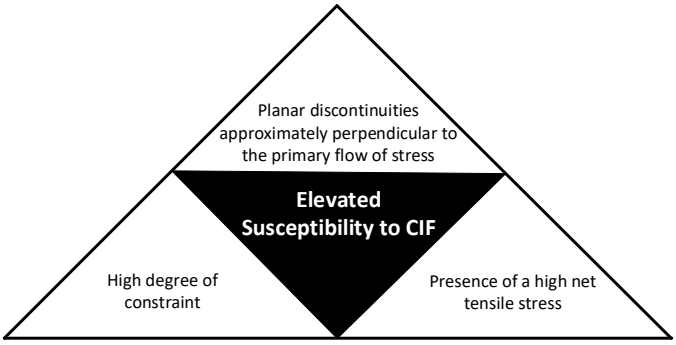

Source: FHWA.

Figure 3. Illustration. Factors contributing to elevated susceptibility to CIF.

Coletti et al. (2021) presented the need for the research around the topic of CIF in steel bridges. The research reported herein was aimed at addressing some of those research gaps. This literature review, therefore, is aimed at highlighting topics that specifically underpin the research effort at hand, and attempts to not be unnecessarily repetitive with detailed content available in Coletti et al. (2021).

3.2 EXAMPLES OF CIF IN STEEL BRIDGES

The Hoan bridge failure (Milwaukee, WI) is the most well-known example of CIF. The Hoan Bridge was opened in 1974, and in 2000 all three girders on an approach span of the bridge fractured with no evidence of prior fatigue crack development. Two girders experienced full-depth fracture through the flanges, while fracture of the third girder arrested at the web-to-flange intersection prior to complete fracture. Previous

inspections had identified smaller cracks at other locations on the bridge, presumed at the time to be fatigue cracks. Further investigations following the large fracture event indicate these previous cracks were also CIF that arrested prior to full-depth failure (Cooper, 2001). The failure in the Hoan Bridge initiated at a lateral brace gusset detail that included a slot to accommodate an orthogonal connection plate. The detail resulted in a high level of stress triaxiality due to: a high level of constraint limiting the ability of the web to yield; high tensile stresses from applied loads and welding residual stresses; and a high stress concentration and a crack-like plane of discontinuity perpendicular to the primary flow of tensile stress at the constraint-relief gap between weld toes (Coletti et al., 2021). A small $^1/_8$-inch-wide CRG was present in the detail (Cooper, 2001).

Other important examples of CIF have occurred over the past few decades. The bridge carrying US 422 over the Schuylkill River in Pennsylvania (opened in 1965) experienced a fracture due to CIF in 2003. The failure initiated in one of the two main bridge members at the junction of the web, a lateral gusset plate, and transverse connection plate, near the bottom flange of the girder (Connnor et al., 2007), and appeared to occur nearly simultaneously at two different locations at the lateral connection plate. No evidence of fatigue cracking was noted before the fracture, and the steel met AASHTO Zone 2 fracture-critical toughness requirements.

The Diefenbaker Bridge in Saskatchewan, Canada experienced a full-depth failure due to CIF at a similar detail in 2011 (Ellis et al., 2013), as did the bridge carrying I-64 over the Blue River in Harrison County, Indiana in 1994 (Bowman, 2002).

While the preceding examples were cases in which CIF occurred at a lateral gusset and transverse stiffener detail, there have also been cases of fracture occurring in other details, including bearing stiffeners used as connection plate elements (Fisher & Kaufmann, 2010; Hodgson et al., 2018). In both cases, fracture occurred at a bearing stiffener being used as a connection plate where the stiffener was not welded to the flange. It is theorized that these fractures represent cases of CIF as well.

A detailed synthesis of CIF case studies in steel bridges is provided in Coletti et al. (2021). A review of that synthesis, as well as supplementary materials (e.g., drawings and photographs) relevant to the failures discussed above, was conducted. Particular quantities of interest included web thickness, stiffener thickness, and grade of material, as summarized in Table 3-2.

Table 3-1. Summary of key parameters from instances of CIF at shelf plate details in steel bridges.

Case Study	*CRG or Gap Dimension*	*Plate Thicknesses*	*Notes*
Hoan Bridge	$^1/_8$ inch	$^1/_2$-inch web, $^3/_4$-inch gusset plate	Fracture initiated at a small ($^1/_8$-inch) gap at a lateral brace gusset plate, cross-frame connection plate, and girder web intersection.
US 422 Schuylkill River Bridge	—	$^7/_{16}$-inch web, $1^1/_4$-inch bottom flange	Fracture occurred in bottom flange, initiating at the intersection of a lateral bracing connection plate, cross-frame connection plate, and web.
Diefenbaker Bridge	$^1/_{16}$ inch	—	Fracture initiated at the intersection of lateral gusset plate, cross-frame connection plate, and girder web.

— *Represents data that is unknown*

Table 3-2. Summary of key parameters from instances of CIF at bearing stiffener details in steel bridges

Case Study	*CRG or Gap Dimension*	*Plate Thicknesses*	*Notes*
Cedar River Bridge	$^3/_8$ inch	$^7/_{16}$-inch web, $^{13}/_{16}$-inch bearing stiffener	Fracture occurred at bearing stiffener not welded to top flange, in the web gap.
IA-926 (Des Moines River Bridge)	$^5/_8$ inch	$^5/_8$-inch web, 2-inch top flange	Fracture occurred in top flange above a bearing stiffener.
Norman Wood Bridge	$^1/_8$ inch min.	$^1/_2$-inch web, $^7/_8$-inch bearing stiffeners	Fracture occurred at bearing stiffener over a pier. Bearing stiffener was not welded to top flange, and fracture initiated in the web gap.
IA-150 Volga River Bridge	—	$^7/_{16}$-inch web, $^7/_8$-inch bearing stiffeners	Fracture occurred in web gap at a bearing stiffener over a pier, at junction of stiffener and top flange. Stiffener was detailed as 'close fit' to flange.

— *Represents data that is unknown*

3.3 TRIAXIALITY AND CONSTRAINT-INDUCED FRACTURE

Schafer et al. (2000) is an important source of information that describes a manner in which susceptibility to constraint-induced fracture can be explored and quantified through nonlinear finite element analysis (FEA). Schafer et al. (2000) describes two triaxiality factors for a ductile metal, T_1 and T_2, calculated as follows:

$$T_1 = \frac{\sigma_{hydrostatic}}{\sigma_{eff}} \quad \textbf{Eq. 1}$$

$$T_2 = \frac{\sigma_1}{\sigma_{eff}} = \frac{\sigma_{max}}{\sigma_{eff}} \quad \textbf{Eq. 2}$$

$$\sigma_{hydrostatic} = \frac{\sigma_1+\sigma_2+\sigma_3}{3} \quad \textbf{Eq. 3}$$

$$\sigma_{eff} = \sqrt{\frac{1}{2}}\sqrt{(\sigma_1-\sigma_2)^2+(\sigma_2-\sigma_3)^2+(\sigma_1-\sigma_3)^2} \quad \textbf{Eq. 4}$$

Where σ_1, σ_2, and σ_3 are the principal stresses acting on an element, $\sigma_{hydrostatic}$ is the average of the principal stresses acting on an element, and σ_{eff} is the von Mises stress.

Schafer et al. (2000) provide a useful summary describing when elements are subjected to multiaxial states of stress that material yielding behavior is different than how engineers are often accustomed to considering it, which is under a uniaxial tension load. Triaxiality factors T_1 and T_2 help to describe a state of stress under multiaxial loading normalized against the von Mises yield stress (Table 3-3). Additionally, Coletti et al. (2021) provide a detailed exposition of various states of multiaxial stress rooted in the context of Mohr's Circle.

Table 3-3. Triaxiality factors T_1 and T_2 for various states of stress.

State of Stress	T_1	T_2
Pure Shear	0	0.58
Uniaxial Tension ($\sigma_1=\sigma$; $\sigma_2=\sigma_3=0$)	0.33	1.0
Biaxial Tension ($\sigma_1=\sigma_2=\sigma$; $\sigma_3=0$)	0.67	1.0
Triaxial Tension ($\sigma_1=\sigma_2=\sigma_3=\sigma$)	lim = ∞	lim = ∞

Schafer et al. (2000) make a case that since cleavage fracture is related to the presence of high-magnitude principal stresses, the likelihood for cleavage fracture to occur is directly related to high values of T_2, particularly where $T_2 > 1.0$. The conclusions of their research are supported on the basis of T_2 and maximum principal stress; while T_1 is described in the beginning of the paper, it is not directly used to formulate conclusions. They also describe how triaxiality changes with plasticity, and finite element models should be three-dimensional and include nonlinear material properties. They make note of the influence of different materials may have on constraint and triaxiality when two adjacent parts possess different material stress-strain properties.

Coletti et al. (2021) note that T_2 is particularly helpful in evaluating the susceptibility of a detail to CIF, and that a T_2 greater than the ratio of a material's uniaxial ultimate tensile strength to yield strength (F_u/F_y) indicates a situation wherein the material may fracture at an applied stress less than the stress the material would otherwise be expected to yield.

3.4 PRIOR ANALYTICAL RESEARCH ON CONSTRAINT-INDUCED FRACTURE

Mahmoud et al. (2005) is of particular note in this literature review because it has been often referenced in other sources in establishing criteria for CRG dimensions in steel bridge details.

Mahmoud et al. describe a 3D finite element modeling effort aimed at investigating the role of triaxiality on fracture in a welded connection with similarities to the detail that experienced CIF in the Hoan Bridge.

The detail modeled was a web plate with a vertical stiffener/attachment and a longitudinal attachment. The web plate was restrained at one end, and a tension load was applied to the other end. The web and transverse stiffener were ½ inch thick, and the longitudinal element was ¾ inch thick. The model was executed separately with linear and nonlinear material properties. The analyses were conducted for an applied tension stress of 40 ksi and a CRG width of 0 inches. The material properties used within the nonlinear analysis were determined by a true stress-strain relationship and an approximate yield strength of 40 ksi based on material tests of a fractured girder from the Hoan Bridge.

In the nonlinear analyses, the attachments were modeled in succession such that the relative level of constraint in the detail could be studied. With both the vertical stiffener and longitudinal attachment in place, constraint was found to be greatest at the weld toe and directly behind the longitudinal attachment. The authors concluded that high triaxial stresses were present through the thickness of the web, and nonlinear analysis should be conducted rather than linear to properly assess triaxial demand. They called for further research to examine the influence of different web plate thicknesses and gap sizes, as well as the influence of welds.

While the authors did not evaluate different CRG dimensions to assess their significance in reducing susceptibility to CIF, they stated that "*The results of the nonlinear analysis demonstrated that a high constraint detail with a zero-inch web gap has high potential for fracture. A slight increase in the web gap size (1/4") will result in smaller triaxial stresses and less potential for fracture.*"

3.5 STATE-OF-THE-PRACTICE AND CURRENT SUGGESTIONS

The most recent work reviewed was published by Coletti et al. (2021) and their major findings included:

- Steel bridge details that possess intersecting welds are not necessarily at elevated risk of constraint-induced fracture.
- Elevated susceptibility of steel bridges to CIF is dependent upon three conditions: presence of a high net tensile stress, a high degree of constraint, and planar discontinuities approximately perpendicular to the primary flow of tensile stress.
- Evaluating details using methods grounded in a technical understanding of CIF can help bridge owners identify details that are candidates for redesign and retrofit.
- Retrofitting and redesigning details with intersecting welds without proper understanding of CIF can lead owners to adopt design and/or retrofits that may result in poor performance.
- The bridge industry may benefit from clarification on several topics, including improved terms to describe problematic details in steel bridges; the influence of intersecting welds; factors that produce elevated susceptibility to CIF; minimum width for constraint-relief gaps; and education regarding the effectiveness of constraint-relief gaps as well as other measures for reducing susceptibility to CIF.
- Existing practice for the minimum width of constraint-relief gaps in specifications and documents are based on a very limited analytical study that considered only one web thickness and one CRG dimension.
- Lateral connection plates that are connected directly to the girder web can sometimes be correlated with an elevated susceptibility to CIF; they should instead be connected directly to flanges on the girder.
- CIF concerns related to thick bearing stiffeners at interior supports of steel bridges remain unresolved.
- Corrosion performance at transverse stiffener details can be improved by using seal welding and welding the stiffener into the flange-to-web junction. However, for this to be implementable, research is needed regarding CRG dimensions for coped stiffeners, and with regard to susceptibility to CIF when copes are not present.

The report also included three important suggestions for future research, as follows.

1. The first suggestion (§8.2.1 in Coletti et al. (2021)) was that an investigation should be conducted to study the influence of web thickness and CRG size on triaxiality in steel bridge details. The technical literature shows the minimum size of CRGs is inconsistent, ranging from ¼ inch to 1 inch, depending on whether the reader is referencing the AASHTO Bridge Design Specifications, the participant workbook for the FHWA/NHI course on Design and Evaluation of Steel Bridges for Fatigue and Fracture, the Design and Evaluation of Steel Bridges for Fatigue and Fracture-Reference Manual (Russo et al., 2016a), or journal publications by Mahmoud et al. (2005) and Connor et al. (2005). Coletti et al. (2021) suggested that such future research include a study of web thickness, CRG dimensions, and other variations in geometry including stiffener size and orientation. They additionally suggested the inclusion of low temperature fracture experimental testing.
2. The second suggestion (§8.2.2 in Coletti et al. (2021)) was to explore the potential for CIF at large bearing stiffeners at interior supports of steel bridge girders. Coletti et al. (2021) noted multiple cases of fractures that have occurred at large bearing stiffeners over interior supports (Fisher & Kaufmann, 2010; Hodgson et al., 2018), where the bearing stiffeners were also being used as connection plates unattached to the tension flange. The suggestion suggests a focus on influence of residual stresses, load-induced stresses, stress concentrations, and geometric constraint.

3. The third suggestion (§8.2.3 in Coletti et al. (2021)) was to explore the susceptibility of seal-welded details to CIF including seal-welded coped transverse stiffeners, transverse connection plates continuously welded to girder flanges and webs, and bearing stiffeners continuously welded to girder flanges and webs. By seal-welding stiffeners and connection plates, better protection against corrosion may be achieved. However, research is needed to determine whether such detailing practices may detrimentally increase constraint. Additionally, research is needed to determine the acceptable size of the gap between the cope in the corner of the stiffener and flange-to-web weld.

CHAPTER 4 - ANALYTICAL INVESTIGATION

This chapter describes the analytical investigation conducted to characterize the state of triaxiality to quantify susceptibility to constraint-induced fracture in various steel bridge details.

4.1 ANALYTICAL APPROACH

To close knowledge gaps regarding the risk of CIF at attachments (transverse stiffeners, connection plates, bearing stiffeners, and longitudinal stiffeners) in existing bridges and new designs, the influence of the following variables have been considered: web thicknesses, gap dimensions, and stiffener thickness. To characterize the performance of stiffeners and connection plates subjected to out-of-plane loading where no cope is present between the stiffener and the flange-to-web weld, the influence of varying levels of out-of-plane loads are also considered.

A series of analyses were conducted to assess CIF susceptibility of the following details: a discontinuous stiffener interrupted by an orthogonal continuous stiffener, and a connection plate continuously welded into the flange/web junction.

4.1.1 Model Geometry

A 3D finite element model of a girder was developed using the commercially available software package, Abaqus/CAE 2021 Standard. The modeled girder was 100-ft long and was simply supported. The cross-section of the I-shaped girder was comprised of a 16-inch x 1-inch top flange, 20-inch x 2-inch bottom flange, and a 60-inch x $^{5}/_{8}$-inch web. An equivalent concrete deck modeled with steel material properties having cross-sectional dimensions of 16 inches x $6^{3}/_{16}$ inches was attached to the top flange to simulate the contribution of a composite concrete deck, based on 8-ft girder spacing and an 8-inch-thick concrete slab with f'_c=4,000 psi. Figure 4 presents the dimensions for each component of the girder.

Several model construction techniques were explored in detail, including modeling a refined midspan portion of the girder using solid elements and connecting that section to either beam elements or shell-element-constructed parts to generate the end extents of the girder. Ultimately, all models were constructed using quadratic hexahedron solid reduced-integration elements, each with 20 nodes (Abaqus element "C3D20R") throughout the entire girder, as it was found the other element formulations performed poorly under the action of out-of-plane loads.

The flanges, web, and stiffeners of the base model plate girder were created separately and then connected to form the complete geometry of the plate girder finite element model. These connections were made using 3D-element fillet welds which were connected to the cross-section elements using tie constraints. When a tie constraint is used between two surfaces of two parts, those parts deform as a single integrated unit. Fillet welds were meshed using quadratic tetrahedrons, each with 10 nodes (Abaqus element "C3D10"). In the portions of the FE model away from the refined region of interest at midspan, the entire cross-section was one integrated part, eliminating the need for tie constraints or weld modeling.

To prevent lateral torsional buckling, the girder model was restrained against out-of-plane translation along the length of the top flange, equivalent deck, and bottom flange. A uniform downward 0.0305-ksi load was applied to the full width of the top flange along the length of the girder to produce a tensile stress of $0.55F_y$ at the bottom of the bottom flange. The tensile stress of $0.55F_y$ was targeted in the finite element models for the practical rationale that it approximately corresponds to the design stress level implicit in the AASHTO Bridge Design Specifications (AASHTO, 2017).

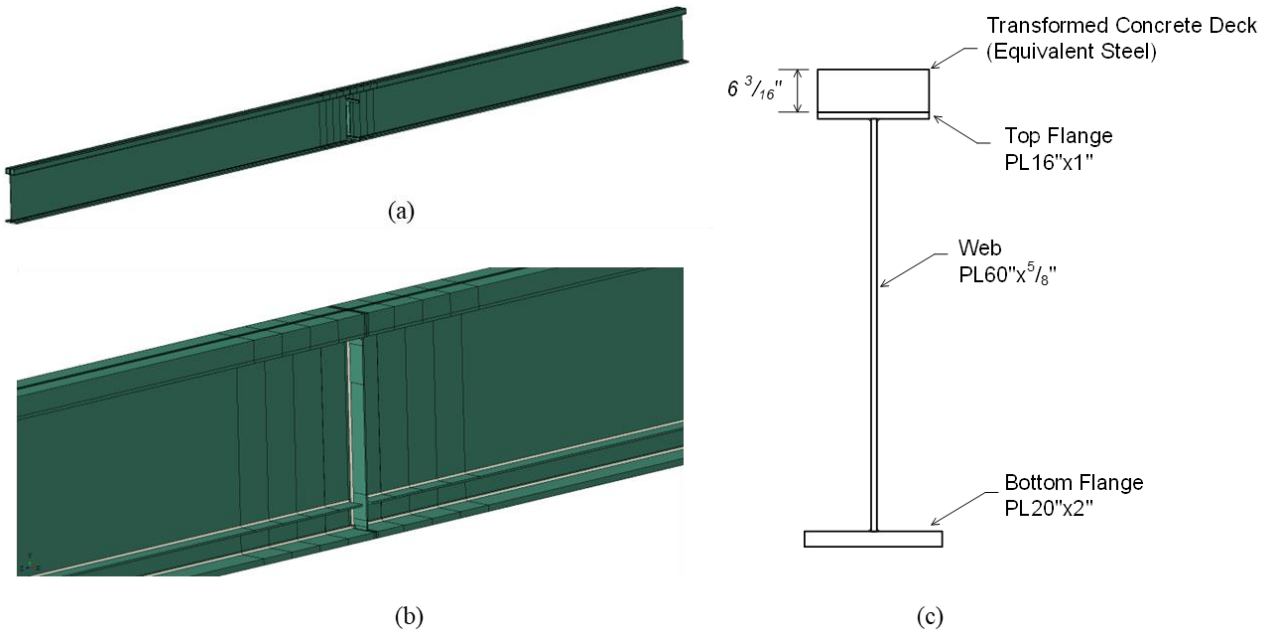

Source: FHWA.

Figure 4. Illustration. Girder model and cross-section: (a) full-length girder model; (b) view of midspan for a detail with orthogonal stiffeners; (c) girder cross-section dimensions.

4.1.1.1 Orthogonal Stiffener Details

The baseline plate girder model was used as a foundation for 29 subsequent parametric plate girder models in which detail classes with orthogonal stiffeners were considered:

1. A discontinuous transverse stiffener (DTS) detail class in which the transverse stiffener is made discontinuous due to a conflict with an orthogonal longitudinal stiffener (Figure 5a), and
2. A discontinuous longitudinal stiffener (DLS) detail class in which the longitudinal stiffener is made discontinuous (Figure 5b).

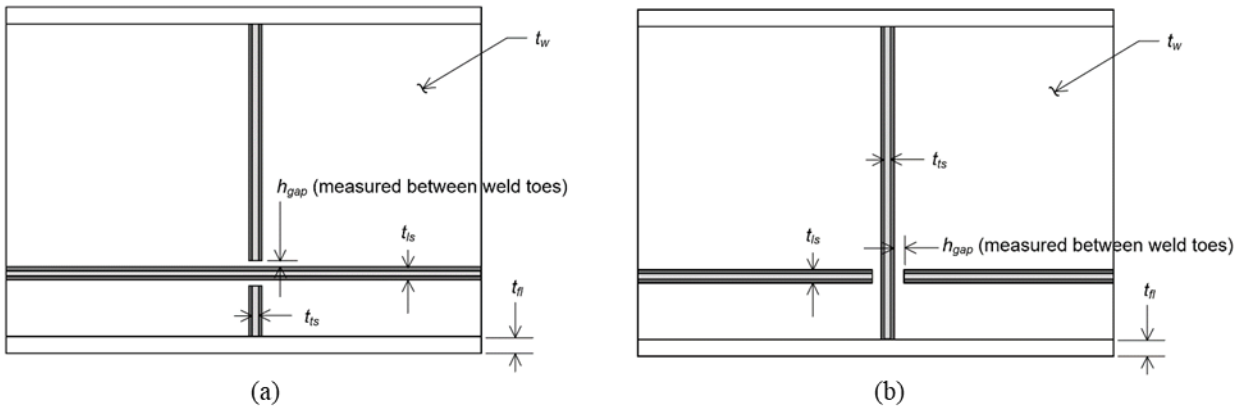

Source: FHWA.

Figure 5. Illustration. Girder segments for orthogonal stiffener models: (a) Discontinuous transverse stiffener; (b) Discontinuous longitudinal stiffener (DLS).

The discontinuous transverse stiffener (DTS) is preferred by the AASHTO BDS (AASHTO, 2017) rather than the discontinuous longitudinal stiffener (DLS) detail. In both cases, the longitudinal stiffener was modeled to extend the entire length of the girder, and the transverse stiffener was attached to the web at midspan.

Table 4-1 describes the 24 parametric models that were developed with discontinuous transverse stiffeners. The models have been named in a specific manner, where each letter in their name represents a parameter and the number to the right of it represents its dimension in sixteenths of an inch. The parameter 'S' denotes the stiffener thickness, 't' denotes web thickness, 'w' denotes the weld size, and 'G' denotes the constraint relief gap size. For instance, "S10t10w4G12" describes a model with $^{10}/_{16}$-inch-thick stiffeners, $^{10}/_{16}$-inch-thick web, $^{4}/_{16}$-inch fillet weld leg, and a constraint-relief gap of $^{12}/_{16}$ inch

Table 4-2 describes the five parametric models with the discontinuous longitudinal stiffener detail. Here the naming convention is based on nominal constraint relief gap size, indicated in sixteenths of an inch. As an example, "GAP16" indicates a model with a constraint-relief gap size of $^{16}/_{16}$ inch.

Table 4-1. Analytical matrix for the discontinuous transverse stiffener (DTS) detail.

Model	CRG, h_{gap} (inch)	Transverse Stiffener Thickness, t_{ts} (inch)	Longitudinal Stiffener Thickness, t_{ls} (inch)	Web Thickness, t_w (inch)	Weld Leg Size, w (inch)
S10t10w4G0	0	$^{5}/_{8}$	$^{5}/_{8}$	$^{5}/_{8}$	$^{1}/_{4}$
S10t10w5G0	0	$^{5}/_{8}$	$^{5}/_{8}$	$^{5}/_{8}$	$^{5}/_{16}$
S10t10w6G0	0	$^{5}/_{8}$	$^{5}/_{8}$	$^{5}/_{8}$	$^{3}/_{8}$
S10t10w4G4	$^{1}/_{4}$	$^{5}/_{8}$	$^{5}/_{8}$	$^{5}/_{8}$	$^{1}/_{4}$
S10t10w5G4	$^{1}/_{4}$	$^{5}/_{8}$	$^{5}/_{8}$	$^{5}/_{8}$	$^{5}/_{16}$
S10t10w6G4	$^{1}/_{4}$	$^{5}/_{8}$	$^{5}/_{8}$	$^{5}/_{8}$	$^{3}/_{8}$
S8t10w4G8	$^{1}/_{2}$	$^{1}/_{2}$	$^{1}/_{2}$	$^{5}/_{8}$	$^{1}/_{4}$
S10t10w4G8	$^{1}/_{2}$	$^{5}/_{8}$	$^{5}/_{8}$	$^{5}/_{8}$	$^{1}/_{4}$
S8t10w5G8	$^{1}/_{2}$	$^{1}/_{2}$	$^{1}/_{2}$	$^{5}/_{8}$	$^{5}/_{16}$
S10t10w5G8	$^{1}/_{2}$	$^{5}/_{8}$	$^{5}/_{8}$	$^{5}/_{8}$	$^{5}/_{16}$
S8t10w6G8	$^{1}/_{2}$	$^{1}/_{2}$	$^{1}/_{2}$	$^{5}/_{8}$	$^{3}/_{8}$
S10t10w6G8	$^{1}/_{2}$	$^{5}/_{8}$	$^{5}/_{8}$	$^{5}/_{8}$	$^{3}/_{8}$
S10t8w4G8	$^{1}/_{2}$	$^{5}/_{8}$	$^{5}/_{8}$	$^{1}/_{2}$	$^{1}/_{4}$
S10t12w4G8	$^{1}/_{2}$	$^{5}/_{8}$	$^{5}/_{8}$	$^{3}/_{4}$	$^{1}/_{4}$
S10t8w5G8	$^{1}/_{2}$	$^{5}/_{8}$	$^{5}/_{8}$	$^{1}/_{2}$	$^{5}/_{16}$
S10t12w5G8	$^{1}/_{2}$	$^{5}/_{8}$	$^{5}/_{8}$	$^{3}/_{4}$	$^{5}/_{16}$
S10t8w6G8	$^{1}/_{2}$	$^{5}/_{8}$	$^{5}/_{8}$	$^{1}/_{2}$	$^{3}/_{8}$
S10t12w6G8	$^{1}/_{2}$	$^{5}/_{8}$	$^{5}/_{8}$	$^{3}/_{4}$	$^{3}/_{8}$
S10t10w4G12	$^{3}/_{4}$	$^{5}/_{8}$	$^{5}/_{8}$	$^{5}/_{8}$	$^{1}/_{4}$
S10t10w5G12	$^{3}/_{4}$	$^{5}/_{8}$	$^{5}/_{8}$	$^{5}/_{8}$	$^{5}/_{16}$
S10t10w6G12	$^{3}/_{4}$	$^{5}/_{8}$	$^{5}/_{8}$	$^{5}/_{8}$	$^{3}/_{8}$
S10t10w4G16	1	$^{5}/_{8}$	$^{5}/_{8}$	$^{5}/_{8}$	$^{1}/_{4}$
S10t10w5G16	1	$^{5}/_{8}$	$^{5}/_{8}$	$^{5}/_{8}$	$^{5}/_{16}$
S10t10w6G16	1	$^{5}/_{8}$	$^{5}/_{8}$	$^{5}/_{8}$	$^{3}/_{8}$

Table 4-2. Analytical matrix for the discontinuous longitudinal stiffener (DLS) detail.

Model	CRG, h_{gap} (inch)	Transverse Stiffener Thickness, t_{ts} (inch)	Longitudinal Stiffener Thickness, t_{ls} (inch)	Web Thickness, t_w (inch)	Weld Leg Size, w (inch)
GAP0	0	5/8	5/8	5/8	5/8
GAP4	1/4	5/8	5/8	5/8	5/8
GAP8	1/2	5/8	5/8	5/8	5/8
GAP12	3/4	5/8	5/8	5/8	5/8
GAP16	1	5/8	5/8	5/8	5/8

The meshing technique is depicted in Figure 6, where the finest mesh size of 1/8 inch is used at the very center of the girder. The mesh size gradually increases to 1/4 inch, 1/2 inch, 1 inch, and then 2 inches, moving away from the region of interest. These mesh sizes were chosen after conducting a mesh sensitivity study, which involved examining the finite element analysis results of a model as a function of the mesh size.

All the models for the orthogonal stiffener details utilized homogenous material between the flanges and web (i.e. a non-hybrid girder).

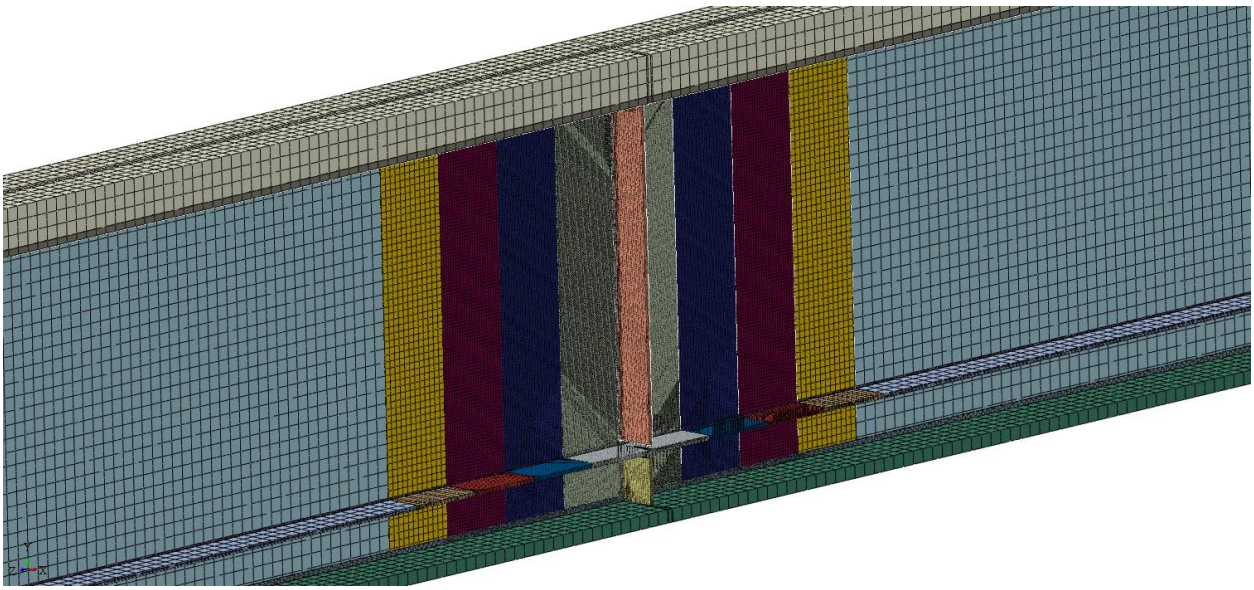

Source: FHWA.

Figure 6. Illustration. Mesh structure used in refined portion of model at mid-span.

4.1.1.2 Connection Plate Details

The baseline plate girder model was used as a foundation for subsequent parametric plate girder models in which detail classes with connection plates (CP) were considered. Three types of detailing practice were investigated:

1. Historic practice: A detail in which the CP is not attached to the flange ($CP_{not\ welded}$), mimicking design practices often used in bridges before the mid-1980s (Figure 7b) wherein engineers often avoiding welding to the tension flange. While CPs were typically welded to the compression flange

in practice, the CP detail was left unattached at both flanges in these models to capture accurate analysis of the unattached detail when considering both positive and negative bending load cases.

2. Current practice: A detail in which the CP is welded to the flange and incorporates a clip ($CP_{clipped}$) (Figure 7c).
3. Newly-proposed practice: A detail in which the CP is minimally clipped and is welded into the corner junction between the flange and web ($CP_{no\ clip}$) (Figure 8).

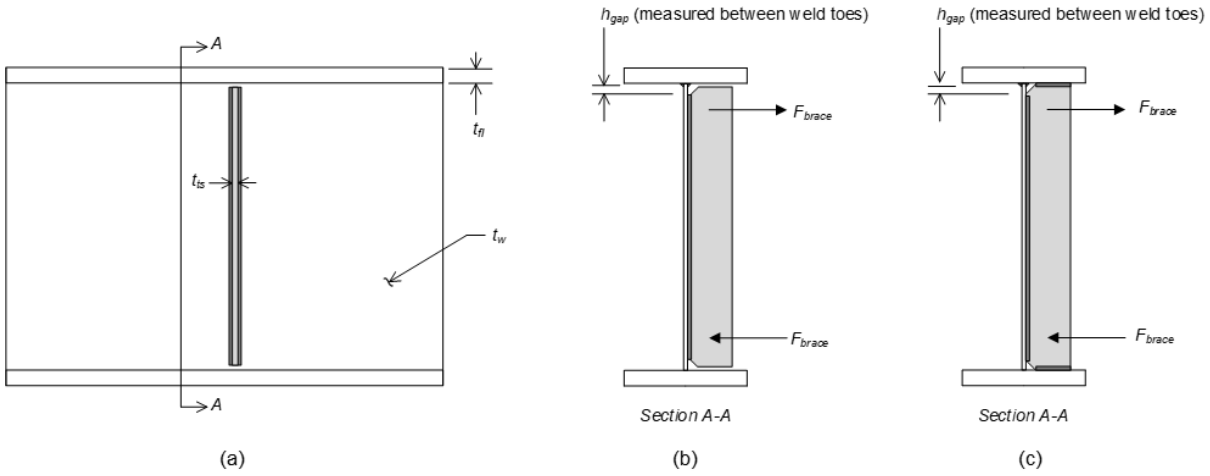

Source: FHWA.

Figure 7. Illustration. Girder detailing practices: (a) Elevation view of girder segment; (b) Models in which CP is not attached to flange ($CP_{not\ welded}$); (c) Models in which CP is welded to the flange and incorporates a clip ($CP_{clipped}$).

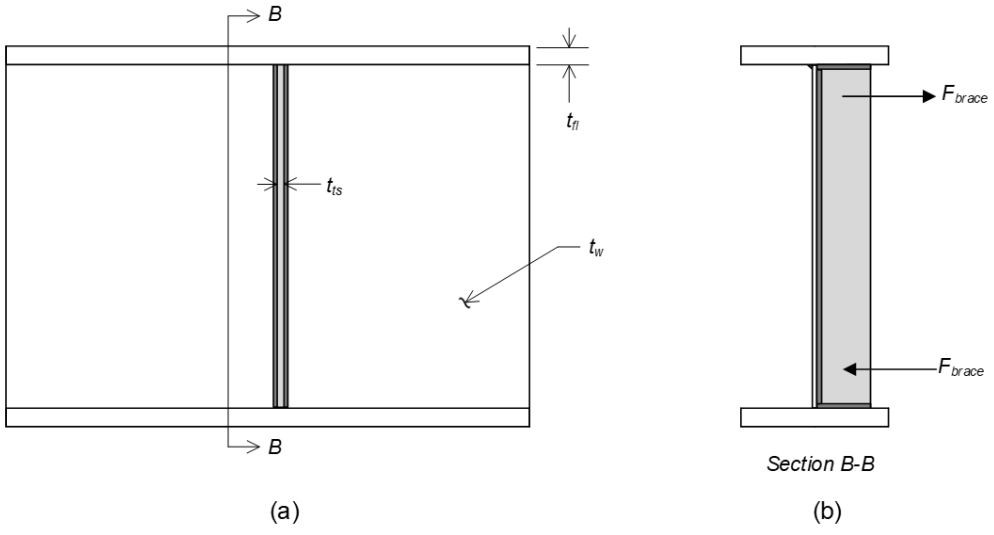

Source: FHWA.

Figure 8. Illustration. Girder detailing practice: (a) Elevation view of girder segment; (b) CP is welded into the corner of the web-to-flange junction, and welds are allowed to intersect ($CP_{no\ clip}$).

Parameters varied in this subtask, detailed in Table 4-3, include the out-of-plane brace force, F_{brace}, web thickness, t_w, weld size, w, grade of material used in the girder flanges, and direction of bending in the girder, for a total of 32 models. Mismatches between materials can have an important influence on the development of constraint, therefore, models included realistic material properties for the welds, which typically have higher strength than the base metal. The material properties for both the girder plate material and weld material were modeled as nonlinear. In addition to a homogeneous girder that utilized grade 50 material in the flanges and web, a hybrid girder was considered for the $CP_{no\ clip}$ case, in which grade 70 flanges were used with a grade 50 web and CP, to consider the case of grade mismatch between the flange, web, and CP elements.

Primary loading cases producing positive bending and negative bending were considered. In both cases, loads were applied at the top flange (downward producing positive bending, and upward producing negative bending). The load applied was such that a stress of $0.55F_y$ was achieved in the tension flange in both cases. For the loading case inducing negative primary bending, the equivalent concrete deck was removed from the top flange, conservatively representing a cracked composite deck. In all models, the connection plate detail girder models were continuously restrained against lateral translation along the entire length of the top flange and the bottom flange to ensure stability. External boundary conditions were applied to the top and bottom flanges and the equivalent deck that restrained out-of-plane translation at every node along those surfaces (i.e., a 1-inch-thick and 100-ft-long surface was restrained against out-of-plane translation on the top flange, a 6.18-inch thick and 100-ft-long surface was restrained against out-of-plane translation on the equivalent deck, and a 2-inch-thick and 100-ft-long surface was restrained against out-of-plane translation on the bottom flange).

For cases in which out-of-plane loads were applied, axial forces were applied near the top and bottom of the connection plate through segments of crossframe members. The out-of-plane forces were located 6 inches below the bottom of the top flange, and 6 inches above the top of the bottom flange. Regardless of the direction of primary bending, the top out-of-plane force was applied horizontally in the direction pointed away from the girder, and the bottom out-of-plane force was applied horizontally in the direction pointed towards the girder.

Table 4-3. Parametric model suite for models with different connection plate details.

Model	Web Thickness, t_w (inch)	Weld Size, w (inch)	CRG Dim., h_{gap} (inch)	Flange Material (ksi)	Out-of-Plane Force, F_{brace} (kips)	Direction Of Primary Bending
CP_{not_welded} 1P	5/8	5/16	1	50	**0**	Positive
CP_{not_welded} 1N	5/8	5/16	1	50	**0**	Negative
CP_{not_welded} 2P	5/8	5/16	1	50	**20**	Positive
CP_{not_welded} 2N	5/8	5/16	1	50	**20**	Negative
CP_{not_welded} 3P	5/8	5/16	1	50	**40**	Positive
CP_{not_welded} 3N	5/8	5/16	1	50	**40**	Negative
$CP_{clipped}$ 1P	5/8	5/16	1	50	**0**	Positive
$CP_{clipped}$ 1N	5/8	5/16	1	50	**0**	Negative
$CP_{clipped}$ 2P	5/8	5/16	1	50	**20**	Positive
$CP_{clipped}$ 2N	5/8	5/16	1	50	**20**	Negative
$CP_{clipped}$ 3P	5/8	5/16	1	50	**40**	Positive
$CP_{clipped}$ 3N	5/8	5/16	1	50	**40**	Negative
CP_{no_clip} 1P	5/8	5/16	0	50	**0**	Positive
CP_{no_clip} 1N	5/8	5/16	0	50	**0**	Negative
CP_{no_clip} 2P	5/8	5/16	0	50	**20**	Positive
CP_{no_clip} 2N	5/8	5/16	0	50	**20**	Negative
CP_{no_clip} 3P	5/8	5/16	0	50	**40**	Positive
CP_{no_clip} 3N	5/8	5/16	0	50	**40**	Negative
CP_{no_clip} 4P	**1/2**	5/16	0	50	0	Positive
CP_{no_clip} 4N	**1/2**	5/16	0	50	0	Negative
CP_{no_clip} 5P	**3/4**	**3/8**	0	50	0	Positive
CP_{no_clip} 5N	**3/4**	**3/8**	0	50	0	Negative
CP_{no_clip} 6P	5/8	**1/4**	0	50	0	Positive
CP_{no_clip} 6N	5/8	**1/4**	0	50	0	Negative
CP_{no_clip} 7P	5/8	**3/8**	0	50	0	Positive
CP_{no_clip} 7N	5/8	**3/8**	0	50	0	Negative
CP_{no_clip} 8P	5/8	5/16	0	**70**	**0**	Positive
CP_{no_clip} 8N	5/8	5/16	0	**70**	**0**	Negative
CP_{no_clip} 9P	5/8	5/16	0	**70**	**20**	Positive
CP_{no_clip} 9N	5/8	5/16	0	**70**	**20**	Negative
CP_{no_clip} 10P	5/8	5/16	0	**70**	**40**	Positive
CP_{no_clip} 10N	5/8	5/16	0	**70**	**40**	Negative

The model geometry used for investigating the connection plate details included a connection plate modeled at midspan (Figure 9). The attachment detail between the connection plate and adjacent flanges was varied between the three detail classes as previously described, shown in Figure 9(c), (d), and (e). In all cases, the connection plate was modeled as 5/8 inch thick. For models in which a clip is present between the flange and connection plate, the clip was modeled as a right triangle with two 1-inch legs.

The meshing structure for the connection plate detail models closely followed that described previously. Figure 9b shows the mesh pattern and density used in the region of interest.

Most of the connection plate detail models were assigned homogenous material properties for the flanges and web, but some models for the proposed detail practice (CP_{no_clip}) simulated a hybrid girder with 50-ksi web material and 70-ksi flange material.

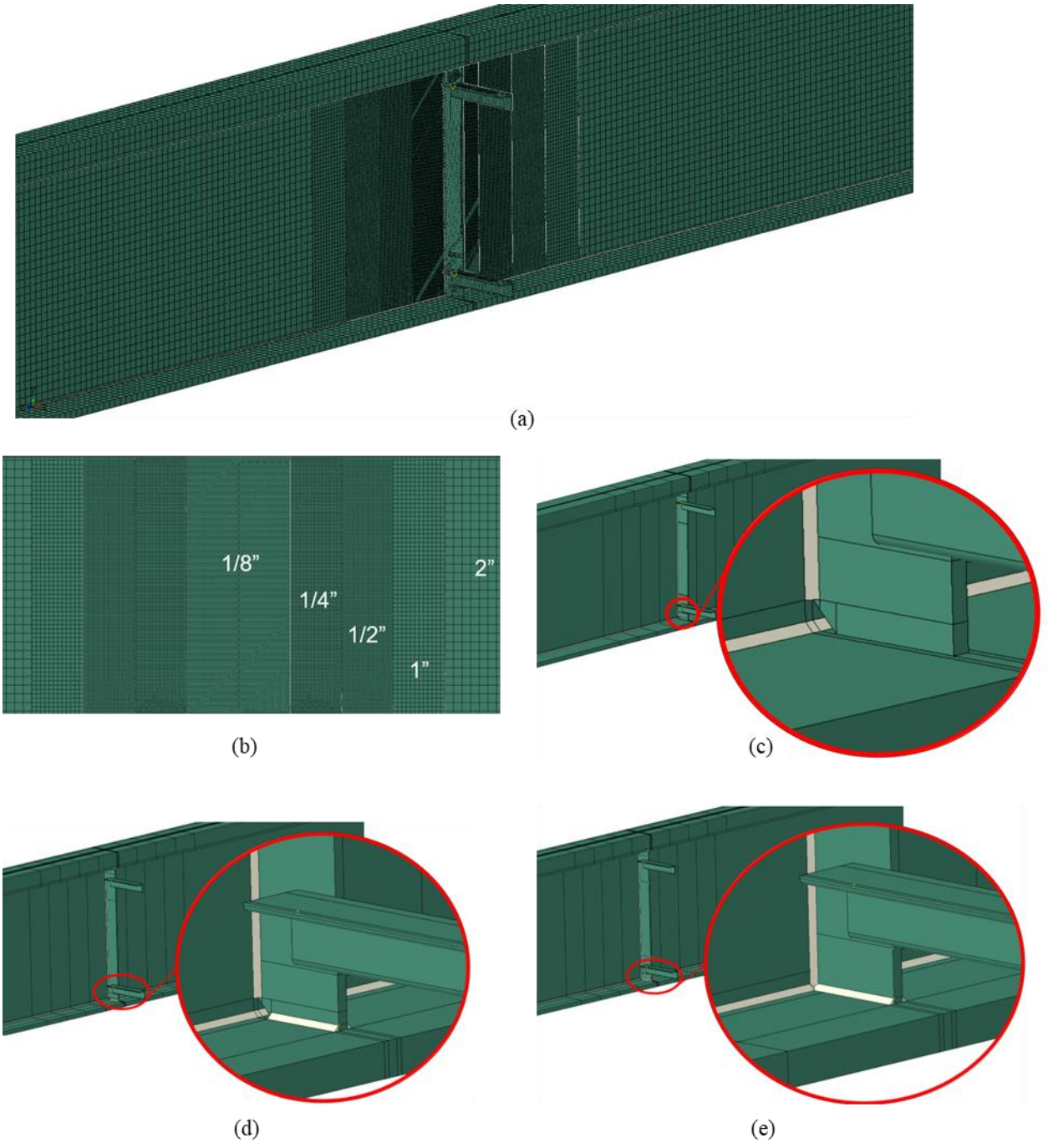

Source: FHWA.

Figure 9. Illustration. Model structure for connection plate details: (a) meshed girder; (b) mesh structure at midspan; (c) CP_{not_welded} detail; (d) $CP_{clipped}$; (e) CP_{no_clip}.

4.1.2 Constitutive Model

Three nonlinear steel material profiles were developed in Abaqus. The first material was assigned yield strength F_y=50 ksi and ultimate strength of F_u=65 ksi, and was used for all components of the plate girder, such as flanges, web, and stiffeners. The second material was assigned F_y=57 ksi and F_u=70 ksi, and was

used to create the fillet welds in the plate girder. The third material was assigned F_y=70 ksi and F_u=85 ksi, and was used for girder flanges in hybrid girder models.

The elastic properties of all materials were assigned Young's modulus of 29,000 ksi and Poisson's ratio of 0.3. To determine the plastic properties for the two materials, the Ramberg-Osgood relationship (Eq 4-1 to Eq 4-5) was used to generate engineering stress strain curves, where σ is the stress, E is the elastic modulus of the material, S_{ty} is the tensile yield strength of the material, S_{tu} is the material ultimate strength, and n is the strain hardening exponent of the material in Eq 4-2. O_s is assumed to be 0.002 which is consistent with the 0.2% offset method, and e_L is the assumed elongation percentage for the material, which was 21% for the F_y=50 ksi material, 22% for the F_y=57 ksi material (welds), and 16% for the F_y=70 ksi material. The Ramberg-Osgood determines a constitutive relationship in terms of true stress-strain.

$$\varepsilon = \frac{\sigma}{E} + 0.002\left(\frac{\sigma}{S_{ty}}\right)^{\frac{1}{n}} \quad \textbf{Eq 4-1}$$

$$n = log\left(\frac{S_{tu}}{S_{ty}}\right)/log\left(\frac{\varepsilon_f}{\varepsilon_p}\right) \quad \textbf{Eq 4-2}$$

$$\varepsilon_{yield} = \frac{\delta_y}{E} + O_s \quad \textbf{Eq 4-3}$$

$$\varepsilon_{ult} = \frac{S_{tu}}{E} + \varepsilon_f \quad \textbf{Eq 4-4}$$

$$e_f = \frac{e_L}{100\%} \quad \textbf{Eq 4-5}$$

Figure 10, Figure 11, and Figure 12 show the stress-strain curves for each material. The plastic stress-strain curves which start at the yield stress and end at the ultimate stress are separated from the total true stress-strain curve of the materials and were inputted in Abaqus as piecewise-linear to determine the materials' plasticity.

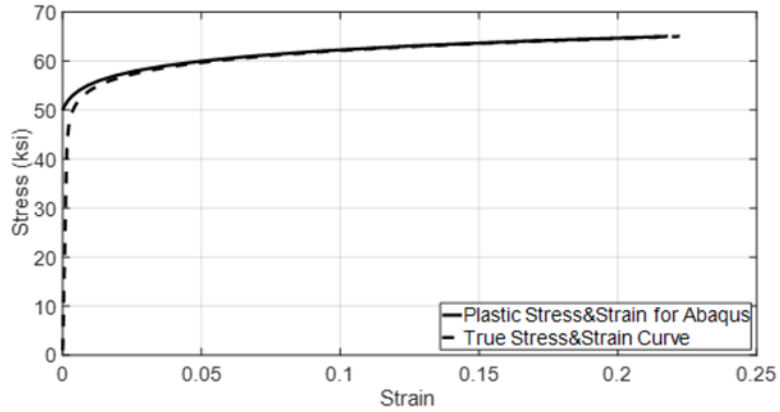

Yield Stress	Plastic Strain
50	0
53	0.0036
55	0.0088
57	0.0184
60	0.0488
63	0.1186
65	0.208

Source: FHWA.

Figure 10. Graph. True stress-strain curve and true plastic stress-strain curve for material with F_y=50 ksi and F_u=65 ksi.

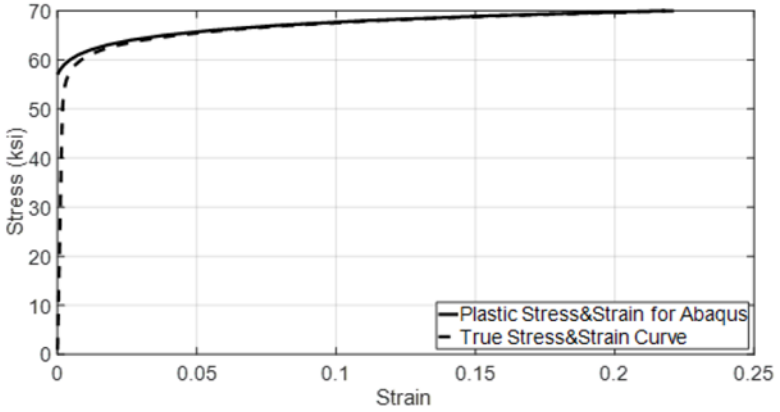

Yield Stress	Plastic Strain
50	0
59	0.0024
61	0.0074
63	0.0177
65	0.0384
67	0.0788
70	0.218

Source: FHWA.

Figure 11. Graph. True stress-strain curve and true plastic stress-strain curve for material with F_y=57 ksi and F_u=70 ksi.

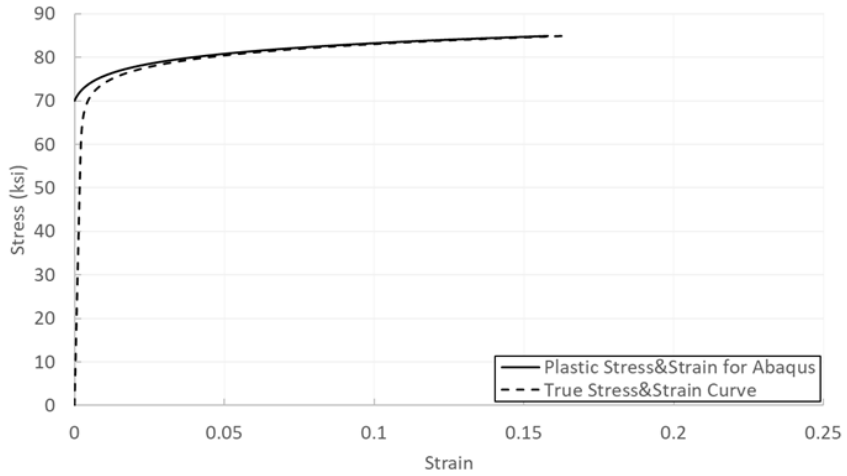

Yield Stress	Plastic Strain
70	0
72	0.0018
74	0.0050
76	0.0108
78	0.0210
80	0.0387
82	0.0691
84	0.1205
85	0.1580

Source: FHWA.

Figure 12. Graph. True stress-strain curve and true plastic stress-strain curve for material with F_y=70 ksi and F_u=85 ksi.

4.1.3 Mesh Sensitivity

Figure 13 shows the plot of T_2 as a function of the mesh size for the plate girder base model for both linear and quadratic element types. T_2 for the base model does not have a steep slope in the range of 0.1 inches to 0.25 inches as a function of the mesh size. Therefore, the central part of the girder was meshed within the same range.

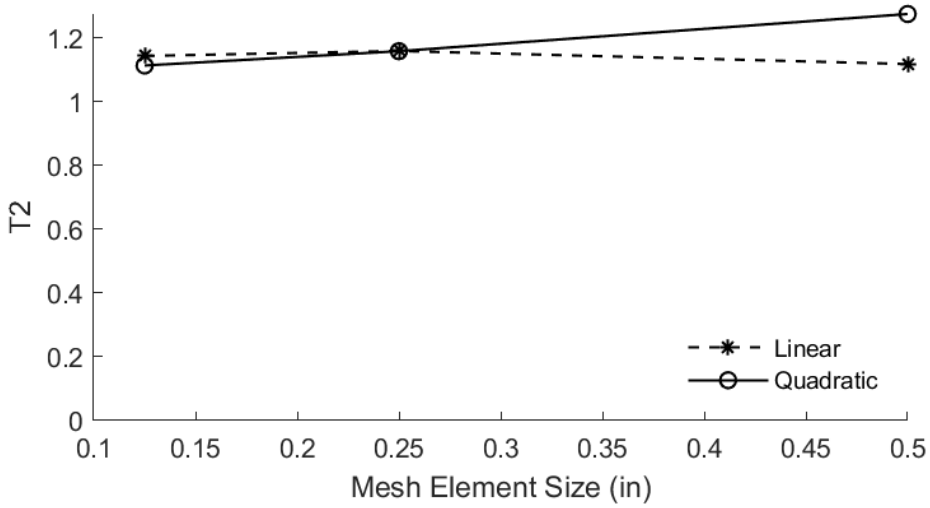

Source: FHWA.

Figure 13. Graph. T_2 as a function of mesh size.

4.2 RESULTS AND DISCUSSION

For each model, data was extracted along 22 paths on the girder web that extended the height of the web. The locations of the data extraction paths are shown in Figure 14. For each path, the stress values (σ_1, σ_2,

σ_3, and σ_{eff}) were extracted at each node along the path, and $\sigma_{hydrostatic}$, T_1, and T_2 were computed for each node. The peak values for T_1 and T_2 were identified for each path, and in each case, those peak values were confirmed as occurring at the detail of interest rather than at a superfluous location (e.g., flange and web junction). In this way, peak triaxiality was computed and considered in a holistic way at each detail considered.

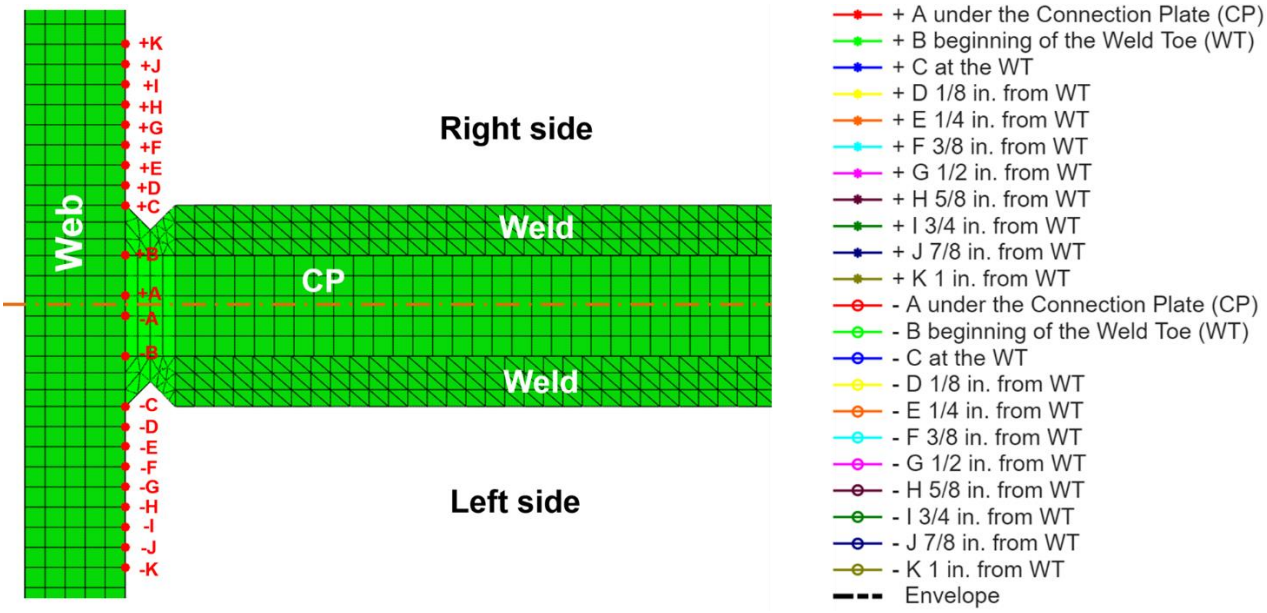

Source: FHWA.

Figure 14. Illustration. Section cut showing locations of data extraction paths.

4.2.1 Orthogonal Stiffener Details

4.2.1.1 Discontinuous Transverse Stiffener Details

The influence of constraint relief gap dimension, web thickness, weld size, and stiffener thickness were considered (Figure 15, Figure 16, and Figure 17). Here, the data from the individual paths are not shown and just the envelopes are presented for clarity.

Each of the plots for T_1 and T_2 show consistent lack of sensitivity to the three variables. T_1 was nearly constant at a value of 0.5 for all variables and variable values; similarly, T_2 remained nearly constant with a magnitude of 1.2. Therefore, two observations emerge:

(1) triaxiality is not sensitive to changes in local geometry for the DTS detail, based on the results of all 24 models with the DTS detail; and

(2) the magnitudes for T_1 and T_2 are much lower for the DTS detail than for the DLS detail (results discussed in the following section).

The second observation should not be surprising since the DTS detail has been understood for decades to be a preferable detail over the DLS detail from a fatigue perspective, and it has not shown susceptibility to CIF in field applications. However, this research is the first occasion to demonstrate that the DTS detail is

likely not a CIF concern, and is insensitive to detailing CRG dimensions, which is a positive finding for the state of practice.

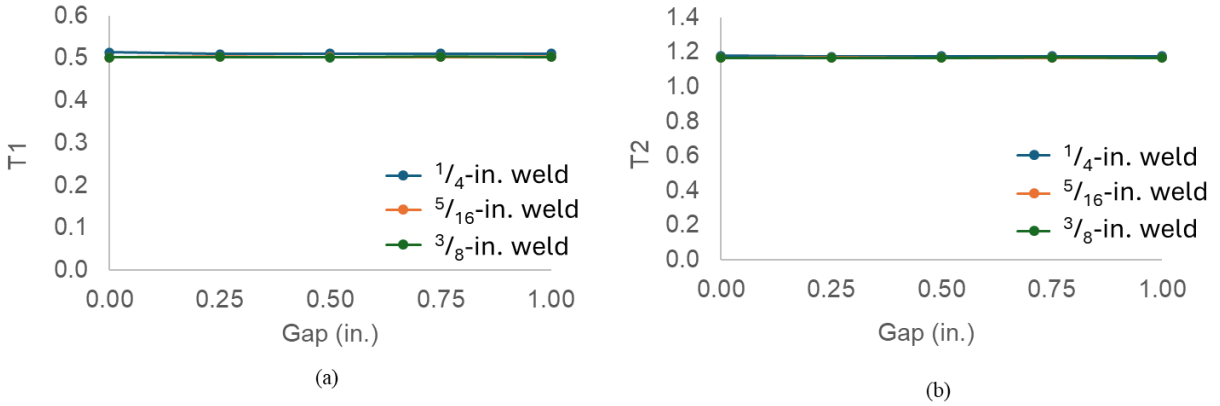

Source: FHWA.

Figure 15. Graph. Envelope of maximum values for the DTS detail, for varied constraint relief gap dimensions and weld sizes (web = 5/8 inch thick; stiffeners = 5/8 inch thick): (a) T_1; (b) T_2.

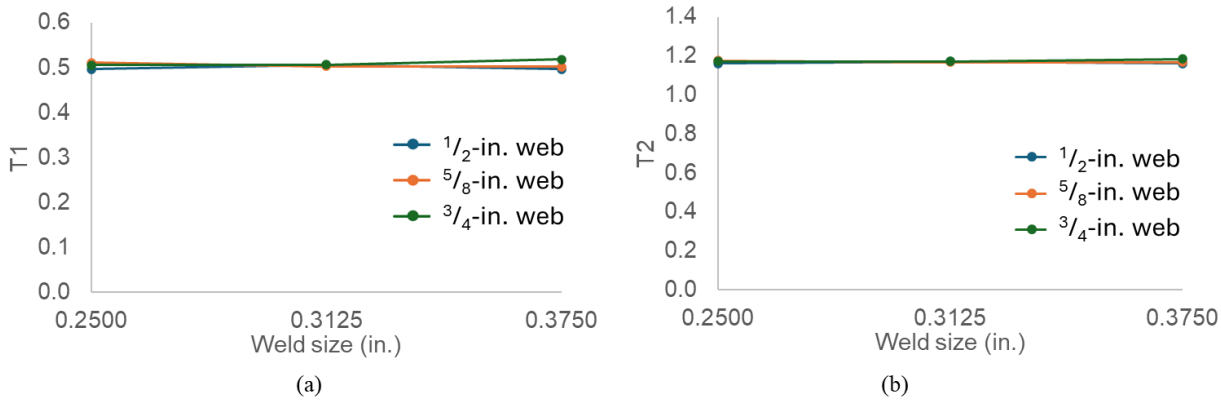

Source: FHWA.

Figure 16. Graph. Envelope of maximum values for the DTS detail, for varied web thicknesses and weld sizes (CRG = 1/2 inch; stiffeners = 5/8 inch thick): (a) T_1; (b) T_2.

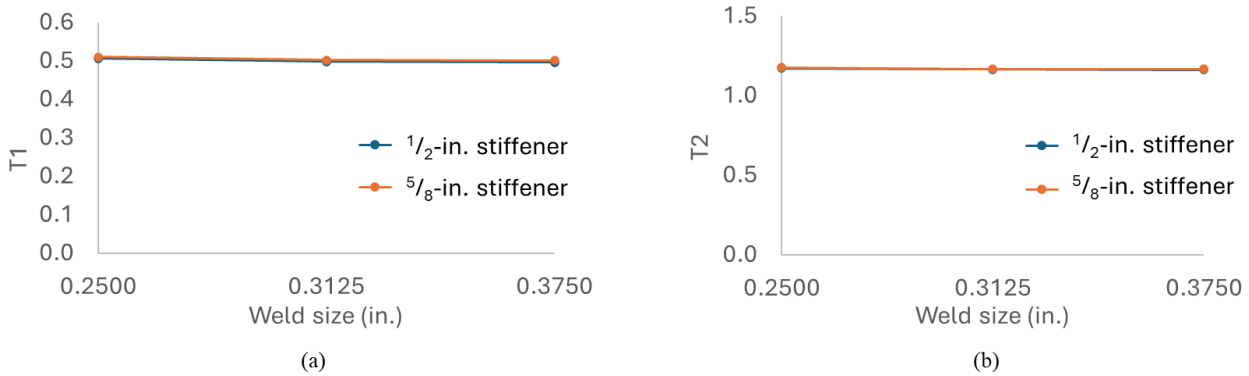

Source = FHWA.

Figure 17. Graph. Envelope of maximum values for the DTS detail, for varied stiffener thickness and weld size (CRG = 1/2 inch; web = 5/8 inch thick): (a) T_1; (b) T_2.

4.2.1.2 Discontinuous Longitudinal Stiffener Details

Representative contour plots showing the distribution of T_2 in a DLS model are shown in Figure 18 and Figure 19. Figure 18 shows the triaxiality distribution in the girder including at the location of longitudinal stiffener truncation at the transverse stiffener. Figure 19 shows the triaxiality distribution in the girder web with the stiffeners hidden from view. In this case, peak triaxiality occurs in the constraint relief gap at the toe of the weld on the longitudinal stiffener with a peak value of T_2=1.92.

Figure 20 presents aggregated data for T_1 and T_2 that describe triaxiality demand in the region of interest for varied constraint relief gap dimensions (0 inches, 1/4 inch, 1/2 inch, 3/4 inch, and 1 inch). The plots present maximum triaxiality values extracted from each path.

Results for both T_1 and T_2 reveal a consistent trend. The state of triaxiality is greatest for the case with no constraint relief gap provided (CRG=0 inches), with T_1 = 1.5 and T_2 = 2.1. Triaxiality quickly decays for both measures when a small constraint relief gap is introduced (1/4 inch), to T_1 = 1.0 and T_2 = 1.5, and these values are maintained with increasing gap dimensions.

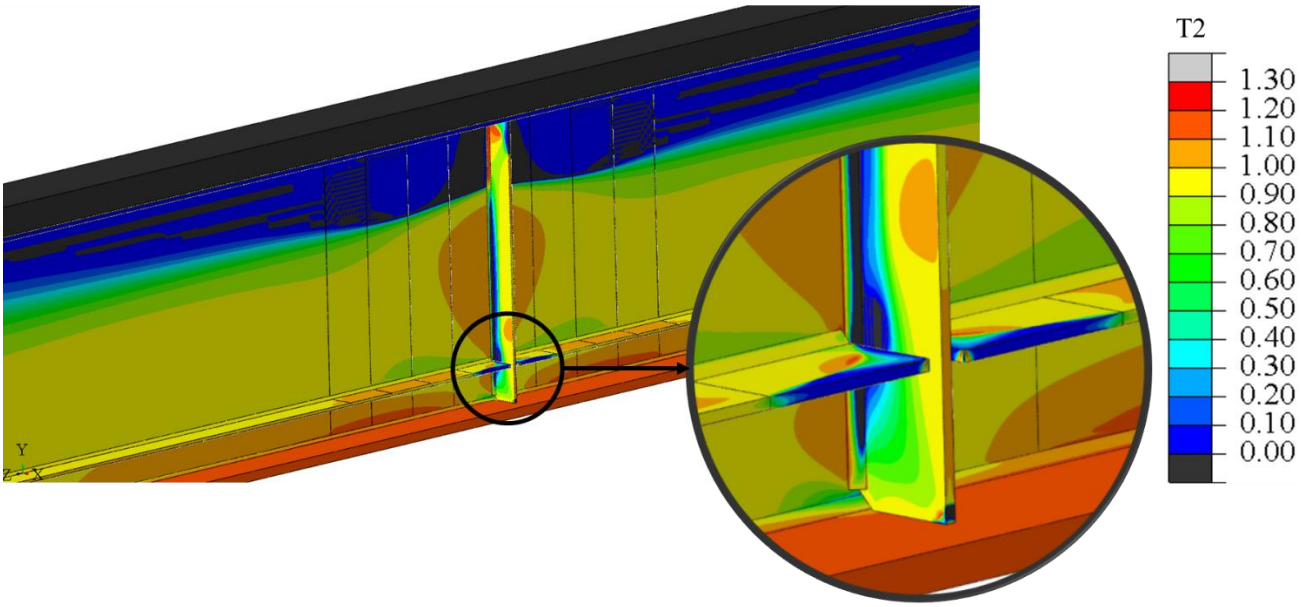

Source: FHWA.

Figure 18. Illustration. T_2 results distribution in a DLS model.

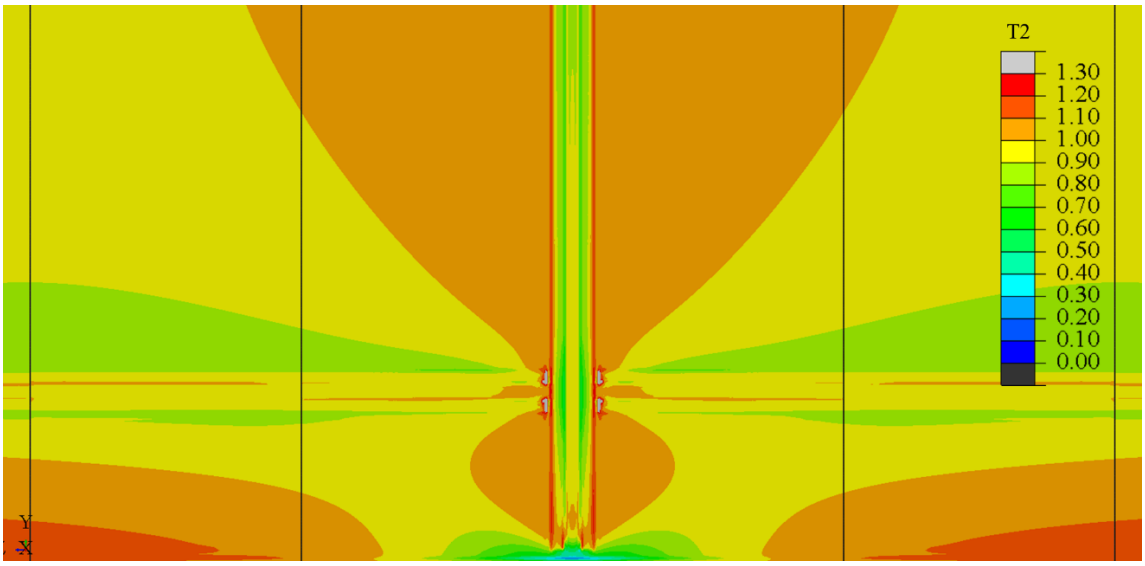

Source: FHWA.

Figure 19. Illustration. T_2 results distribution in a DLS model, web only (stiffeners hidden from view).

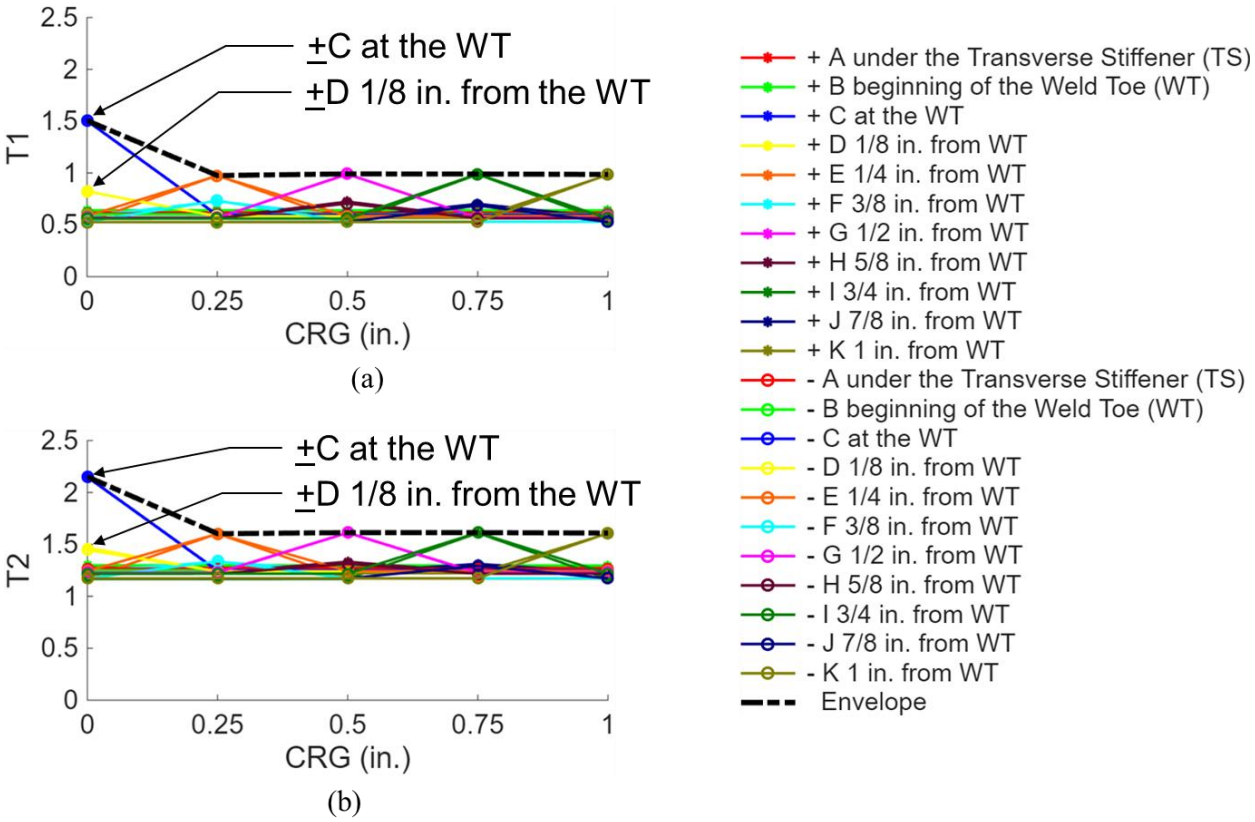

Source: FHWA.

Figure 20. Graph. Envelope of maximum values for the DLS detail, for varied constraint relief gap dimensions: (a) T_1; (b) T_2.

4.2.2 Connection Plate Details

The following sections present results from the models representing historic practice (CP_{not_welded}), current practice ($CP_{clipped}$), and proposed practice (CP_{no_clip}).

Six models each were considered to characterize historic practice and current practice in terms of triaxiality, in which the magnitude of out-of-plane force and direction of primary bending were varied. For the proposed-practice detail (20 models), the magnitude of out-of-plane force, direction of primary bending, web thickness, and weld size were varied.

4.2.2.1 Historic-Practice Connection Plate Detail: CP_{not_welded}

Figure 21 presents a comparison of contour plots for von Mises stress, T_1, and T_2, for the CP_{not_welded} detail under the action of different out-of-plane load magnitudes (0, 20, and 40 kips) and positive bending. A comparison of the results in the absence of out-of-plane loading with results that include out-of-plane loading shows a large effect on the von Mises stresses and T_1 and T_2 induced by the out-of-plane loading. Each of these measures is increased with the inclusion of out-of-plane loading, in a distributed manner.

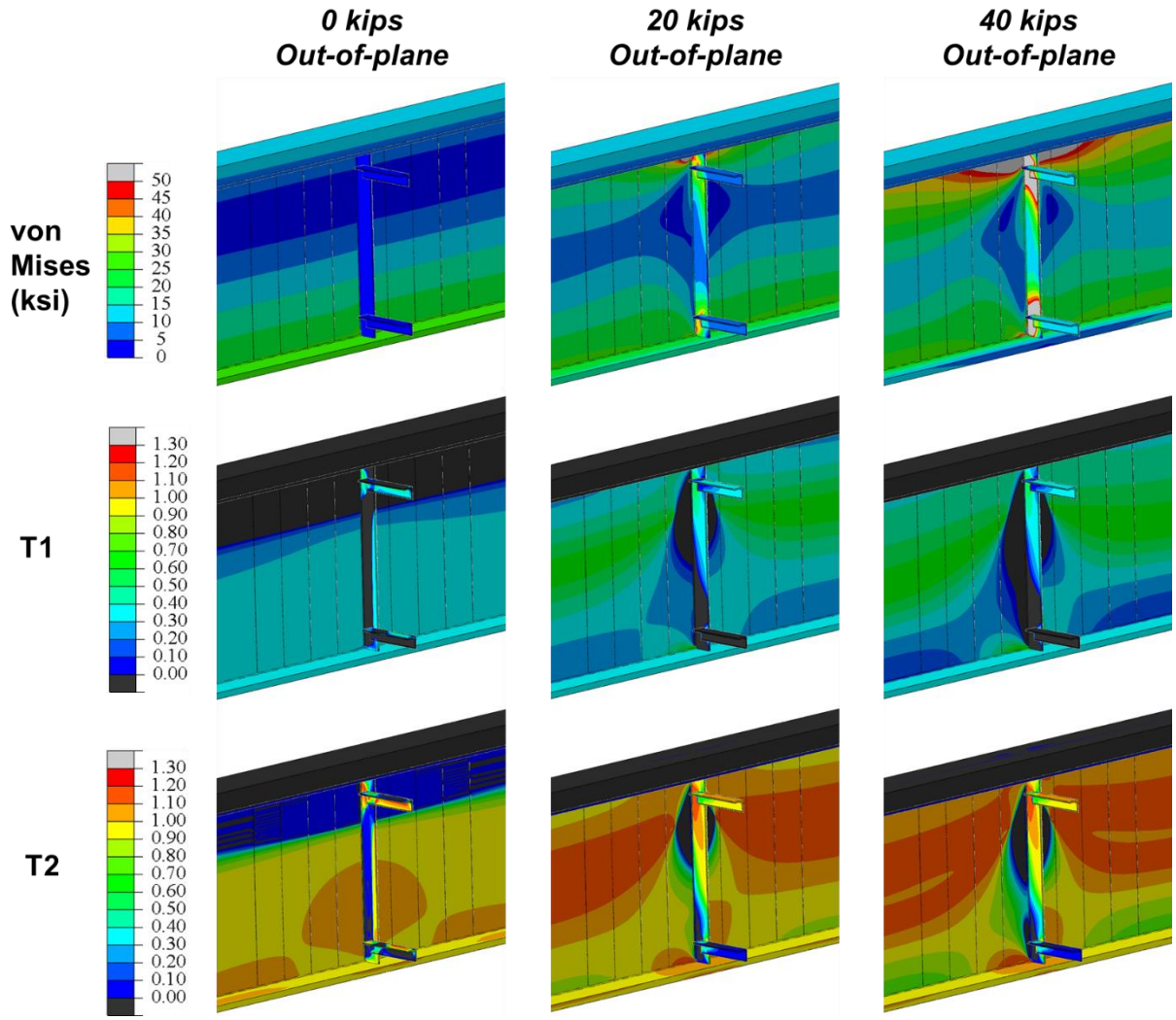

Source: FHWA.

Figure 21. Illustration. Distributions of von Mises stress, T_1, and T_2 for varied out-of-plane load levels when the girder is under positive flexure: historic-practice connection plate detail.

The influence of out-of-plane loading on T_1 and T_2 is quantified in Figure 22 for positive flexure and Figure 23 for negative flexure. Figure 24 distills the data into a direct comparison of T_1 and T_2 envelopes for positive and negative bending. Several observations are apparent:

1. For the case with no out-of-plane loading, the magnitude of triaxiality is similar to that present in the DTS detail: $T_1 = 0.5$ and $T_2 = 1.1$, for both positive and negative bending cases. The models with no out-of-plane loading are capturing behavior of a transverse stiffener rather than a connection plate, the former of which is a detail that has had a good practical performance record.

2. There is a large increase in triaxiality with the introduction of out-of-plane loading, for both positive and negative bending cases. In the presence of 20 kips of out-of-plane loading, $T_1 = 1.5$ and 1.2 for

positive and negative bending, respectively, and $T_2 = 2.0$ and 1.9 for positive and negative bending, respectively. These magnitudes are similar to those computed for the DLS with no constraint relief gap ($T_1 = 1.5$ and $T_2 = 2.1$). This suggests elevated susceptibility to constraint-induced fracture in the presence of significant out-of-plane loads, on the basis of a poor practical performance record of details like the discontinuous longitudinal stiffener. Tempering this observation, it should be noted that bridges containing this detail near the tension flange have historically been susceptible to distortion-induced fatigue cracking, but few cases of cracking at similar details have been attributed to CIF. The Norman Wood Bridge is one example of a similar detail that was attributed to CIF, where a constraint-induced fracture occurred over a pier where a floorbeam connected into the girder through a connection plate that was unattached to the girder tension (top) flange.

3. The results are sensitive to the direction of primary flexure in the presence of out-of-plane loads, and particularly for very large-magnitude out-of-plane loads. The 40-kip out-of-plane load case produces $T_1 = 1.2$ and $T_2 = 1.7$ for positive bending, and $T_1 = 1.6$ and $T_2 = 2.1$ for negative bending. For very large-magnitude out-of-plane loads (40 kips), negative bending was found to produce greater triaxiality than positive bending. Note that this was the load case that induced tension in the upper CP detail combined with tensile out-of-plane loading. Differences were much less pronounced for the 20-kip out-of-plane load case, but triaxiality was greatest under positive bending.

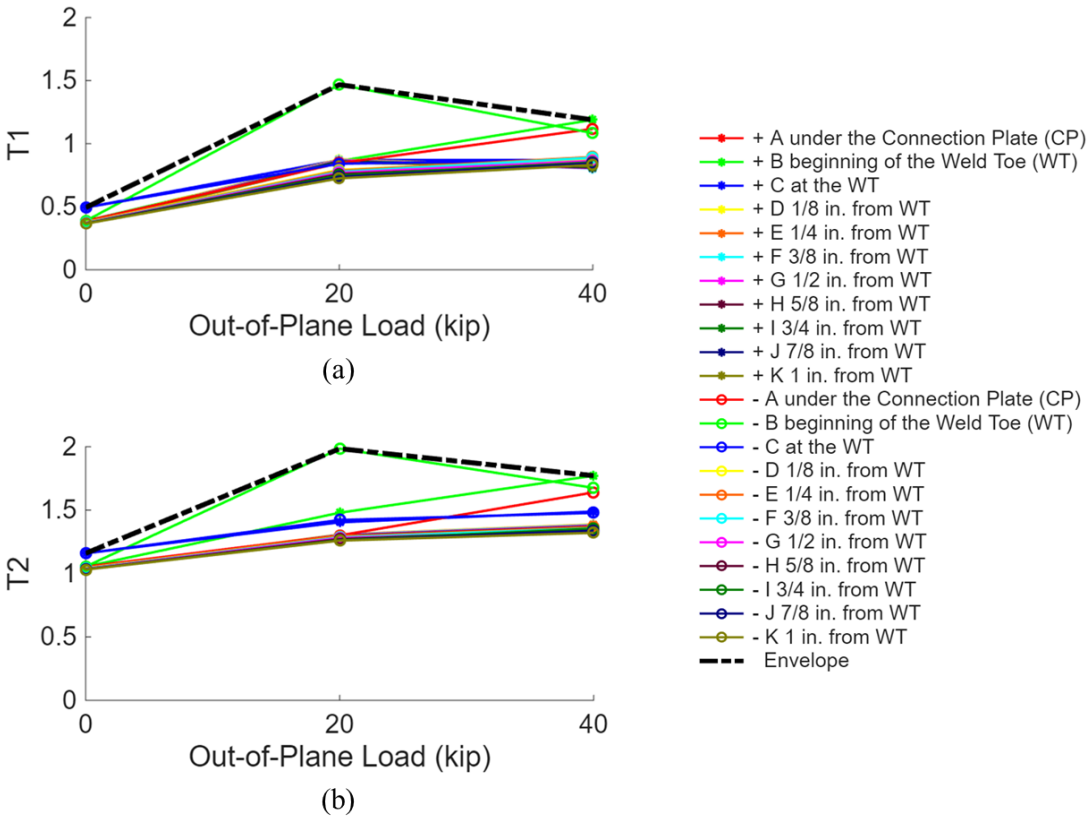

Source: FHWA.

Figure 22. Graph. Envelope of maximum values for the connection plate detail CP_{not_welded}, for varied out-of-plane load levels when the girder is under positive flexure: (a) T_1; (b) T_2.

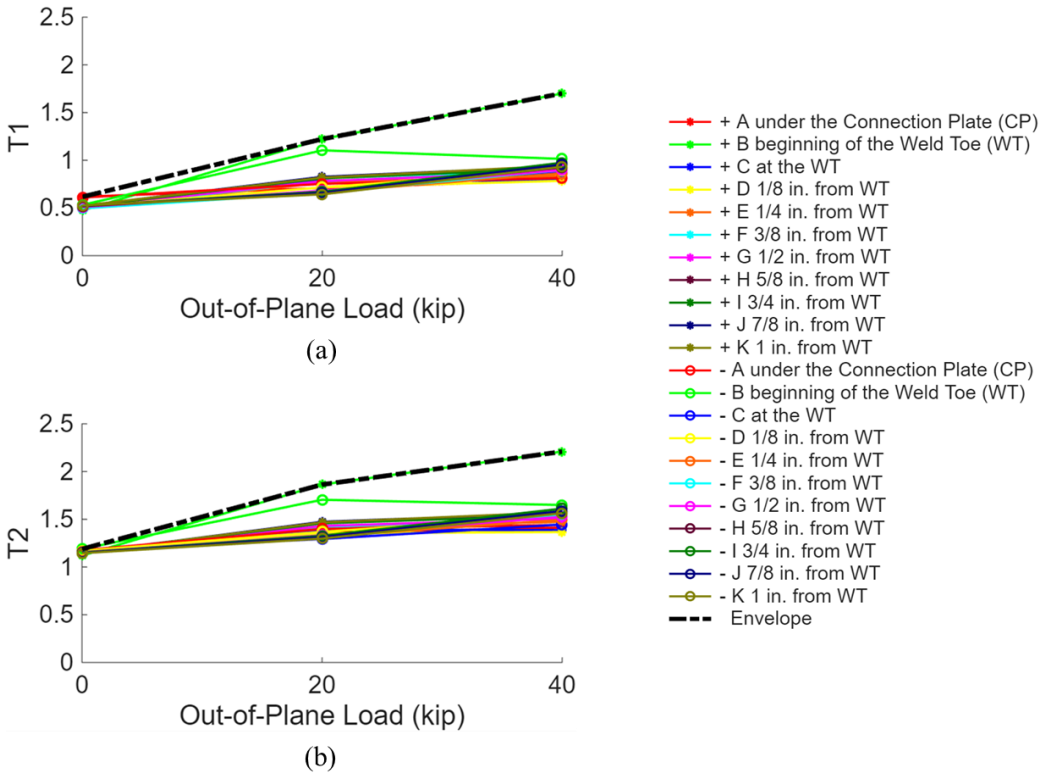

Source: FHWA.

Figure 23. Graph. Envelope of maximum values for the connection plate detail CP_{not_welded}, for varied out-of-plane load levels when the girder is under negative flexure: (a) T_1; (b) T_2.

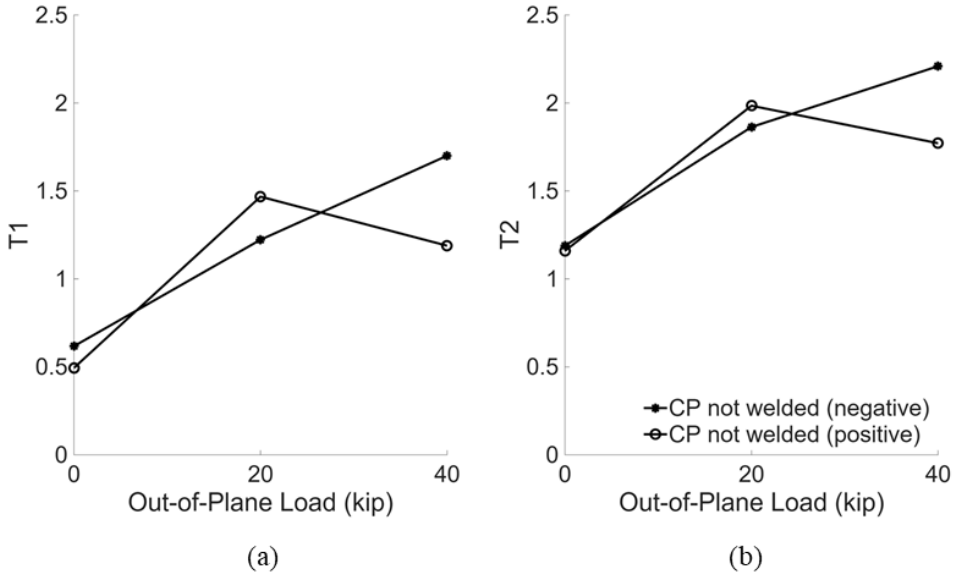

Source: FHWA.

Figure 24. Graph. Envelopes of maximum values for historic-practice connection plate detailing: (a) T_1; (b) T_2.

4.2.2.2 Current-Practice Connection Plate Detail: $CP_{clipped}$

Figure 25 shows a comparison of von Mises stress, T_1, and T_2, contour plots for the current-practice connection plate detail under the action of different-magnitude out-of-plane loads.

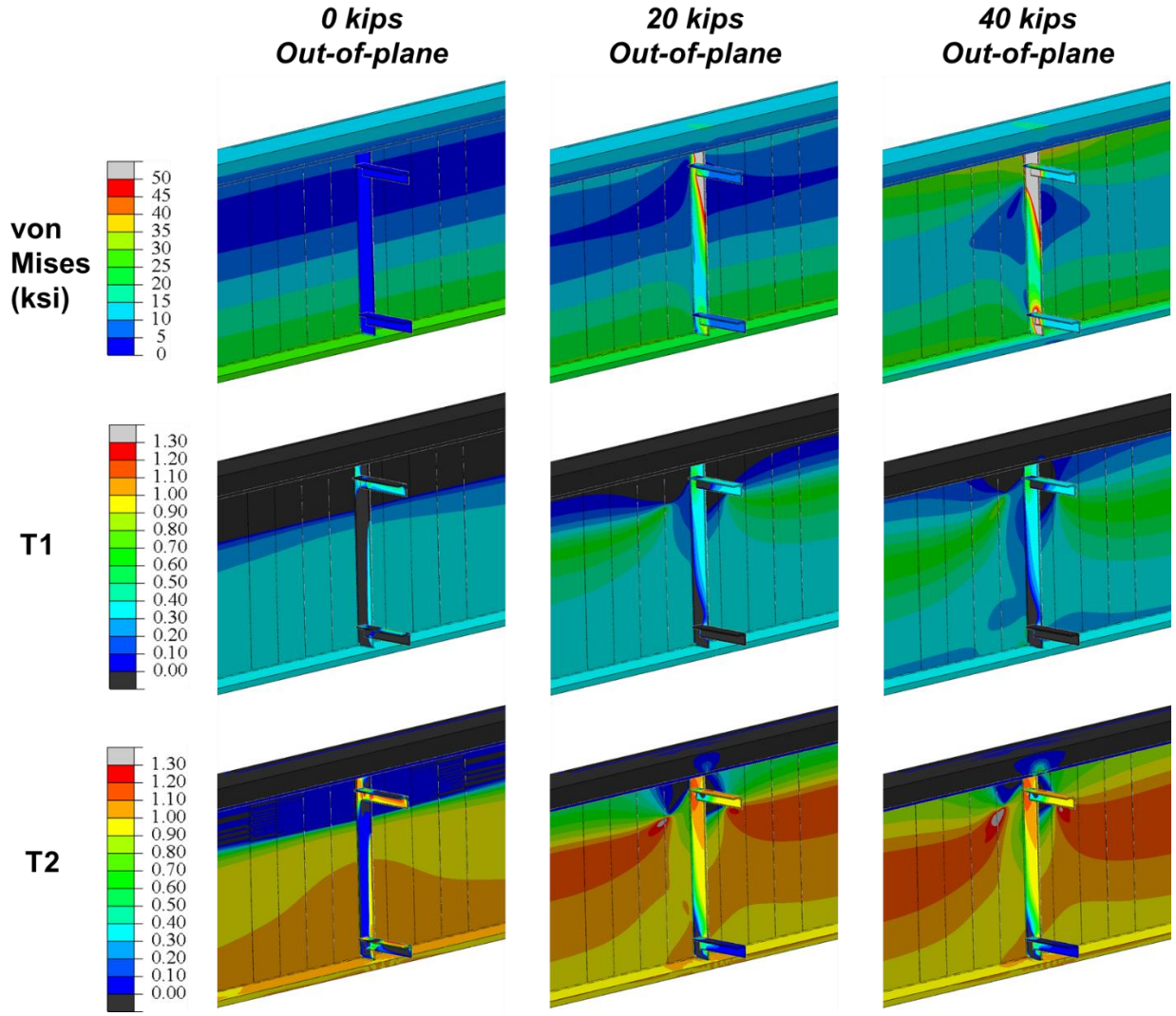

Source: FHWA.

Figure 25. Illustration. Distributions of von Mises stress, T_1, and T_2, for varied out-of-plane load levels when the girder is under positive flexure: current-practice connection plate detail.

Figure 26 and Figure 27 present T_1 and T_2 for current-practice connection plate detailing. Figure 28 distills the data into a direct comparison of T_1 and T_2 envelopes for positive and negative bending. The following observations emerge:

1. For the case with no out-of-plane loading, the magnitude of triaxiality is similar to that present in the DTS detail and historic-practice connection plate detailing: $T_1 = 0.5$ and $T_2 = 1.1$, for both positive and negative bending cases. The models with no out-of-plane loading are capturing

behavior of a transverse stiffener rather than a connection plate, the former of which is a detail that has had a good practical performance record. This indicates that susceptibility of the current-practice connection plate detail to constraint-induced fracture in the absence of out-of-plane loads is small.

2. As was the case for the historic-practice connection plate detail, triaxiality increases with the introduction of out-of-plane loading, for both positive and negative bending cases. The increase is small for the 20-kip out-of-plane load level in positive bending (T_1=0.51 for 0-kips out-of-plane force and 0.74 for 20-kips out-of-plane force), but quite large for negative bending (T_1=0.59 for 0-kips out-of-plane force and 1.14 for 20-kips out-of-plane force). As out-of-plane force increases beyond 20 kips to 40 kips, the magnitudes of T_1 and T_2 continue to increase for positive bending and remain constant for negative bending.

3. For cases with large-magnitude out-of-plane loads, triaxiality magnitudes are lower than those for historic-practice connection plate detailing and for the discontinuous longitudinal stiffener with no constraint relief gap. Nonetheless, triaxiality is still elevated compared to the magnitudes determined for discontinuous transverse stiffeners.

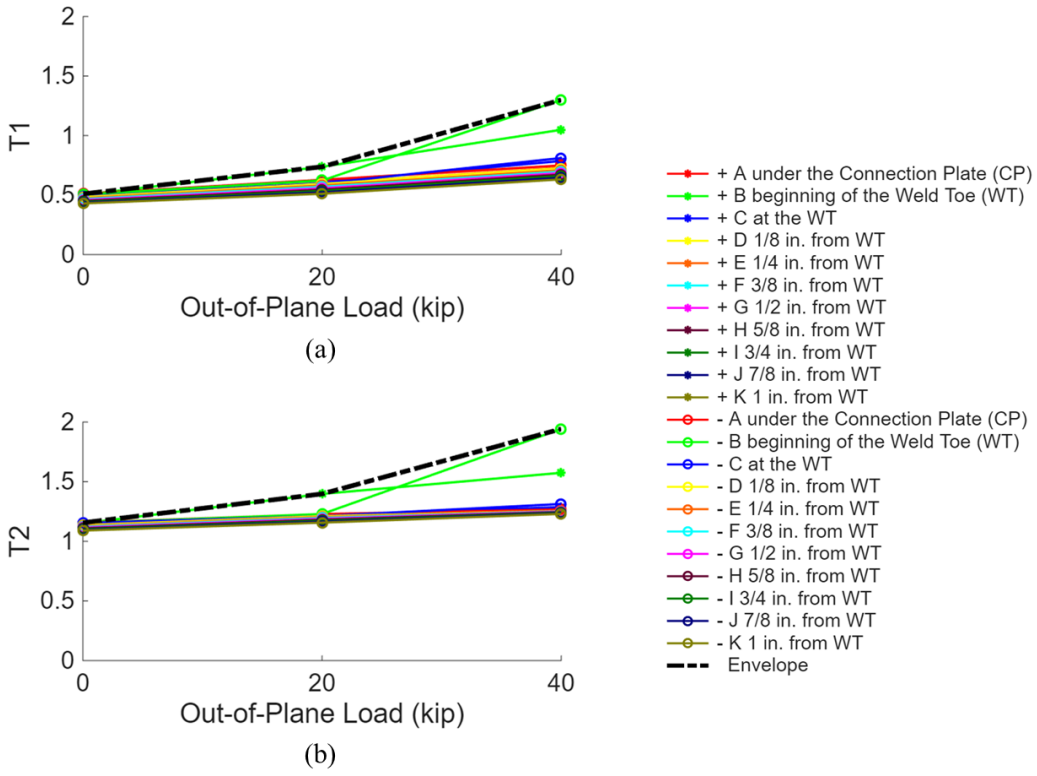

Source: FHWA.

Figure 26. Graph. Envelope of maximum values for the connection plate detail $CP_{clipped}$, for varied out-of-plane load levels when the girder is under positive flexure: (a) T_1; (b) T_2.

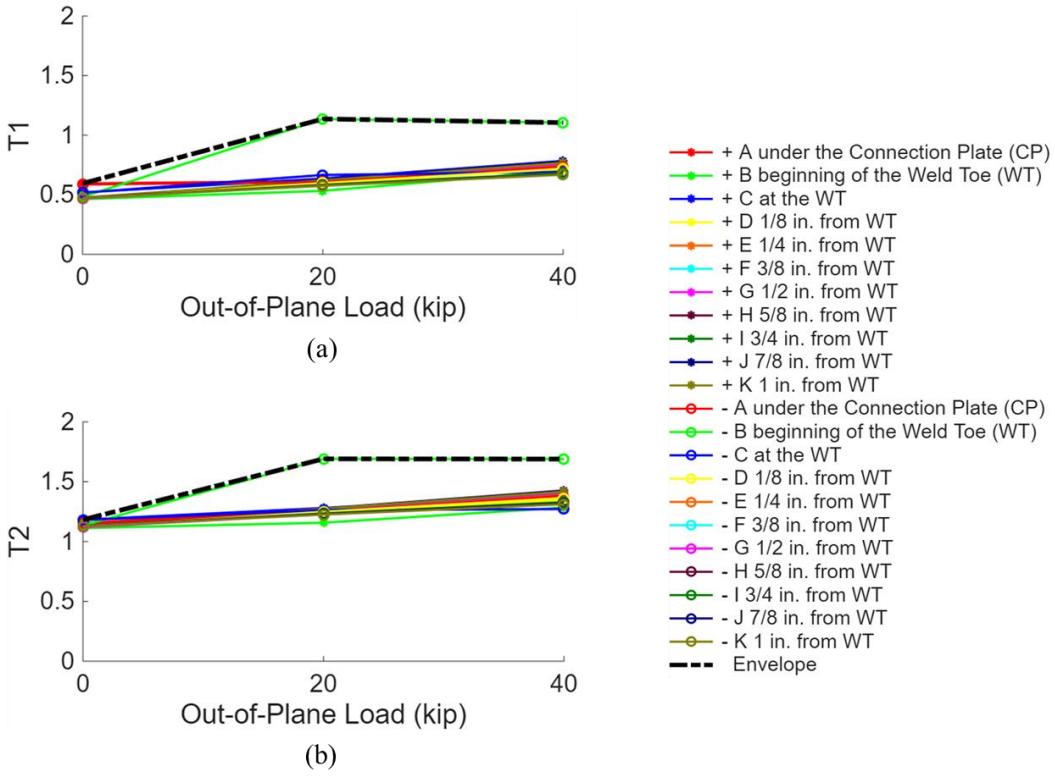

Source: FHWA.

Figure 27. Graph. Envelope of maximum values for the connection plate detail $CP_{clipped}$, for varied out-of-plane load levels when the girder is under negative flexure: (a) T_1; (b) T_2.

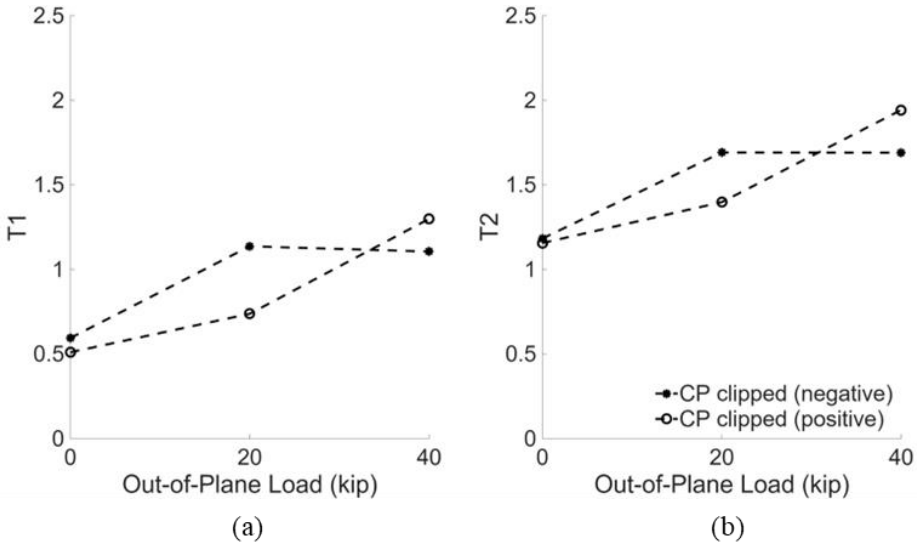

Source: FHWA.

Figure 28. Graph. Envelopes of maximum values for current-practice connection plate detailing: (a) T_1; (b) T_2.

4.2.2.3 Proposed-Practice Connection Plate Detail: CP_{no_clip}

Figure 29 shows a comparison of von Mises stress, T_1, and T_2, contour plots for the proposed-practice connection plate detail under the action of different-magnitude out-of-plane loads.

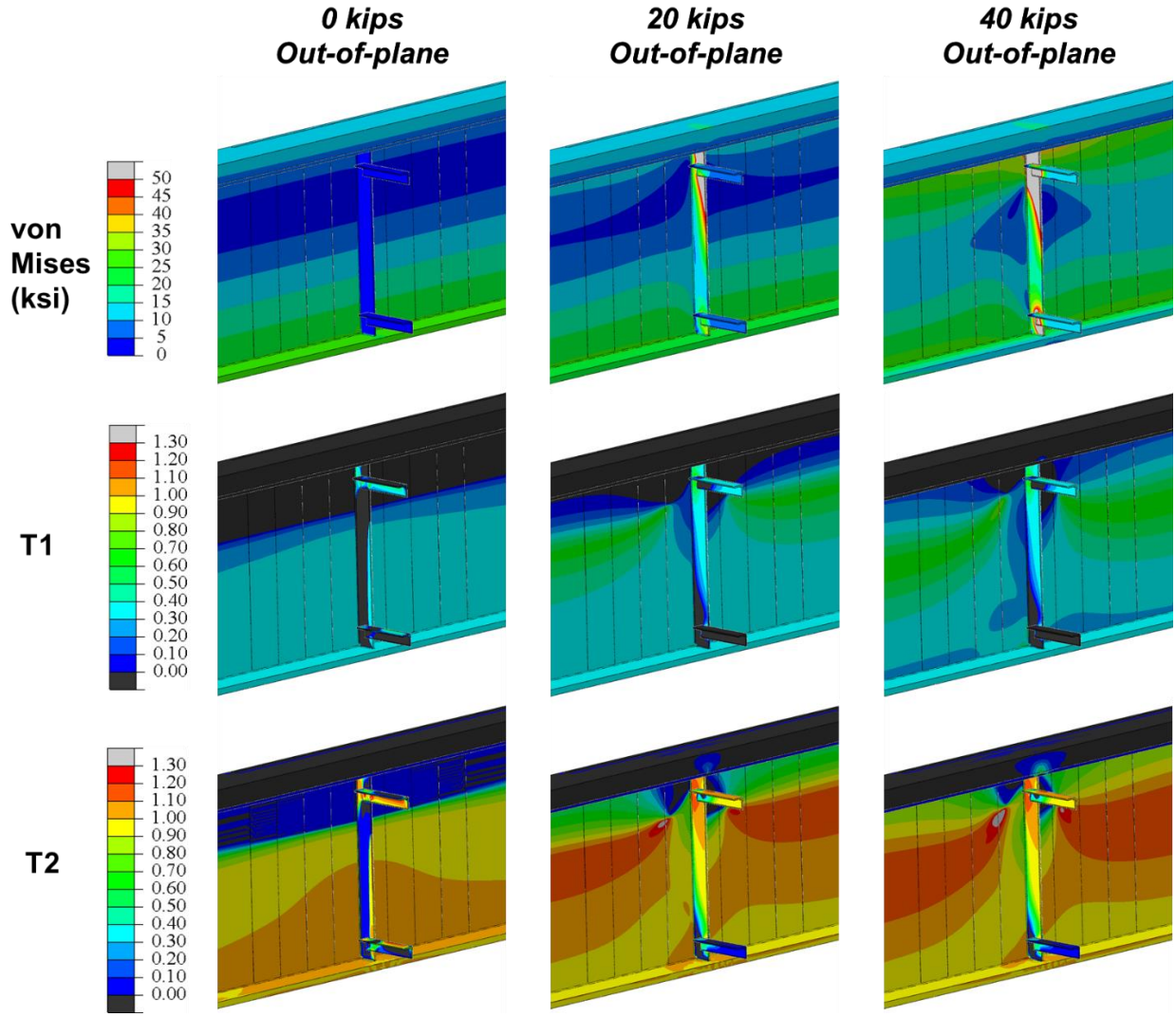

Source: FHWA.

Figure 29. Illustration. Distributions of von Mises stress, T_1, and T_2 for varied out-of-plane load levels when the girder is under positive flexure: proposed-practice connection plate detail.

Figure 30, Figure 31, and Figure 32 present the influence of out-of-plane load on triaxiality in the proposed-practice connection plate detail. The magnitudes and trends are similar to those observed for the current-practice connection plate detail.

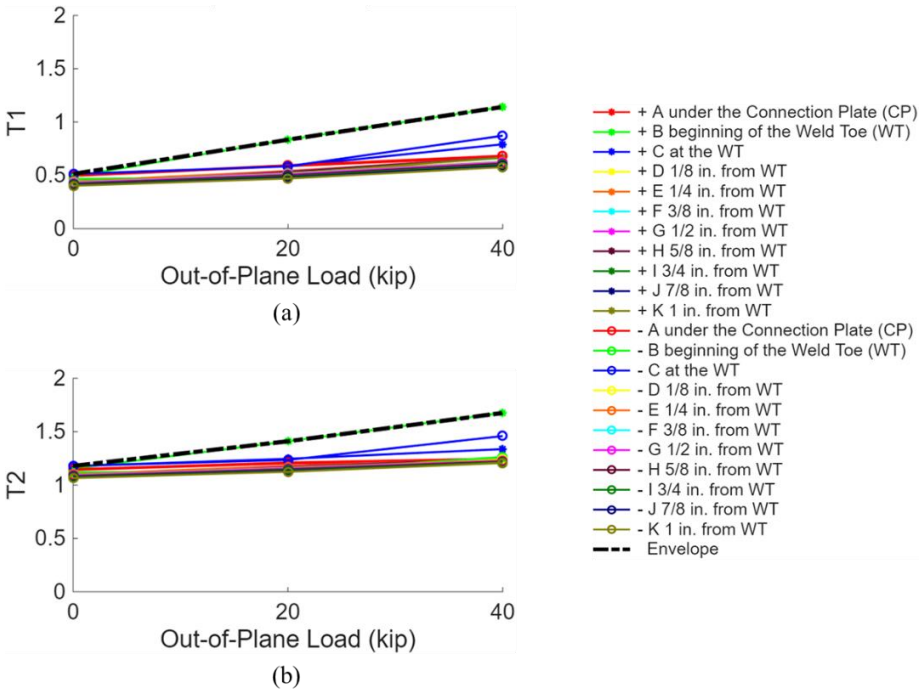

Source: FHWA.

Figure 30. Graph. Envelope of maximum values for the connection plate detail CP_{no_clip}, for varied out-of-plane load levels when the girder is under positive flexure: (a) T_1; (b) T_2.

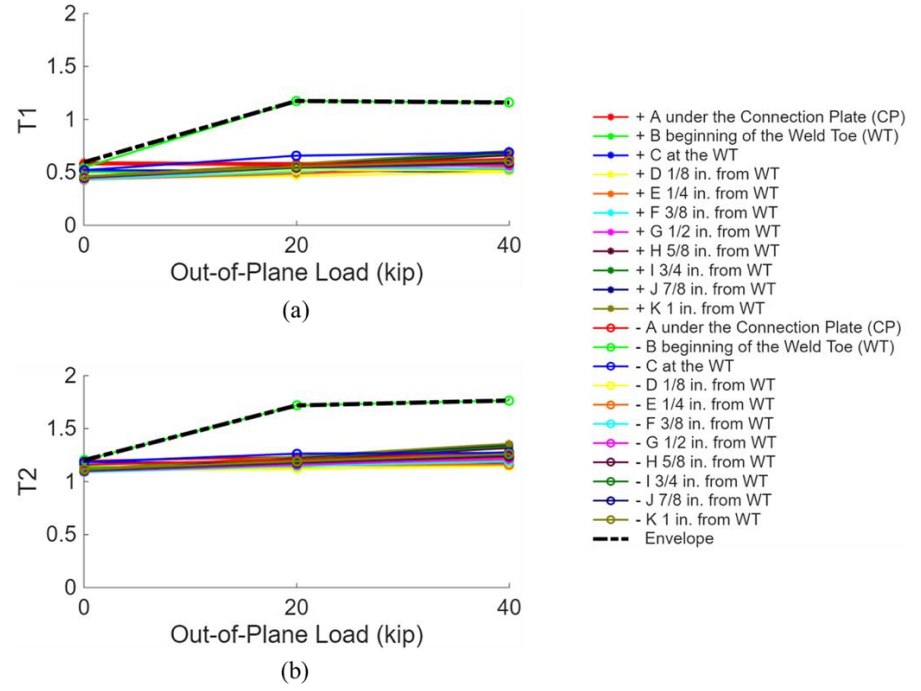

Source: FHWA.

Figure 31. Graph. Envelope of maximum values for the connection plate detail CP_{no_clip}, for varied out-of-plane load levels when the girder is under negative flexure: (a) T_1; (b) T_2.

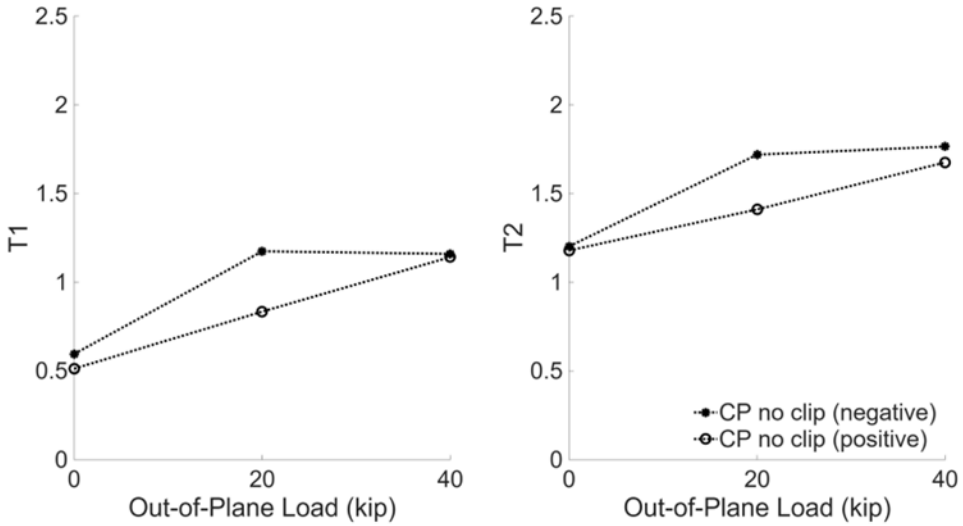

Source: FHWA.

Figure 32. Graph. Envelopes of maximum values for proposed-practice connection plate detailing: (a) T_1; (b) T_2.

Figure 33, Figure 34, and Figure 35 address the influence of using dissimilar materials in a built-up girder on triaxiality. Figure 33 and Figure 34 present triaxiality in the proposed-practice connection plate detail for the hybrid girder case (F_y=50 ksi in the web; F_y=70 ksi in the flanges). Figure 35 presents a comparison of the hybrid and non-hybrid girder results.

Triaxiality was found to be much greater in the hybrid girder detail than in the non-hybrid girder detail for the case with no out-of-plane load: T_1 = 1.2 for the hybrid girder versus 0.5-0.6 for the non-hybrid girder; T_2 = 1.7 for the hybrid girder versus 1.2 for the non-hybrid girder. Interestingly, for the 20-kip and 40-kip out-of-plane load cases, triaxiality demand was lower for the hybrid girder than for the non-hybrid girder. A well-justified explanation for this trend has not been identified, but the data clearly indicate the potential for increased susceptibility to constraint-induced fracture in the presence of a material mismatch when there is no out-of-plane loading.

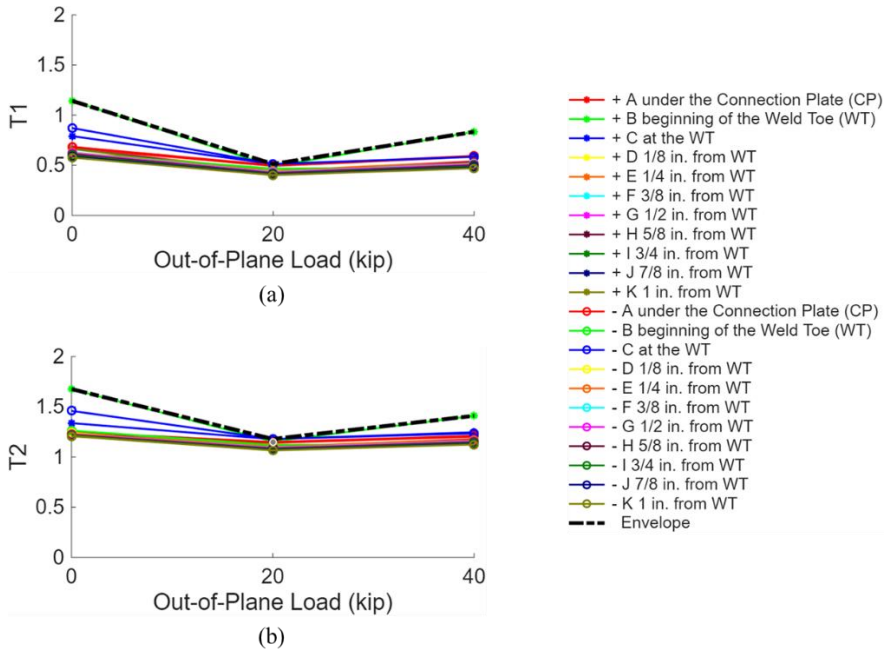

Source: FHWA.

Figure 33. Graph. Envelope of maximum values for the connection plate detail CP_{no_clip}, for varied out-of-plane force when the girder is under positive flexure – Hybrid girder case: (a) T_1; (b) T_2.

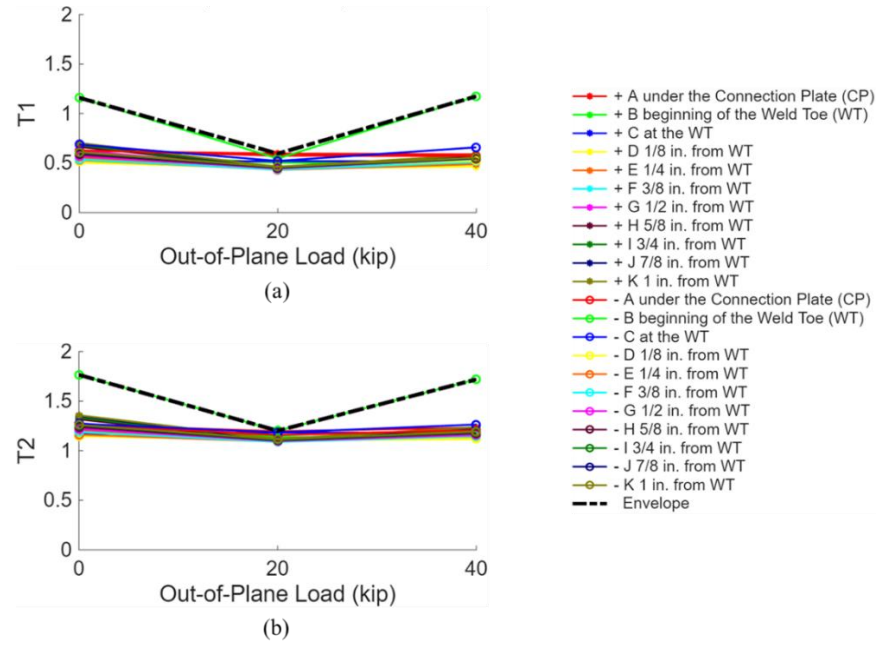

Source: FHWA.

Figure 34. Graph. Envelope of maximum values for the connection plate detail CP_{no_clip}, for varied out-of-plane force when the girder is under negative flexure – Hybrid girder case: (a) T_1; (b) T_2.

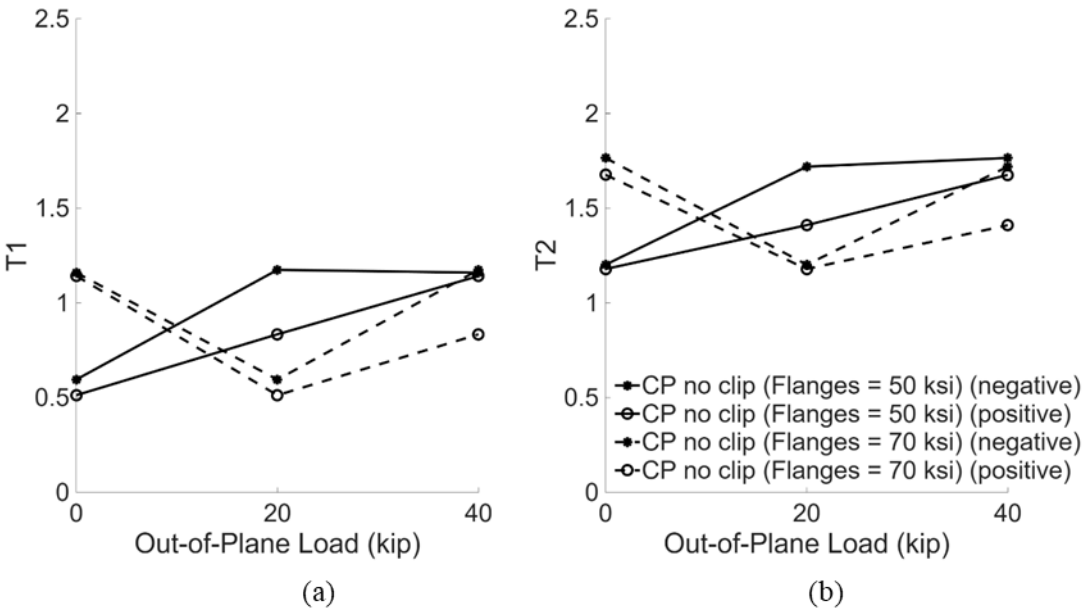

Source: FHWA.

Figure 35. Graph. Envelopes of maximum values comparing non-hybrid and hybrid girder cases: (a) T_1; (b) T_2.

Figure 36 and Figure 37 present data showing the influence of web thickness and weld size, respectively, on triaxiality in the proposed-practice connection plate detail. These data are computed for the case with no out-of-plane loading. The proposed-practice connection plate detail was found to be insensitive to both factors.

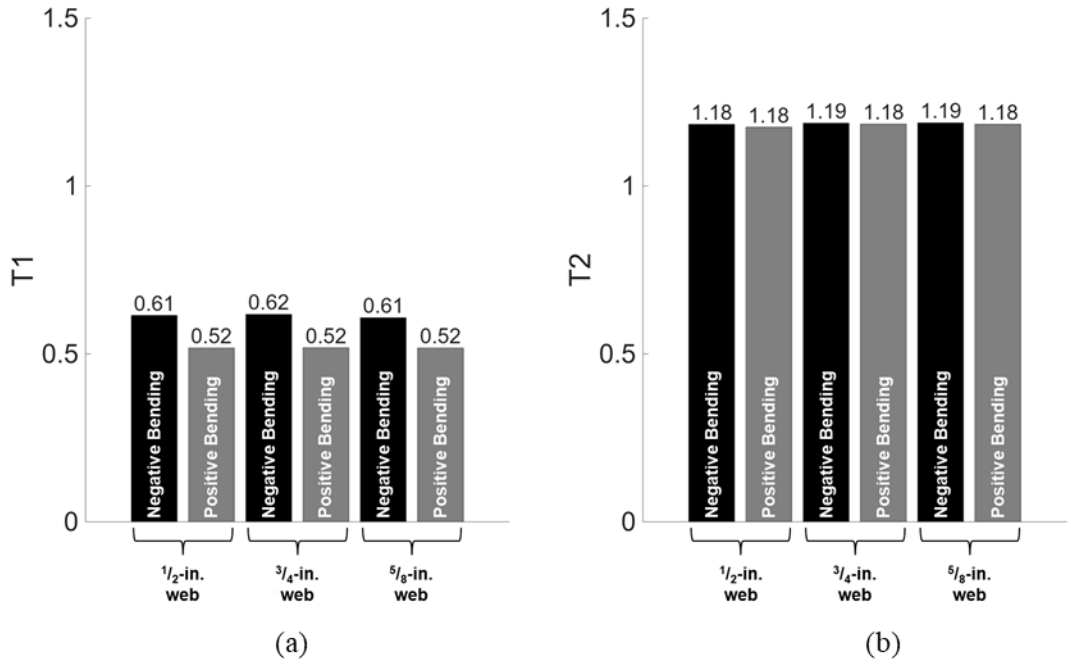

Source: FHWA.

Figure 36. Graph. Comparison of web thickness – CP $_{no\_clip}$: (a) T_1; (b) T_2.

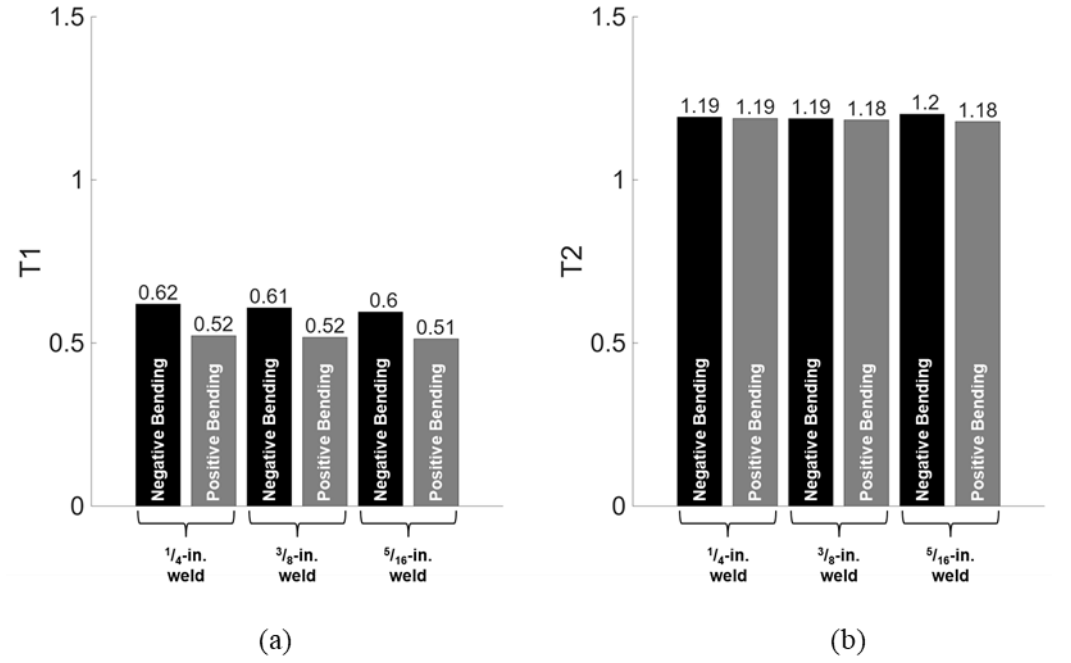

Source: FHWA.

Figure 37. Graph. Comparison of weld sizes – CP$_{no_clip}$: (a) T_1; (b) T_2.

4.2.2.4 Overall Comparison of Connection Plate Details

Figure 38 presents the T_1 and T_2 envelopes for each of the three connection plate details studied, for a non-hybrid girder with $^5/_8$-inch-thick web and $^5/_{16}$-inch weld. Overall, the historic-practice detail consistently produced the greatest triaxiality. The current-practice and proposed-practice details exhibited similar results. For all the details, there was a strong increasing trend associated with increased out-of-plane load magnitudes.

Overall, these data imply that there is not an increased risk of constraint-induced fracture in transitioning from current or historic connection plate details to the newly-proposed connection plate detailing practice.

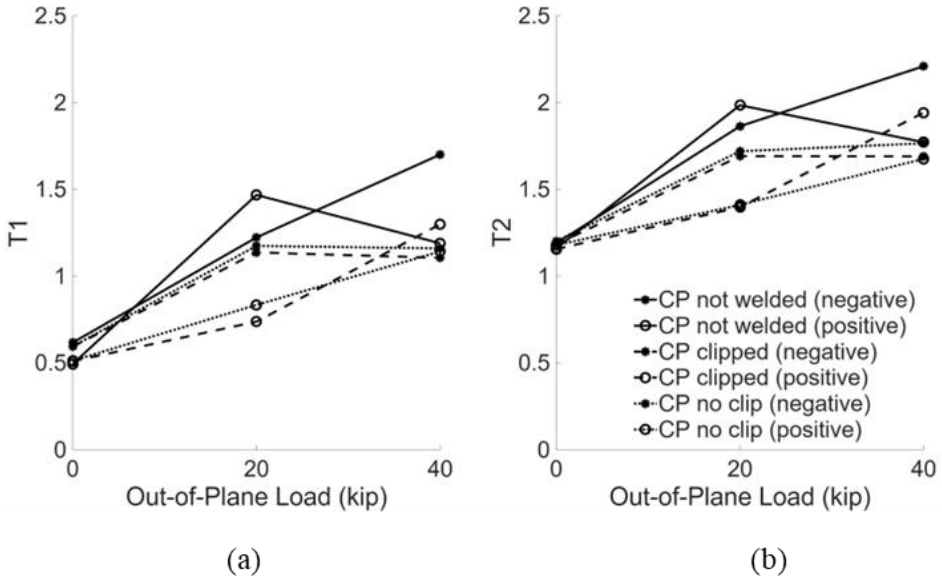

Source: FHWA.

Figure 38. Graph. Envelopes of maximum values for three connection plate detailing practices: (a) T_1; (b) T_2.

CHAPTER 5 - EXPERIMENTAL INVESTIGATION

This chapter describes the experimental investigation to characterize various steel bridge details for susceptibility to constraint-induced fracture.

5.1 EXPERIMENTAL APPROACH

A series of 16 experimental tests were conducted to characterize the strain and fracture response of CIF-sensitive attachment details subjected to tensile loading. The tests were performed on component-scale dogbone specimens. The test program captures a range of variables, including detail type, plate thicknesses, CRG dimensions, test temperature, inclusion of out-of-plane loading, and steel material properties. Fourteen specimens were tested at low temperatures (LT), and two were tested at room temperature (RT).

The specimens tested include:

- An orthogonal stiffener detail, in which a discontinuous transverse stiffener (DTS) is used to avoid a conflict with a longitudinal stiffener (two specimens);
- An orthogonal stiffener detail, in which a discontinuous longitudinal stiffener (DLS) is used to avoid a conflict with a transverse stiffener (eight specimens);
- A thick bearing stiffener detail, also serving as a connection plate (two specimens); and
- Two connection plate details (four specimens).

Half of the specimens in the experimental program were DLS details, which are known to be sensitive to CIF. This was done because prior research on this topic, which has been exclusively analytical, has not satisfactorily characterized the level of sensitivity of the DLS detail to CRG dimension. The intent of dedicating eight specimens to the DLS detail was to help close this research gap and to explore the role of test temperature and material properties on CIF sensitivity of the DLS detail.

The orthogonal stiffener specimens were subjected to longitudinal tension, applied parallel to the long axis of the dogbone specimens. The bearing stiffener and connection plate specimens were additionally subjected to a constant out-of-plane (OOP) tension force while the primary longitudinal tension was applied; this was done to mimic the presence of cross-frame forces acting laterally on the detail.

An overview of the test matrix is presented in Table 5-1.

The specimens were ordered from the fabricator in two batches, referred to as Batch 1 and Batch 2. The Batch 1 order included a subset of the total DTS, DLS, BS, and CP specimens tested. Since the main element of the DTS and DLS specimens were $^{3}/_{8}$-inch-thick plates and the main element of the BS and CP specimens were $^{1}/_{2}$-inch-thick plates, two different heats of steel were used in Batch 1 specimen fabrication. Similarly, another two different heats of steel were used in Batch 2 specimen fabrication. Details of the material properties for each are provided in Section 6.1.

Table 5-1. Experimental test matrix.

Specimen Name	Detail	Temperature Condition†	Steel Batch	OOP Loading (kips)
DTS0LT-1	Discontinuous transverse stiffener, 0-inch gap	Cooled to -60 °F	1	0
DTS1/2LT-1	Discontinuous transverse stiffener, $^1/_2$-inch gap	Cooled to -60 °F	1	0
DLS0LT-1	Discontinuous longitudinal stiffener, 0-inch gap	Cooled to -60 °F	1	0
DLS0LT-2	Discontinuous longitudinal stiffener, 0-inch gap	Cooled to -60 °F	2	0
DLS1/4LT-2	Discontinuous longitudinal stiffener, $^1/_4$-inch gap	Cooled to -60 °F	2	0
DLS1/4RT-2	Discontinuous longitudinal stiffener, $^1/_4$-inch gap	Room temperature	2	0
DLS1/2LT-1	Discontinuous longitudinal stiffener, $^1/_2$-inch gap	Cooled to -60 °F	1	0
DLS1/2LT-2	Discontinuous longitudinal stiffener, $^1/_2$-inch gap	Cooled to -60 F°	2	0
DLS1LT-2	Discontinuous longitudinal stiffener, 1-inch gap	Cooled to -60 °F	2	0
DLS1RT-2	Discontinuous longitudinal stiffener, 1-inch gap	Room temperature	2	0
BS0LT-1	Bearing stiffener, 0-inch gap	Cooled to -60 °F	1	20
BS1LT-1	Bearing stiffener, 1-inch gap	Cooled to -60 °F	1	20
CP1LT-1	Connection plate with 1-inch clip	Cooled to -60 °F	1	20
CP1LT-2	Connection plate with 1-inch clip	Cooled to -60 °F	2	30
CP0LT-1	Connection plate, no clip	Cooled to -60 °F	1	20
CP0LT-2	Connection plate, no clip	Cooled to -60 °F	2	30

† *Description of test temperature selection and rationale provided in Section 6.1.*

5.2 TEST SPECIMEN DESIGN

Test specimens were designed with the following principles:

- Triaxiality should be at a local and global maximum at the location of the detail being tested;
- Specimen fracture should not damage the frame components; and
- The connection between the specimen and frame should be able to develop the nominal yield strength of the specimen on its gross section.

To meet these design criteria, a series of finite element models were constructed in Abaqus Standard v. 2021.

Each dogbone specimen design used a large steel pin at the specimen ends. Thick cover plates were used at the specimen ends to protect against localized yielding. Using two sets of stiffeners (front and back) was found to increase the state of triaxiality at the region of interest and it maintained double symmetry to the specimen so there was no eccentric bending. To reduce stress concentrations at the truncation of the longitudinal attachments, the longitudinal attachments were extended to the cover plates (Figure 39).

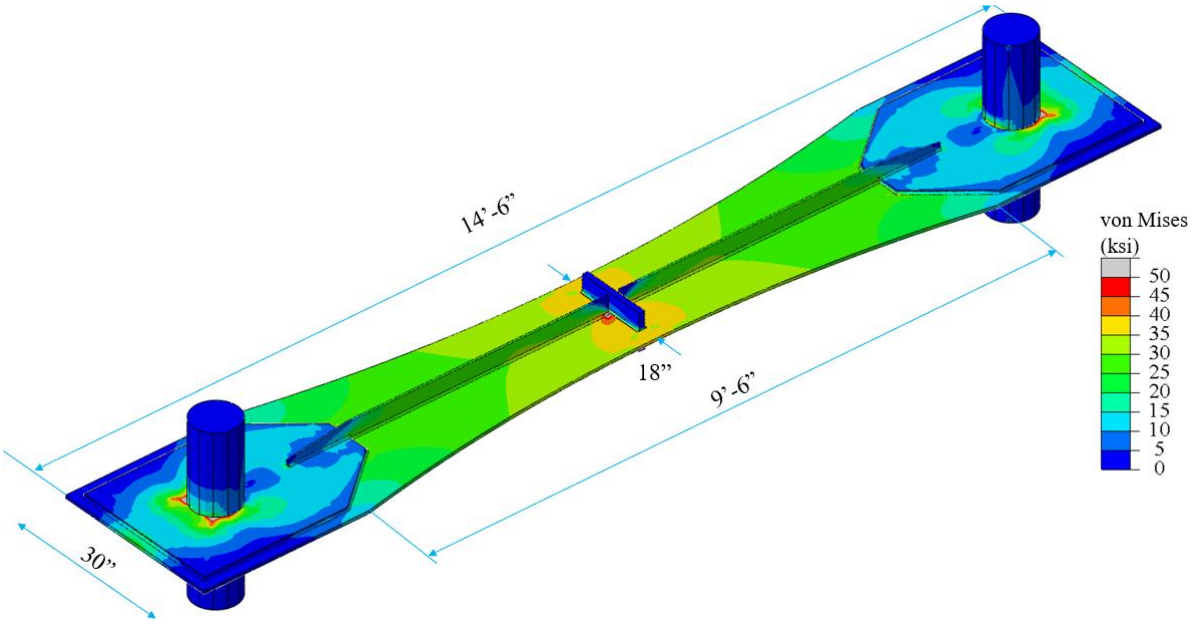

Source: FHWA.

Figure 39. Illustration. FE model results for specimen design.

The end result for predicted stress and triaxiality demand in the specimen is excellent, with peak demands for von Mises stress, T_1, and T_2 all located at the region of interest (Figure 40).

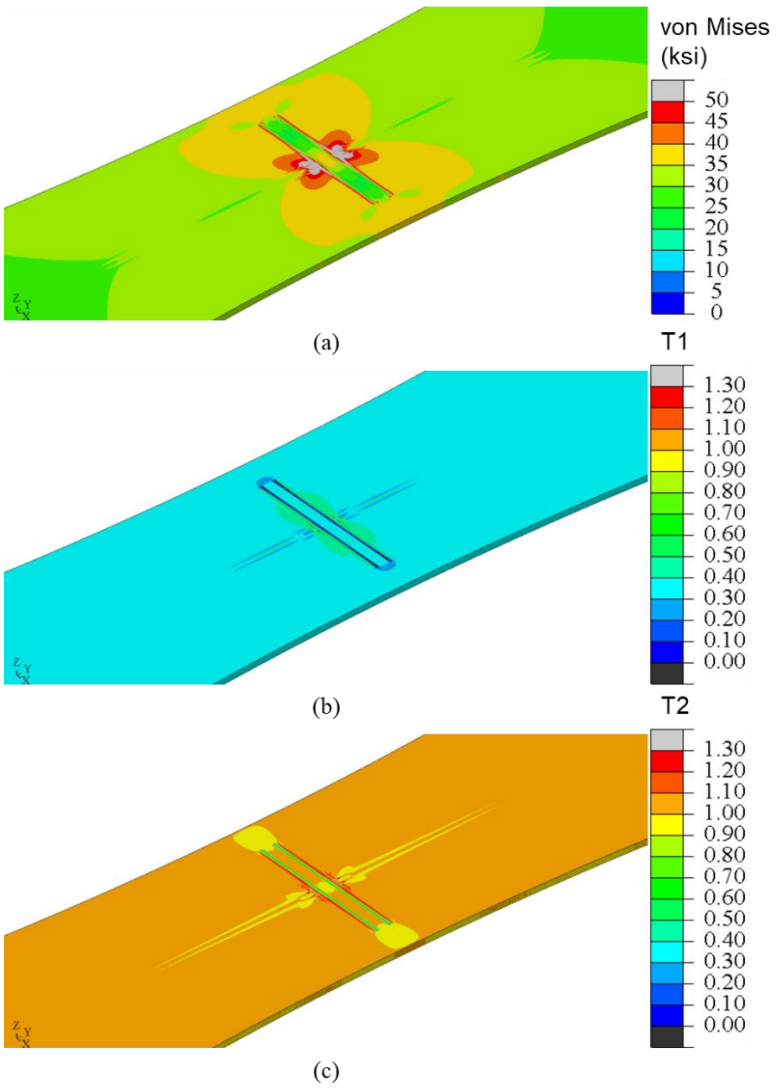

Source: FHWA.

Figure 40. Illustration. Computed demands in the specimen: (a) von Mises stress; (b) T_1; (c) T_2.

5.3 TEST SPECIMEN DETAILING AND FABRICATION

Component-scale dog-bone specimens used in this study are designed to mimic the behavior of details found on highway bridge structures. The primary steel element ("main plate," in Figure 41) of each specimen was designed to have a reduced section in the middle of the specimen. Welded attachments are connected to the main plate, localizing strains at the detail of interest during testing. Depending on the specimen, the main plate represents girder flanges or webs, while welded attachments represent stiffeners, connection plates, and/or girder webs. The longitudinal elements of the dog-bone specimens, comprising the total length of the specimens, are 14.5-ft long with a width of 30 inches at the specimen ends. The length of the reduced section is 9.5-ft with a constant radius of 273.75 inch All attachments project 3-6 inches from the surface of the dog-bone specimens, allowing for development of appropriate levels of constraint at the points of intersection. All specimens were fabricated from A709-50/50W steel. Specimens were

fabricated by a prominent bridge fabricator in Pennsylvania using qualified welding procedures and welders. All welding was performed with flux cored arc welding using electrodes with a minimum tensile strength of 70 ksi.

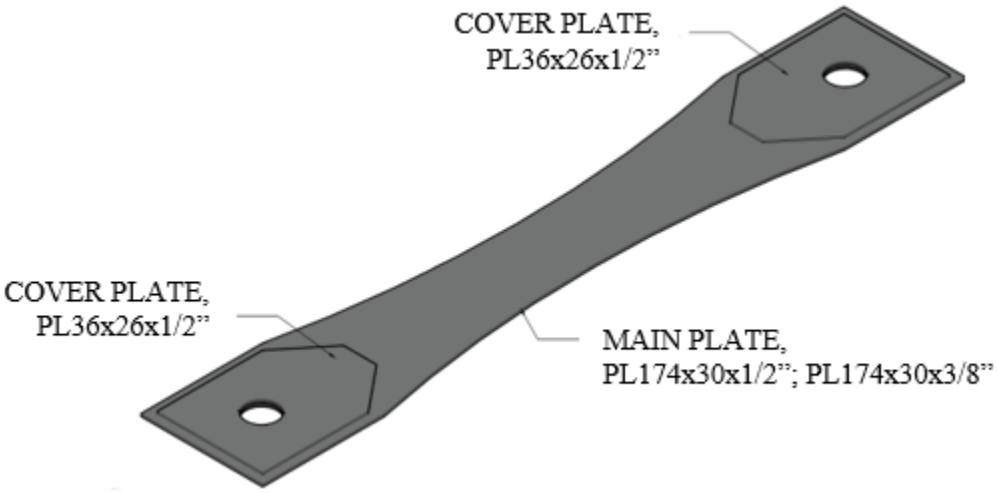

Source: FHWA.

Figure 41. Illustration. Specimen base dimensions.

5.3.1 Orthogonal Stiffener Detail (DTS and DLS):

Ten dogbone specimens with intersecting orthogonal stiffeners were fabricated for testing. The main plate in each of these specimens represents a girder web and is 18 x $^{3}/_{8}$ inch at the reduced section. Attachments oriented parallel to the direction of loading represent longitudinal stiffeners, while orthogonal attachments represent transverse stiffeners. Each stiffener is $^{1}/_{2}$-inch thick.

Two specimens are representative of a DTS detail (Figure 42), evaluating the behavior of two different constraint relief gap dimensions: weld toes touching (DTS0LT-1, Figure 42b), and a $^{1}/_{2}$-inch gap (DTS1/2LT-1, Figure 42c).

The remaining eight specimens were representative of a DLS detail (Figure 43a), enabling examination of the behavior of different CRG dimensions: weld toes touching (DLS0LT-1, DLS0LT-2, Figure 43b), a ¼-inch CRG (DLS1/4LT-2, DLS1/4RT-2, Figure 43c), a $^{1}/_{2}$-inch CRG (DLS1/2LT-1, DLS1/2LT-2, Figure 43d), and a 1-inch CRG (DLS1LT-2, DLS1RT-2, Figure 43e). These specimens were also used to vary test temperature and steel material properties in the test program.

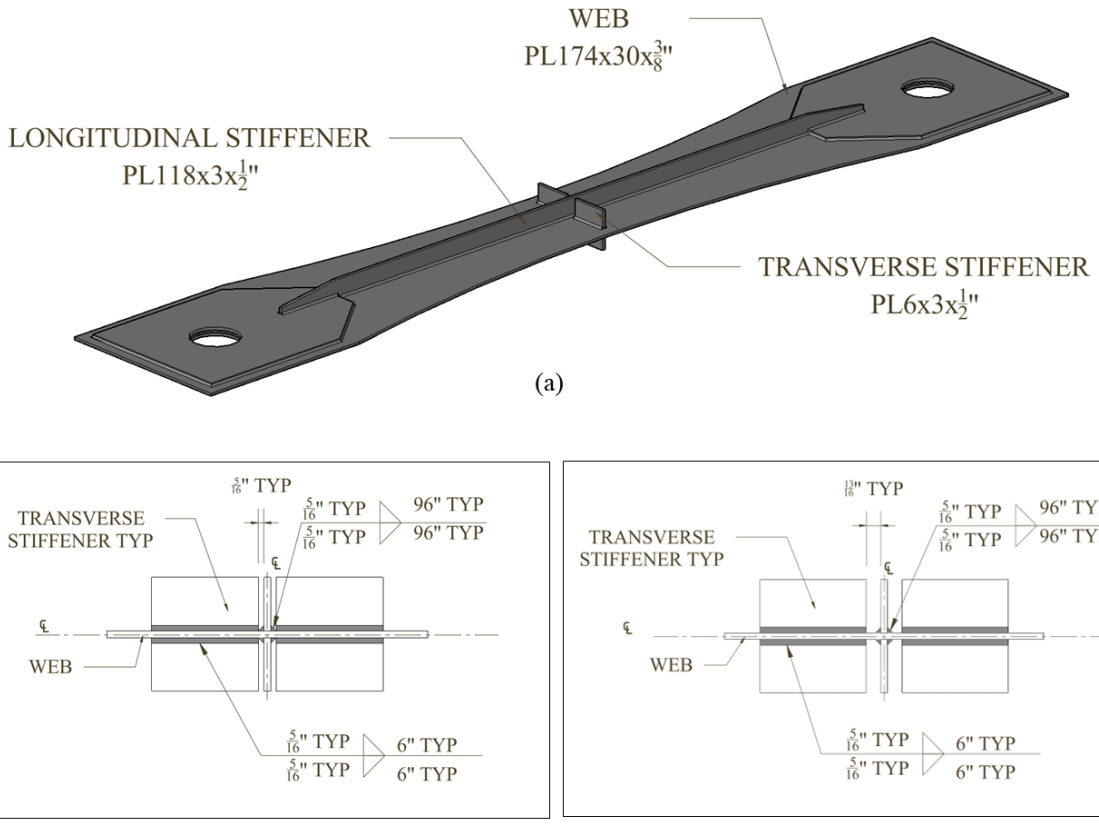

Source: FHWA.

Figure 42. Illustration. DTS specimens: (a) overall view; (b) detail with no CRG used in DTS0LT-1; (c) detail with ½-inch CRG used in DTS1/2LT-1.

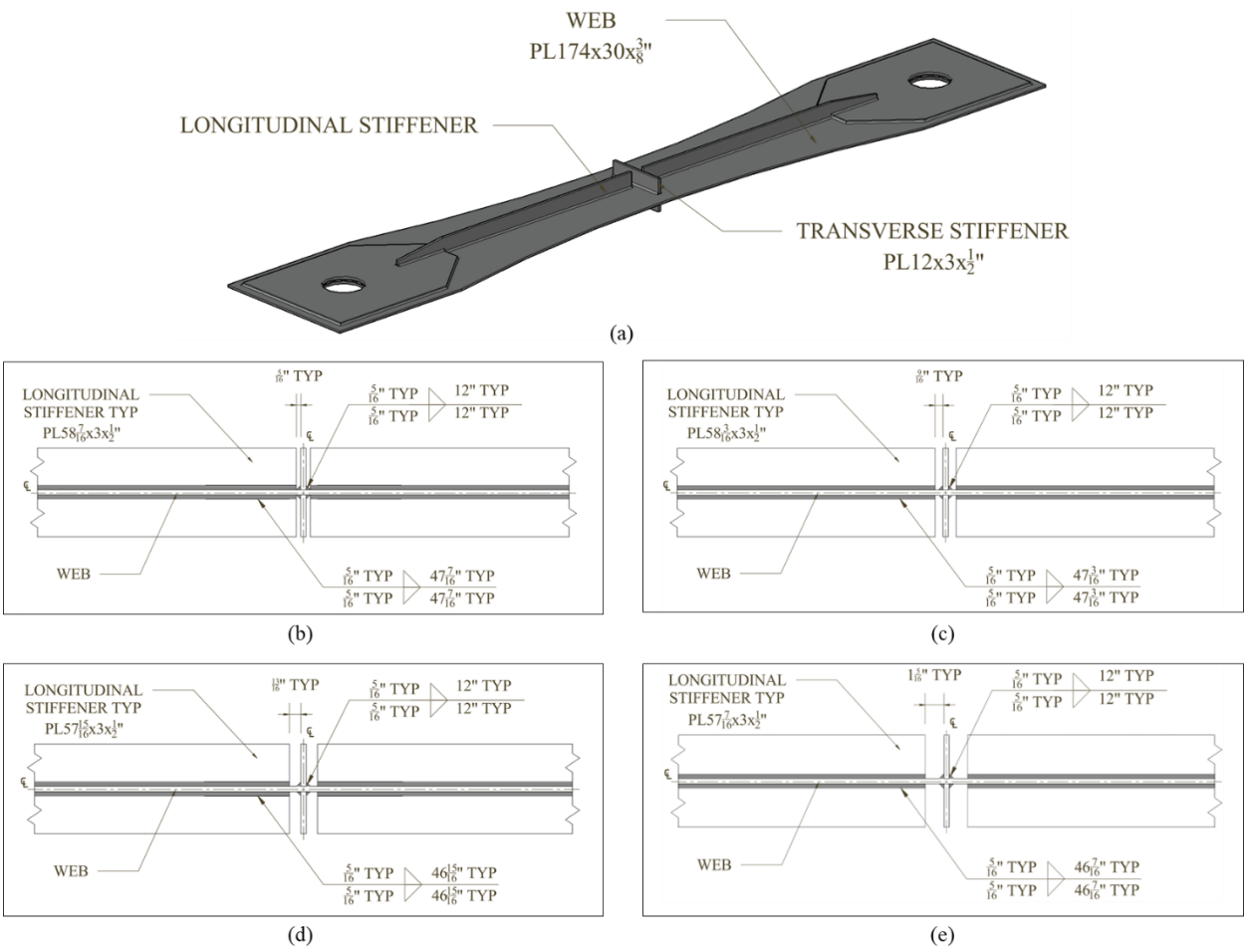

Source: FHWA.

Figure 43. Illustration. DLS specimens: (a) overall view; (b) detail with no CRG used in DLS0LT-1 and DLS0LT-2; (c) detail with 1/4-inch CRG used in DLS1/4LT-2 and DLS1/4RT-2; (d) detail with 1/2-inch CRG used in DLS1/2LT-1 and DLS1/2LT-2; (e) detail with 1-inch CRG used in DLS1LT-2 and DLS1RT-2.

5.3.2 Bearing Stiffener Detail:

Two dogbone specimens representative of a thick bearing stiffener detail also being used as a connection plate are shown in Figure 44. These specimens represent bearing stiffeners detailed using historic practices. The bearing stiffener being used as a CP is not attached the flange. The main plate in these specimens represents a girder flange and has dimensions at the reduced section of 18 x 1/2 inch. Welded attachments include a web plate attached along the longitudinal axis of the specimen and a bearing stiffener on either side of the web plate, oriented transverse to the direction of applied tensile load. The bearing stiffeners are 1 inch thick. Bearing stiffeners are attached only to the web plates, and tests evaluate the influence of the gap between stiffener and flange elements. One specimen has no gap (BS0LT-1, Figure 44b), while the second uses a 1-inch gap (BS1LT-1, Figure 44c).

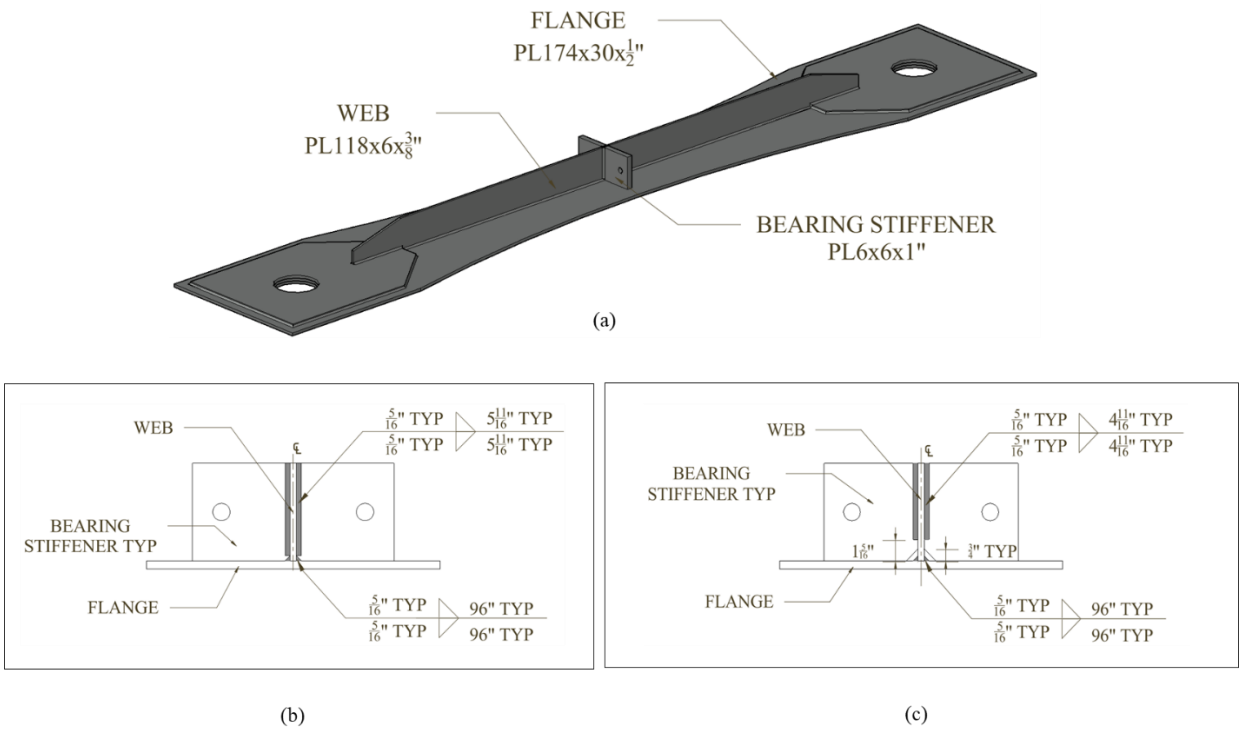

Source: FHWA.

Figure 44. Illustration. Bearing stiffener specimens: (a) overall view; (b) detail with no CRG used in BS0LT-1; (c) detail with 1-inch CRG used in BS1LT-1.

5.3.3 Connection Plate Details:

Four dogbone specimens representative of connection plate details were fabricated. The main plate in the CP specimens represents a girder flange and has a reduced section of 18 inches x 1/2 inch. Attachments include a web plate oriented parallel to the direction of load, and CPs oriented orthogonal to the longitudinal axis of the specimen. Two specimens represent current-practice detailing, in which the CP is clipped at the junction of the web and flange (CP1LT-1, CP1LT-2), while the other specimen represents proposed-practice detailing, in which the CP is welded into the corner of the web to flange junction (CP0LT-1, CP0LT-2). These specimens were also used to vary steel material properties within the experimental test matrix.

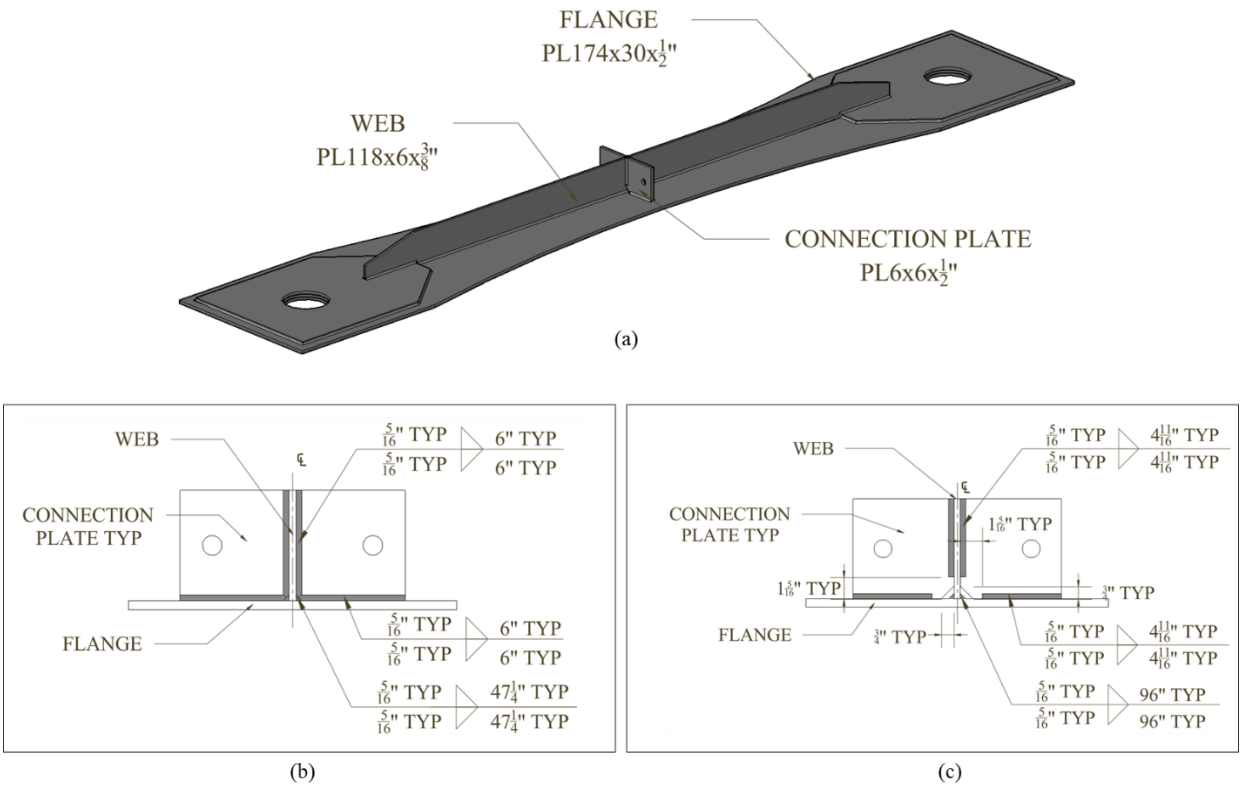

Source: FHWA.

Figure 45. Illustration. Connection plate specimens: (a)overall view; (b)detail view of CP0LT-1 and CP0LT-2; (c) detail view with clipped connection plate used in CP1LT-1 and CP1LT-2.

5.4 TEST SET-UP AND LOAD FRAME

The self-reacting loading apparatus used to apply tension to each specimen (Figure 46 and Figure 47) consisted of two pairs of W36x256 reaction beams that sandwiched the grip ends of the dog-bone tension specimen. An 8-inch diameter pin passing through each end of the dogbone specimen beared on the pair of W36x256 reaction beams during loading. A pair of hydraulic jacks was installed between the two reaction beams, and as the hydraulic jacks were extended, they pushed the two reaction beams apart via four W14x132 jack beams, inducing tensile loads on the specimen. The hydraulic pumps were controlled with an analog controller and powered with an electric pump.

The loading apparatus and installed specimen lay flat on the laboratory floor, and the two reaction beams were allowed to slide apart along the floor during loading. The entire setup was secured to the floor using a restraining rail system that allows movement in the direction of the loading jacks but ensures the frame cannot "jump" during a fracture event. Large sandbags were placed at each end of the testing apparatus to catch the specimen upon fracture.

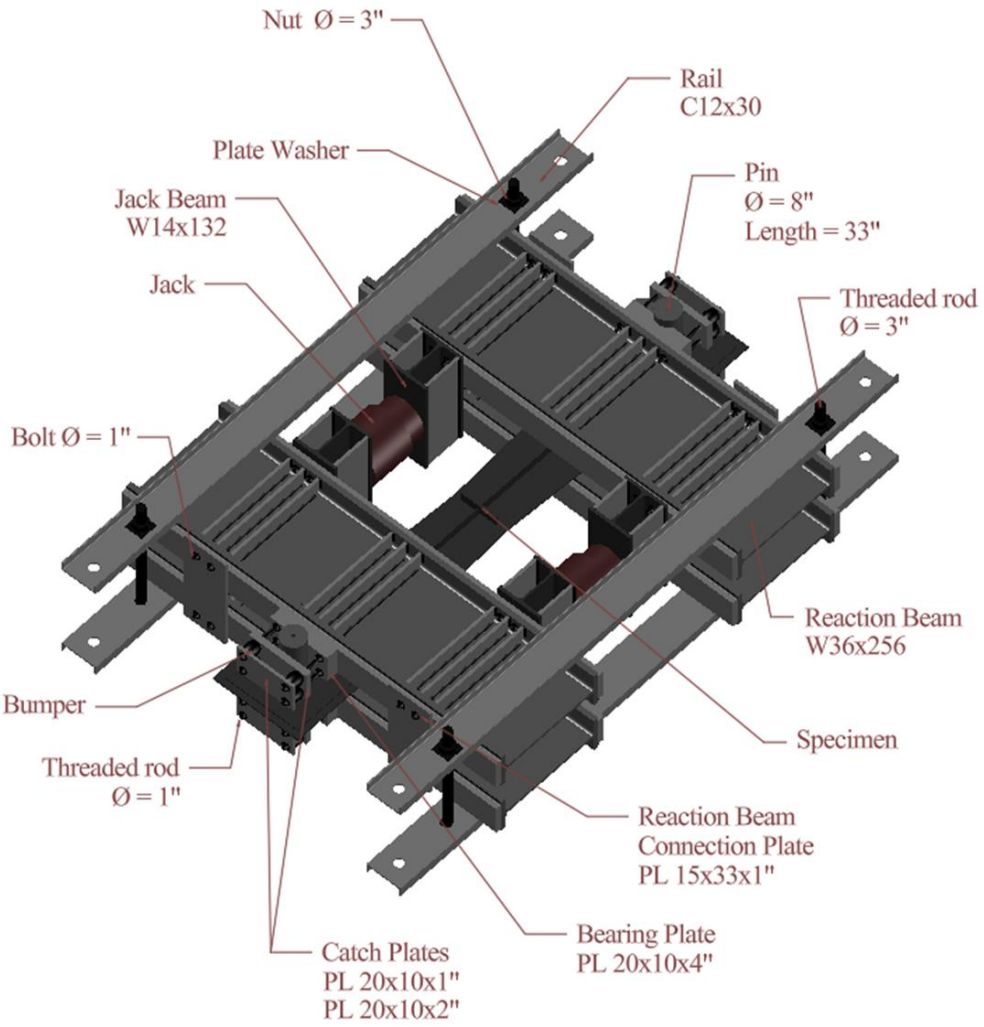

Source: FHWA.

Figure 46. Illustration. Schematic of load frame with tension specimen.

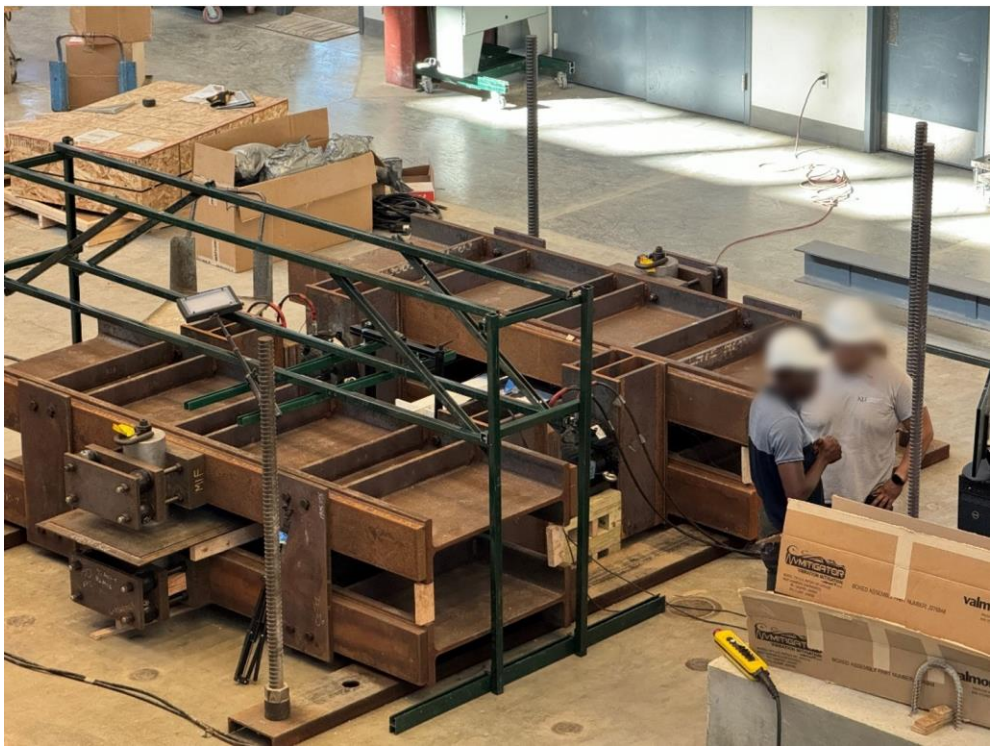

Source: FHWA.

Figure 47. Photograph. Primary load frame with installed tension specimen.

5.4.1 Out-of-Plane Loading Setup

Bearing stiffener and connection plate specimens were loaded with a constant out-of-plane force while they were subjected to the monotonically-increasing primary longitudinal tension force, to mimic the presence of cross-frame forces. To accomplish this, a secondary independent self-reacting load frame that nested within the main loading apparatus was utilized (Figure 48). The specimen was bolted to a steel bar through each connection plate, and the bars were in turn connected back to the self-reacting load frame. A tensioning nut with multiple small jackbolts was attached through an assemblage to one of the steel bars, and as the jackbolts were tightened it applied tension force through the connection plates. An inline donut-style load cell ensured the appropriate out-of-plane tension force was applied, which was 20 kips or 30 kips depending on the specimen. Once the out-of-plane force was applied to a specimen, the secondary load frame remained in place during the primary tension loading so that the out-of-plane force was held constant during the test.

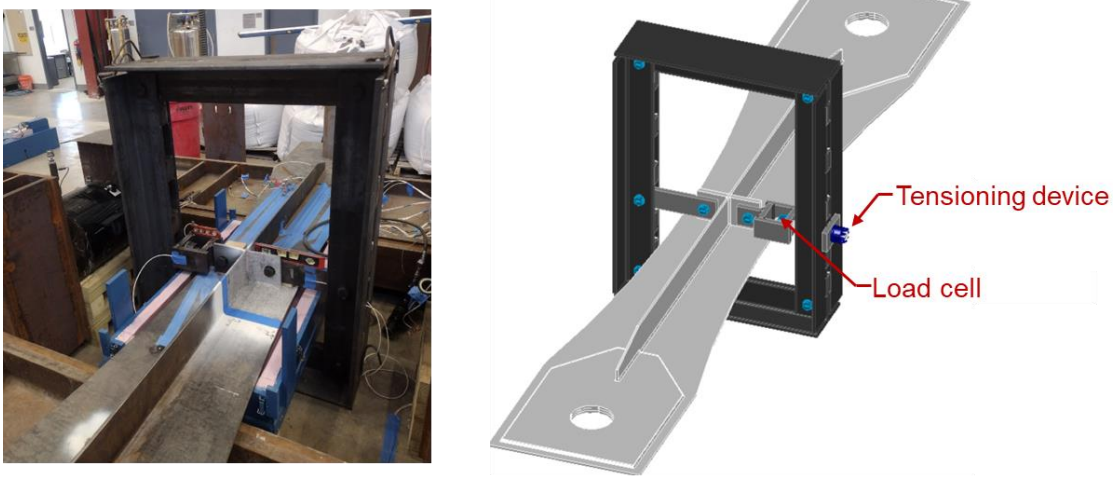

(a) (b)

Source: FHWA.

Figure 48. Illustration. Secondary loading apparatus for applying a constant out-of-plane force to BS and CP specimens: (a) photograph of test setup; (b) schematic of test setup.

5.5 INSTRUMENTATION

Each of the large-scale specimens was painted with a high-contrast speckle pattern over a white painted background to enable use of digital image correlation (DIC) measurements during the test. DIC was used to measure the strain field during each test, allowing comparison with and validation of the finite element models. Figure 49 shows a view of the test setup with DIC lighting and cameras mounted on scaffolding that spans across the primary loading frame.

Source: FHWA.

Figure 49. Photograph. View of test setup showing DIC lighting and cameras on scaffolding and cold box.

Because the majority of the specimens were tested at low temperature and soaked at -60 °F for approximately 15-20 minutes before loading, the steel surfaces developed a great deal of frost upon removal

of the cold box lid, as warmer air contacted the cold steel and produced condensation. The presence of frost obfuscated the painted speckle patten. Therefore, the frost was manually removed during testing using a spray bottle of isopropyl alcohol and a dustcloth, both operated from a distance of approximately 10 ft for safety reasons.

In addition to using DIC for strain measurements during testing, bondable strain gauges and strain gauge rosettes were deployed as shown in Figure 50. Thermocouples were also deployed on the specimen at the detail of interest to record test temperature. A data acquisition system was used to collect strain and temperature information.

One strain gauge rosette in particular, Ro2, is used as a reference throughout the results. Ro2 was located 2 inches from the surface of the longitudinal attachment (web or longitudinal stiffener, depending on the specimen) and 2 inches from the surface of the orthogonal attachment (transverse stiffener, connection plate, or bearing stiffener, depending on the specimen).

The thermocouple used for temperature control during cooling of low-temperature tests and measurement of temperatures at the detail of interest was located 1 inch from the surface of the transverse attachment (transverse stiffener, connection plate, or bearing stiffener), and 5 inches from the surface of the longitudinal attachment (web or longitudinal stiffener).

Overall force and displacement were monitored during testing. Force was measured using a pressure transducer installed at each hydraulic jack. Specimen deformation was measured using a string potentiometer that spanned the exposed length of the dogbone, which corresponded with a 40-inch gauge length (Figure 51). The string potentiometer interfered with placement of the cold box; therefore, for low-temperature tests, the string potentiometer was quickly installed after the top lid of the cold box was removed, before loading.

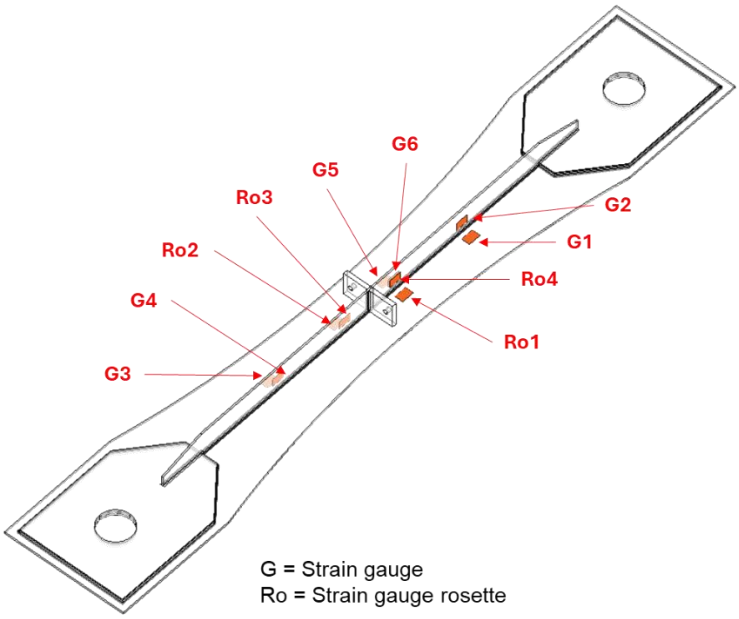

Source: FHWA.

Figure 50. Illustration. Strain gauge distribution.

Source: FHWA.

Figure 51. Photograph. String potentiometer installed on a test specimen.

5.6 TEST INSTALLATION

Figure 52 shows one of the custom-fabricated insulated cold boxes used to cool specimens during testing at the location of the detail of interest. The cold box fit over the welded attachments and liquid nitrogen was pumped into the enclosure and circulated using a fan. The entry rate of the liquid nitrogen into the chamber was controlled using a digital controller so that the target temperature in the specimen was reached. Immediately before testing, the top of the cold box was removed, exposing the top surface of the specimen so that DIC measurements can be made. The soaking temperature for all low-temperature tests was -60 °F, corresponding to Zone III minimum service temperature. See Section 6.1 for further discussion on why this test temperature was chosen relative to the impact energy to steels used to fabricate the specimens.

For specimens subjected to an out-of-plane force in addition to primary longitudinal tension, the out-of-plane tensioning step was conducted before the cold box was installed. A special cold box was used for those specimens that allowed the tensioning system to pass through the sides of the cold box.

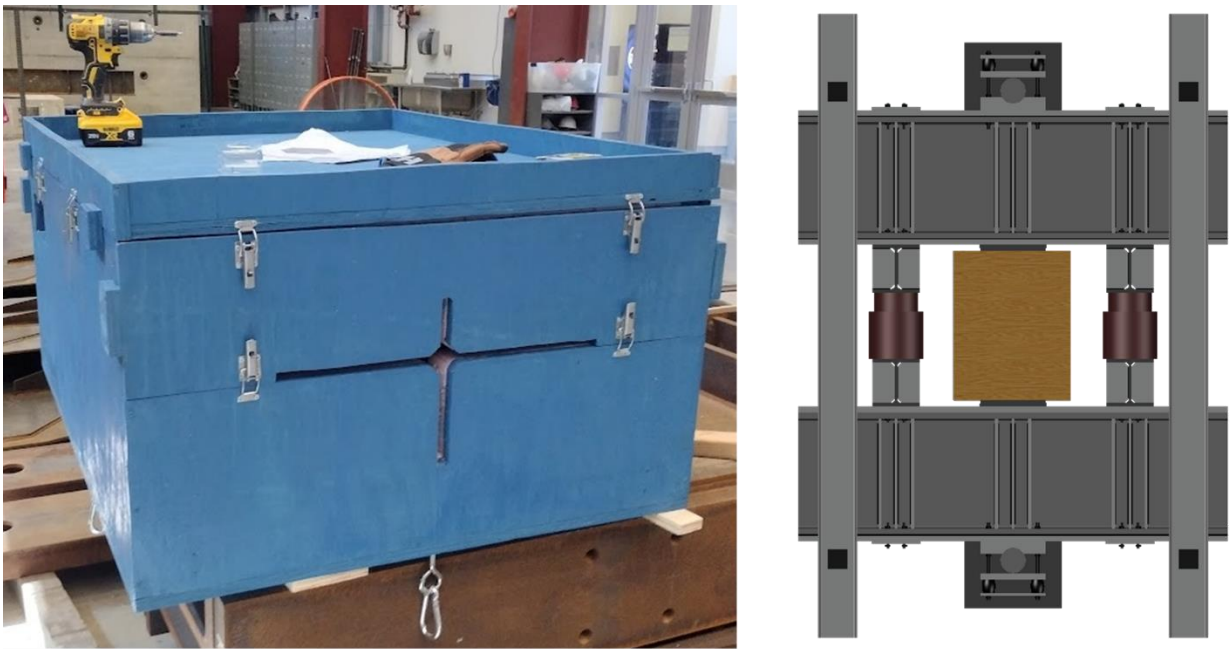

(a) (b)

Source: FHWA.

Figure 52. Photograph. Cold temperature application: (a) fabricated cold box; (b) cold box around specimen in the test setup.

Figure 53 shows the as-received steel dog-bone specimens.

Source: FHWA.

Figure 53. Photograph. Dog-bone specimens in the KU West Campus Structural Testing Laboratory.

CHAPTER 6 - EXPERIMENTAL RESULTS AND DISCUSSION

6.1 MECHANICAL TEST RESULTS

Four heats of steel were used in this test program: two heats (Batch 1 and Batch 2) of $^3/_8$-inch thick steel used as the main plate in the DTS and DLS specimens, and two heats (Batch 1 and Batch 2) of $^1/_2$-inch thick steel used as the main plate in the bearing stiffener and connection plate specimens. All steel was A709-50/50W. The tensile mechanical properties for the main plates are presented in Table 6-1 from provided Mill Test Reports (MTRs). The 1-inch thick bearing stiffener material had a yield strength of 58 ksi, ultimate strength of 78 ksi, and elongation of 26%.

Table 6-1: Tensile mechanical properties.

Batch	Thickness (inch)	F_y (ksi)	F_u (ksi)	Elongation (%)
1	$^3/_8$	56	74	26
1	$^1/_2$	58	80	31
2	$^3/_8$	51	79	24
2	$^1/_2$	52	73	23

The material used for the primary plates in each CIF specimen was characterized in terms of Charpy V-notch (CVN) impact energy.

CVN impact specimens were fabricated from a representative plate provided for each of the four heats of steel included in this study. All specimens were sampled in the L-T orientation, such that the longitudinal axis of each specimen corresponded to the direction of plate rolling, indicated by the "L" designation. Notches were oriented such that fracture propagated transverse to the rolling direction of the plate, indicated by the "T" designation. Given the thicknesses of the plates under consideration, all specimens were sampled from plate mid-thickness. Plates of $^1/_2$-inch thickness allowed for full-size CVN specimens with dimensions of 0.394 x 0.394 x 2.165 inches. Plates of $^3/_8$-inch thickness required the utilization of sub-size specimens with dimensions of 0.354 x 0.394 x 2.165 inches. Notches were fabricated in all specimens in accordance with ASTM E23-24 (ASTM, 2024b), producing a remaining ligament of 0.315 inches.

CVN impact specimens were tested over a range of temperatures to develop full temperature-transition curves. Testing was conducted at each of the three AASHTO minimum service temperatures (MSTs) of 0, -30, and -60 °F, as well as at the prescribed test temperatures of 10, 40, and 70 °F. Additional test temperatures were then selected to more fully characterize behavior throughout the lower shelf, transition, and upper shelf behavior regions. Five-parameter sigmoid curves were then fit to the impact energy data, allowing for a visual representation of the different behavior regimes.

The CVN impact energy test results for the $^3/_8$-inch-thick plate are shown in Figure 54, and the results for the $^1/_2$-inch-thick plate are shown in Figure 55. Results for the sub-size specimens in Figure 65 have no size correction applied. Both figures show the CVN values reported in the MTRs received from the manufacturer for just the second batch specimens. No MTR impact energy data was available for the first batch. Also shown in Figure 54 and Figure 55 are the AASHTO Zones I, II, and III minimum average impact energy requirements as per ASTM A709 (ASTM, 2024a). Minimum requirements are specified for both members not requiring fracture control practice (lower line) and members requiring fracture control practice (upper line).

All four heats of steel exhibit impact behavior significantly greater than the minimum requirements, with all materials in the upper transition region or on the upper shelf specified test temperatures. Although impact energy values vary significantly at the upper shelf, especially for the $^1/_2$-inch-thick material, behavior at service temperatures was less variable. The two different heats of both the $^3/_8$-inch- and ½-inch-thick material exhibited nearly identical behavior at the Zone III MST of -60 °F. Behavior diverged slightly at

warmer temperatures, but at the Zone II MST of -30 °F, the variability between heats of the same thickness are well within expected scatter of impact energy results. Zone I MST behavior for the 3/8-inch-thick materials is essentially the same when comparing the first and second batches of material. This does not hold true for the 1/2-inch-thick materials. At 0 °F, the first batch of the 1/2-inch material remained consistently within the lower transition region, while the second batch showed significant variability at this test temperature with impact energy between 95 and 253 ft-lbf exhibited. This behavior is significant in providing context to CIF specimen test results, as most low temperature testing occurred between Zones II and III service temperatures, where there was little difference observed in the impact energy between the different heats of steel. With low temperature results near the specified minimum impact energy requirements, and room temperature results on the upper shelf, the selected test temperatures for large-scale CIF specimens bound the behavior that would be exhibited on in-service structures.

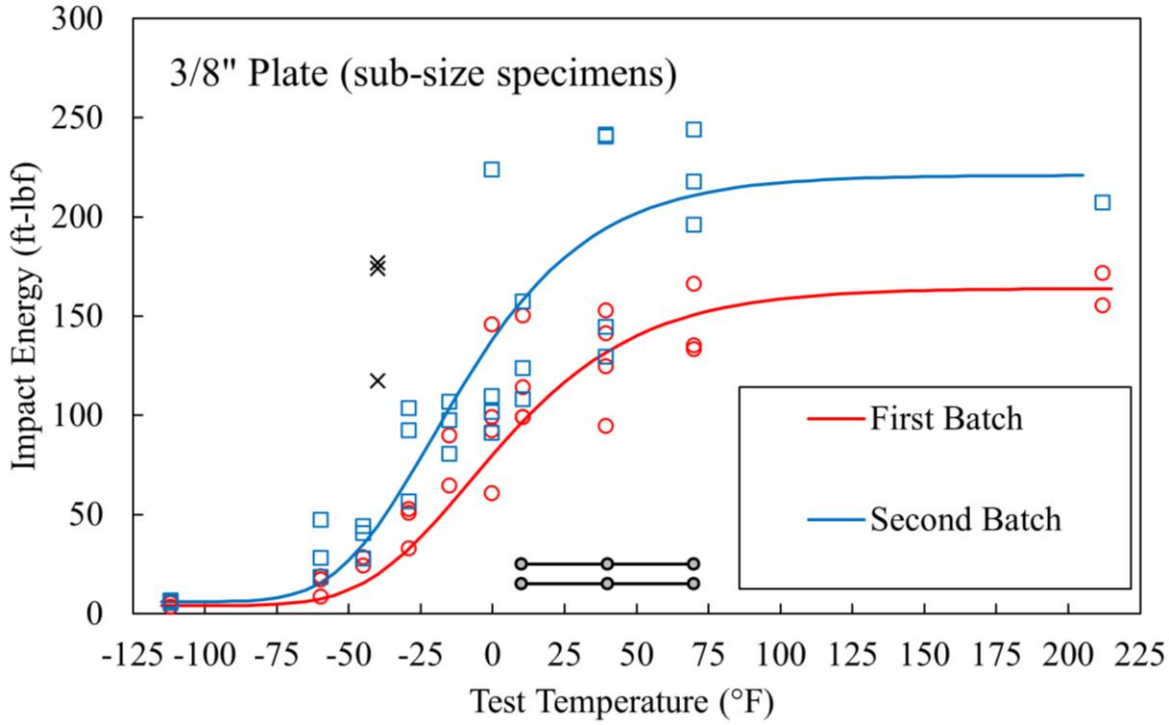

Source: FHWA.

Figure 54. Graph. CVN test results for 3/8-inch plate used DTS and DLS specimens.

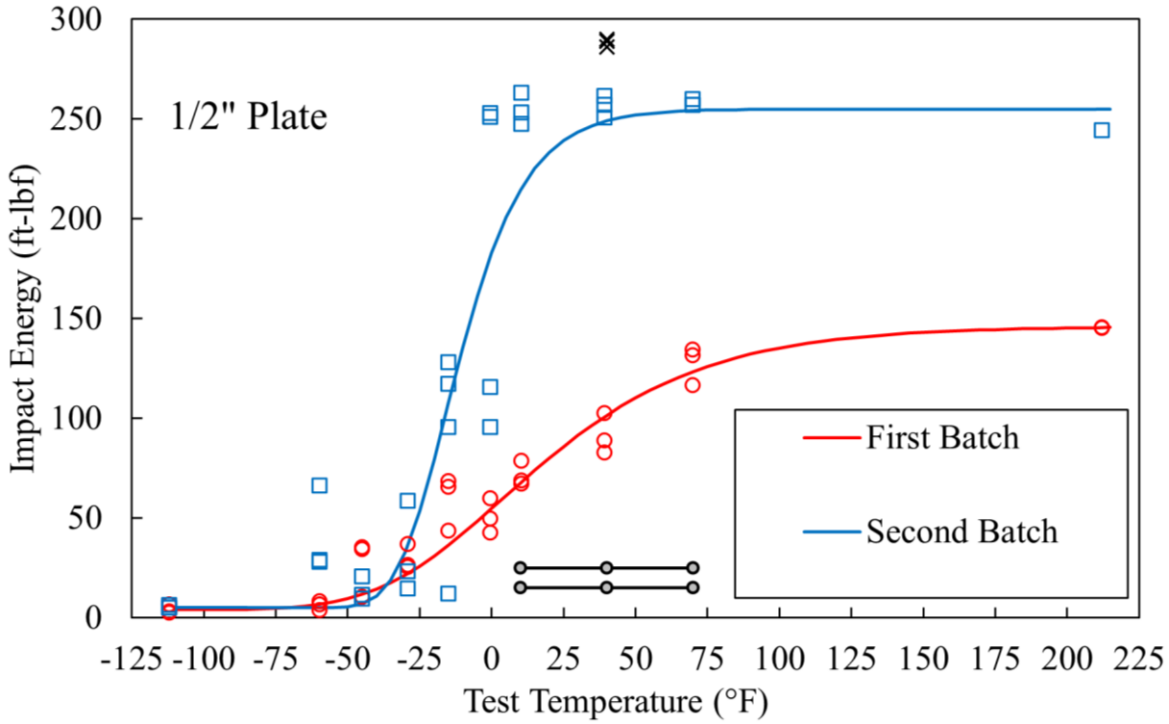

Source: FHWA.

Figure 55. Graph. CVN test results for 1/2-inch plate used BS and CP specimens.

6.2 SUMMARY OF EXPERIMENTAL RESULTS

Table 6-2 presents a summary of experimental results for all specimens tested.

Maximum load is reported for each specimen, corresponding with the maximum force sustained by the specimen before fracture (including pop-in fractures, which were taken as failure even if the specimen remained intact) or the test was stopped. The displacement corresponding with maximum load is reported, providing a general measure of ductility. A binary observation of whether fracture occurred in each specimen is reported, and occurrences of pop-in fractures before complete fracture are denoted with an asterisk symbol.

Table 6-2 also presents the time to maximum load and temperature recorded by the thermocouple closest to the center of the specimen at that time. The average CVN energy is reported for each specimen using the CVN characterizations in Figure 54 and Figure 55 to infer the CVN energy at the temperature corresponding with maximum load.

Multiple measures of strain were collected during the test, including DIC-based strain measurements and strain measurements from bondable gauges and rosettes. In addition to presenting the strain at maximum load as measured from the DIC system, Table 6-2 also shows a comparison of strains in the longitudinal direction, ε_1, as measured from strain gauge Ro2 and the DIC system at the time associated with the last measurement from Ro2 before gauge failure (computed at the same location as the center of Ro2). The DIC system was able to produce strain measurements beyond the point at which the bondable strain gauges failed, and it provides the most consistent measure of strain at failure from the test program. To compare the fidelity of the DIC strain measurements with bondable strain gauge measurements, data from gauge Ro2 and DIC at that location are provided at comparable timestamps.

The results are explored further by specimen type in Sections 6.3.1 (DTS specimens), 6.3.2 (DLS specimens), 6.4 (bearing stiffener specimens), and 6.5 (connection plate specimens).

Table 6-2. Summary of experimental results for all specimens.

Specimen Name	Maximum load (kips)	Displacement at maximum load (inch)	Brittle Fracture?	Temperature at max load (° F)	Time to maximum load (min)	Average CVN energy at maximum load (ft-lbf)	DIC strain at maximum load, at Ro2 (%)	Maximum Ro2 strain (%)	Time to maximum Ro2 strain (min)	DIC strain corresponding to Ro2 (%)
DTS0LT-1	464	1.55	No	-1	11.2	76	—	1.370	6.0	1.357
DTS1/2LT-1	452	1.42	No	26	9.3	118	2.188	0.673	3.1	0.554
DLS0LT-1	209	0.04	Y	-27	1.5	35	0.160	0.300	1.5	0.160
DLS0LT-2	341	0.26	Y	-23	2.6	19	2.363	1.061	2.1	1.196
DLS1/4LT-2	277	0.08	Y*	-52	1.9	33	1.118	0.954	1.9	1.118
DLS1/4RT-2	287	0.18	Y*	71	2.3	211	1.898	2.621	2.7	2.695
DLS1/2LT-1	305	0.19	Y	-10	2.6	42	1.446	1.767	2.5	1.128
DLS1/2LT-2	330	0.24	Y	-32	3.9	62	3.067	1.676	3.3	1.432
DLS1LT-2	348	—	Y	-35	4.4	55	5.022	3.469	3.8	3.229
DLS1RT-2	321	0.39	Y*	74	3.6	212	5.564	2.27	2.9	2.723
BS0LT-1	562	1.48	No	-29	11.3	27	3.087	1.236	6.4	1.598
BS1LT-1	581	1.83	No	-24	13.1	23	3.844	0.984	5.1	1.227
CP1LT-1	533	1.20	No	-35	11.1	18	2.314	0.837	5.6	0.976
CP1LT-2	525	1.21	No	-42	10.6	10	—	0.591	3.9	0.968
CP0LT-1	545	1.53	No	-21	11.5	29	2.673	1.191	6.6	1.360
CP0LT-2	571	1.97	No	-28	15.9	40	4.093	0.815	4.3	1.088

— Indicates no data for table entry.

** Indicates pop-in fracture. Maximum loads are based on load at pop-in (first) fracture.*

6.3 ORTHOGONAL STIFFENER DETAIL (DTS AND DLS)

Results for the DTS and DLS orthogonal stiffener specimens are presented and discussed in this section.

6.3.1 DTS Detail

Two discontinuous transverse stiffener specimens were tested: DTS0LT-1 and DTS1/2LT-1, pictured in Figure 56. DTS0LT-1 and DTS1/2LT-1 were both soaked at -60 °F before loading. The load-deformation results for the DTS specimens are shown in Figure 57; neither specimen experienced fracture, and both were loaded until a bearing failure was apparent at the loading pins, at which point the tests were stopped.

(a) (b)

Source: FHWA.

Figure 56. Photograph. Discontinuous transverse stiffener specimens: (a) DTS0LT-1; (b) DTS1/2LT-1.

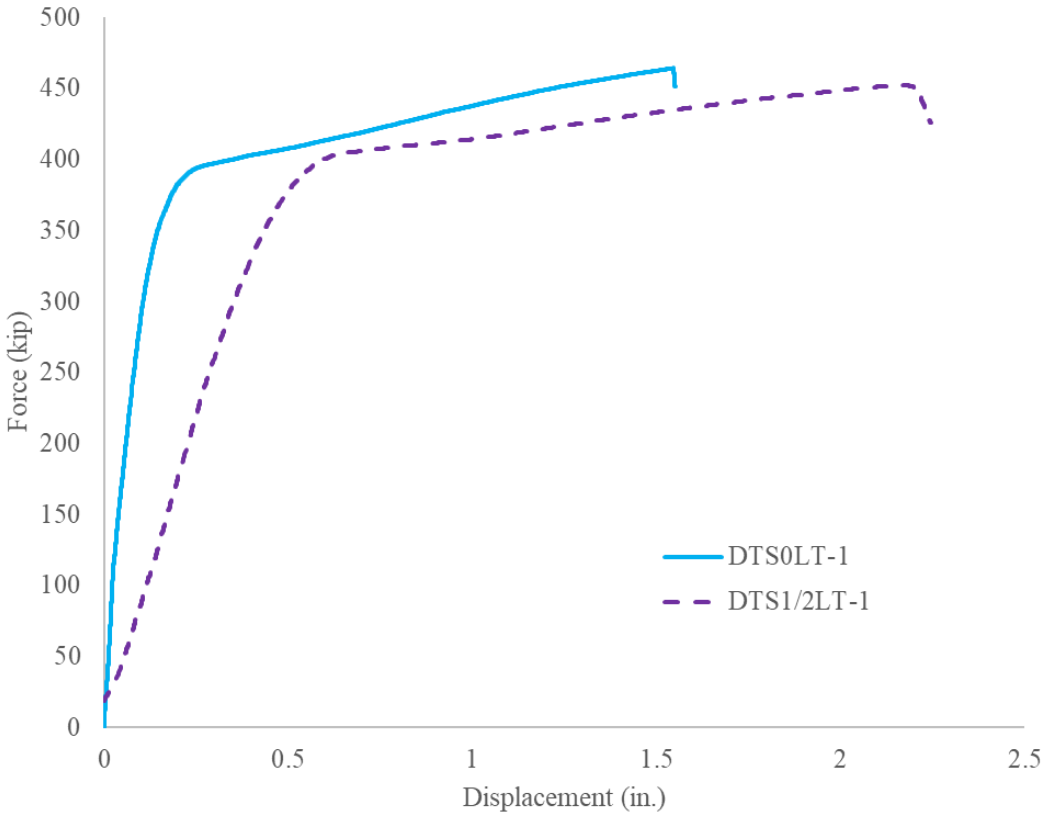

Source: FHWA.

Figure 57. Graph. Load-displacement records for DTS specimens.

Displacement measurements for DTS1/2LT-1 were collected with the string potentiometer attached to the frame rather than the specimen itself; this is a deviation from the general instrumentation description provided in Section 5.5. DTS1/2LT-1 was the first specimen tested in the experimental program, and this approach was initially taken with the goal of utilizing as long a gauge length as possible (pin to pin on the tension specimen) and the knowledge that the stiff loading frame was unlikely to contribute meaningful error through frame compliance at midspan. However, deformations in the 8-inch diameter holes in the specimen at the loading pins became significant at high loads, and this approach was abandoned after testing DTS1/2LT-1 in favor of attaching the string potentiometer directly on subsequent specimens and utilizing a shorter gauge length. Therefore, the load displacement curve for DTS1/2LT-1 includes displacements from bearing failures at the holes at the specimen ends and is measured over a longer gauge length than other specimens. The bearing displacements have been corrected for (removed) in the reported total displacement in Table 6-2, but could not be removed from the complete load-displacement record. This explains the difference in the load-displacement records for DTS0LT-1 and DTS1/2LT-1 that is apparent in Figure 57.

Figure 59 shows the longitudinal strains at maximum load from the DIC measurements. The DIC coating on DTS0LT-1 failed completely shortly before the test was ceased; therefore, Figure 58 shows a comparison of the DIC results at an earlier loading point corresponding with 55% of nominal yield on the gross section of the specimen. While the data for DTS0LT-1 are sparse, the data for DTS1/2LT-1 show no isolated severe hot spots.

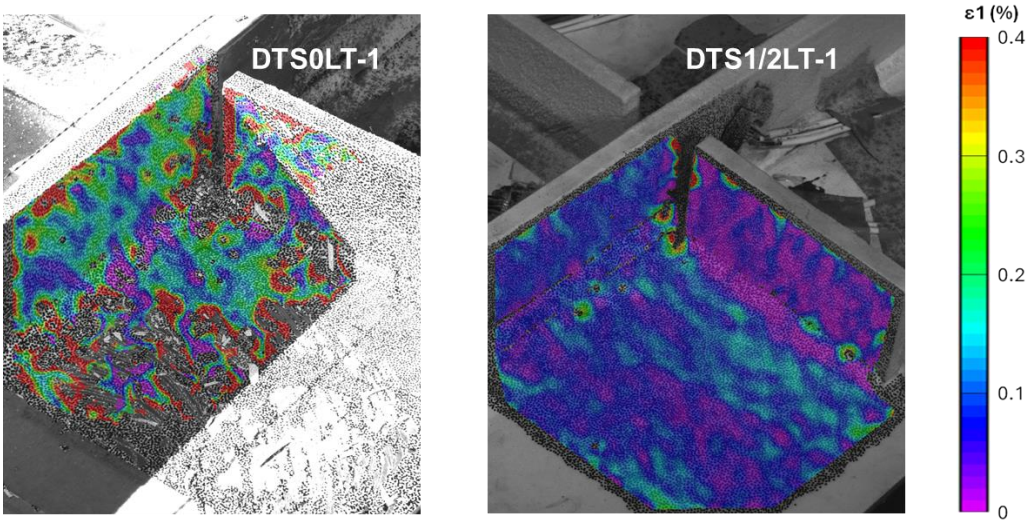

Source: FHWA.

Figure 58. Photograph. Strains at 55%F_y: DTS0LT-1 and DTS1/2LT-1.

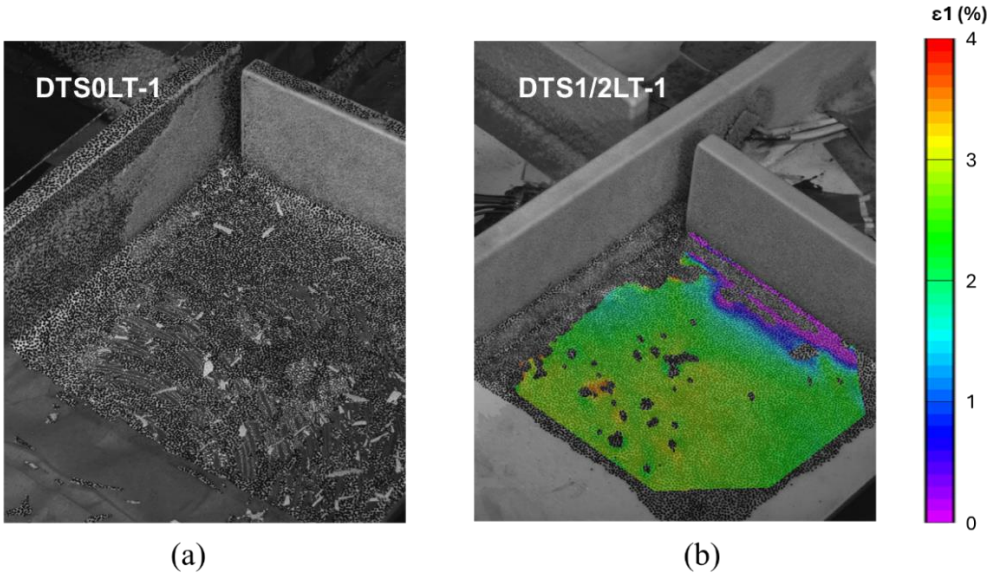

Source: FHWA.

Figure 59. Photograph. Strains at maximum load: DTS0LT-1 and DTS1/2LT-1.

6.3.2 DLS Detail

Eight discontinuous longitudinal stiffener specimens were tested:

- Two with no constraint-relief gap: DLS0LT-1 and DLS0LT-2;
- Two with a $^1/_4$-inch constraint-relief gap: DLS1/4LT-2 and DLS1/4RT-2;
- Two with a $^1/_2$-inch constraint-relief gap: DLS1/2LT-1 and DLS1/2LT-2; and

- Two with a 1-inch constraint-relief gap: DLS1LT-2 and DLS1RT-2.

The suite of DLS specimens allows for comparisons across four constraint relief gap sizes, low-temperature and room-temperature conditions, and two different heats of steel. Each of the DLS details tested are shown in Figure 60.

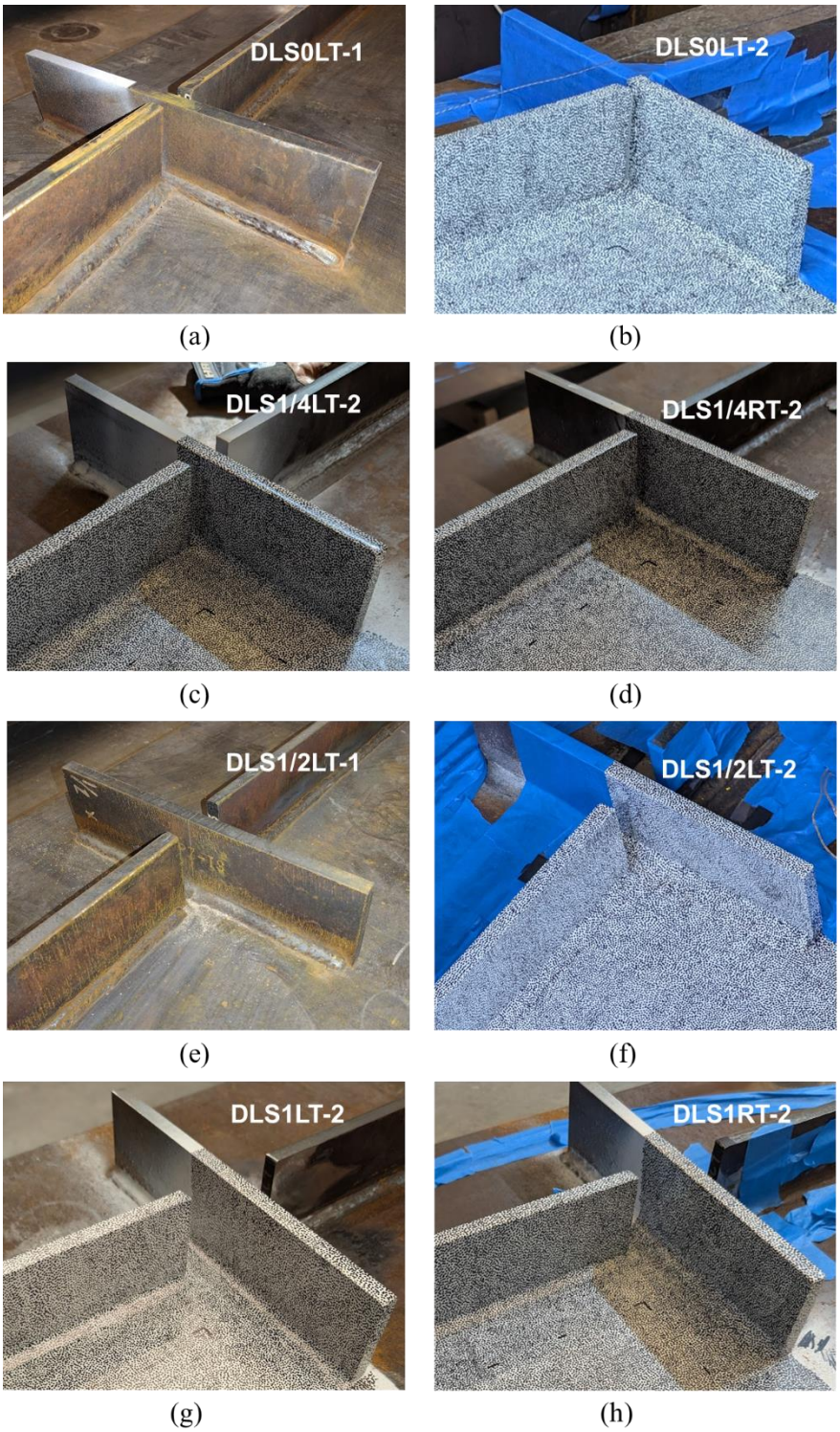

Source: FHWA.

Figure 60. Photograph. DLS specimens: (a) DLS0LT-1; (b) DLS0LT-2; (c) DLS1/4LT-2; (d) DLS1/4RT-2; (e) DLS1/2LT-1; (f) DLS1/2LT-2; (g) DLS1LT-2; (h) DLS1RT-2.

All the DLS specimens failed in brittle fracture regardless of CRG dimension, temperature condition, or steel heat. The load-deformation results are summarized in Figure 61, and a summary of the experimental results is provided in Table 6-2. Note that the load-displacement record for DLS1LT-1 does not appear due to a malfunction with the string potentiometer at about 200 kips of applied load.

Most of the brittle fractures propagated through the entire cross-section resulting in complete failure at the time of first fracture. However, three of the DLS specimens fabricated from the second (tougher) batch of steel experienced a pop-in fracture: DLS1/4LT-2, DLS1/4RT-2, and DLS1RT-2. In these specimens, maximum load is determined as the load at which the pop-in fracture occurred, taken as failure of the specimen. The specimens that experienced pop-in fractures were subsequently loaded until failure occurred through the entire cross-section. DLS1/4LT-2 experienced a brittle fracture through the remaining cross-section upon additional loading after the first fracture. Specimens DLS1/4RT-2 and DLS1RT-2 experienced ductile yielding after first fracture, until the remaining ligament was small, at which point the specimen ruptured. As is discussed further in Section 6.3.2.3, both DLS1/4RT-2 and DLS1RT-2 were found to have pre-existing cracks that corresponded with fracture initiation, based on inspection of the fracture surfaces.

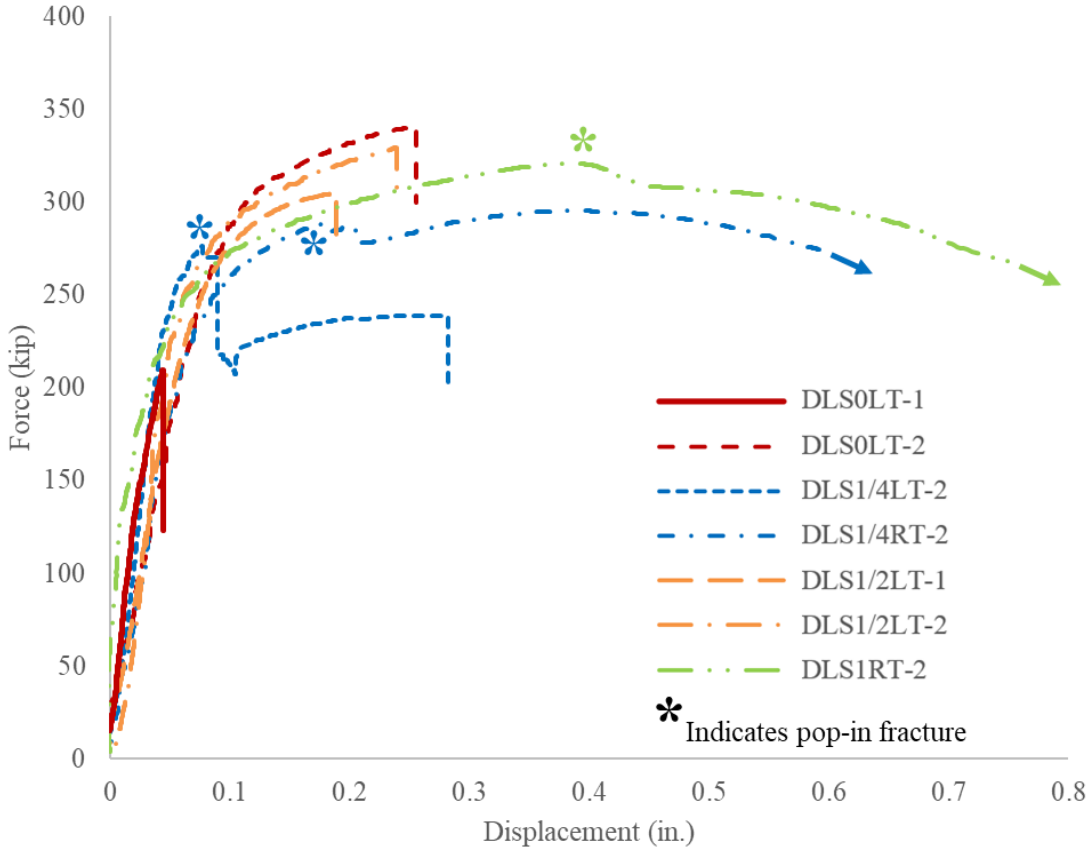

Source: FHWA.

Figure 61. Graph. Load-displacement records for DLS specimens.

A comparison of longitudinal strains from the Ro2 rosette strain gauge and the DIC at the same time and location (Table 6-2) shows a good match between the two data sources for strain measurements in the region of the detail of interest. The DIC measurements indicate a range of strains at failure varying from 0.160% (DLS0LT-1) up to 5.105% (DLS1LT-2) at the location of the Ro2 rosette. There was not a good correlation

between strain at failure and temperature condition, indicating that temperature is likely not a primary factor determining susceptibility to constraint-induced fracture, at least for the DLS detail.

Figure 62 presents the DIC strain fields for strain in the longitudinal direction, ε_1, for the eight DLS specimens at the time of maximum load. Note that for the specimens that experienced pop-in fractures, the DIC results shown are for the time snapshot immediately preceding the pop-in fracture. The results are ordered according to CRG dimension, from least to greatest. The DIC results show a localized strain hot spot occurring at the constraint relief gap in every specimen except for DLS0LT-1, which failed at such low strain that the hot spot is disguised by the consistent scale used for the results in this figure. There is a trend visible in the DIC results, in that the ε_1 hot spot generally increases in size with increasing constraint-relief gap dimension; however, the maximum strain magnitudes corresponding with fracture are remarkably similar across the specimens, ~4%.

The location of peak ε_1 corresponds with the location of fracture initiation in each of the specimens, which consistently occurred at the longitudinal stiffener weld termination.

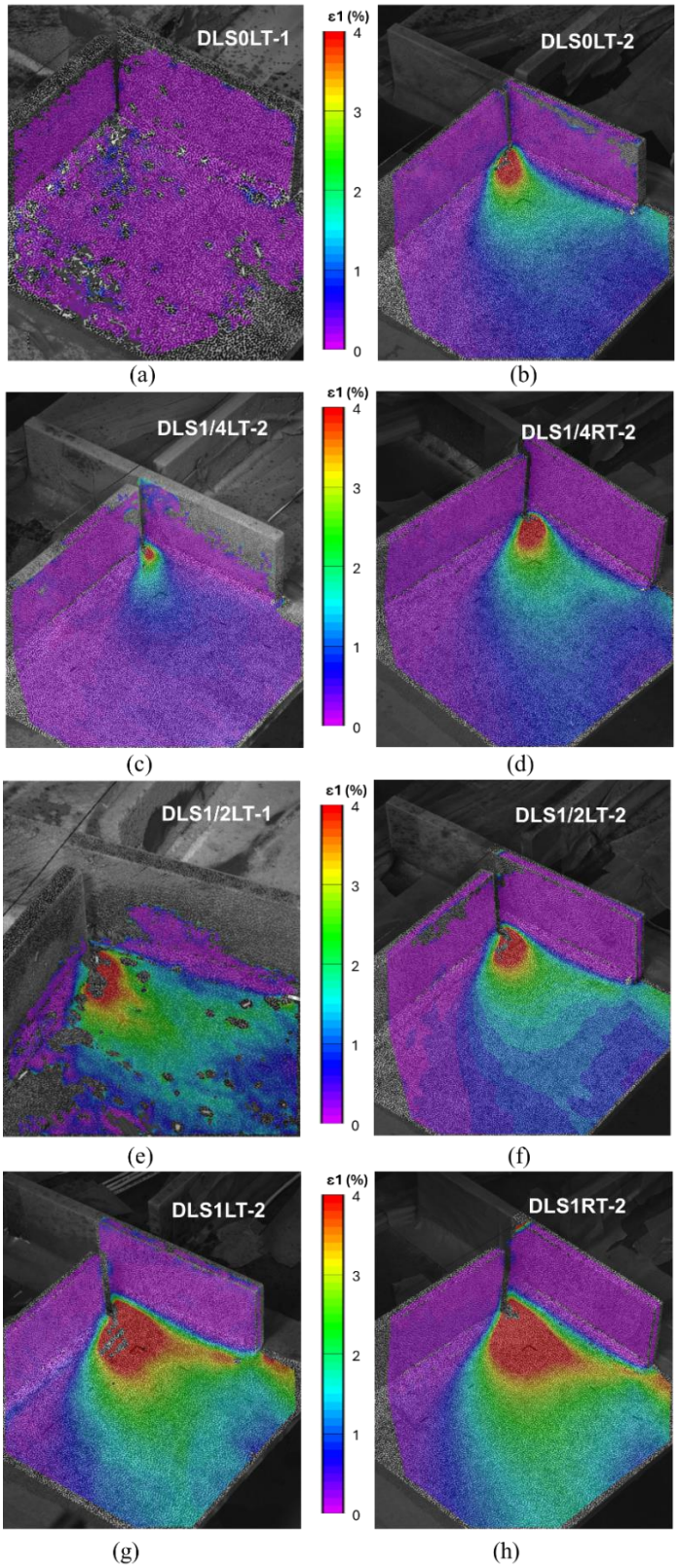

Source: FHWA.

Figure 62. Photograph. DIC results at maximum load for DLS specimens.

6.3.2.1 DLS Specimen Details

Although nominal specimen dimensions were specified, deviations with respect to weld termination locations and actual constraint relief gap were fabricated. To facilitate the description of as-built dimensions, locations within individual specimens have been determined based on the top or bottom of the primary plate, and quadrants divided by the longitudinal and transverse stiffeners. The longitudinal stiffeners divide quadrants I and IV from quadrants II and III, while transverse stiffeners divide quadrants I and II from III and IV. For consistency when examining fracture surface photographs below, the quadrants were determined with respect to the fracture location, such that the fracture always occurred on the quadrant III/IV side of the transverse stiffener. These designations are presented in Figure 63. The high contrast speckle pattern for DIC data acquisition was always applied to the top of the specimen. In all DLS specimens other than DLS0LT-2, the fracture occurred on the side of the transverse stiffener where DIC data was being captured, with the speckle pattern applied in quadrant IV. For specimen DLS0LT-2 the pattern was applied in quadrant II. Weld termination dimensions are schematically represented in Figure 64 and tabulated in Table 6-3.

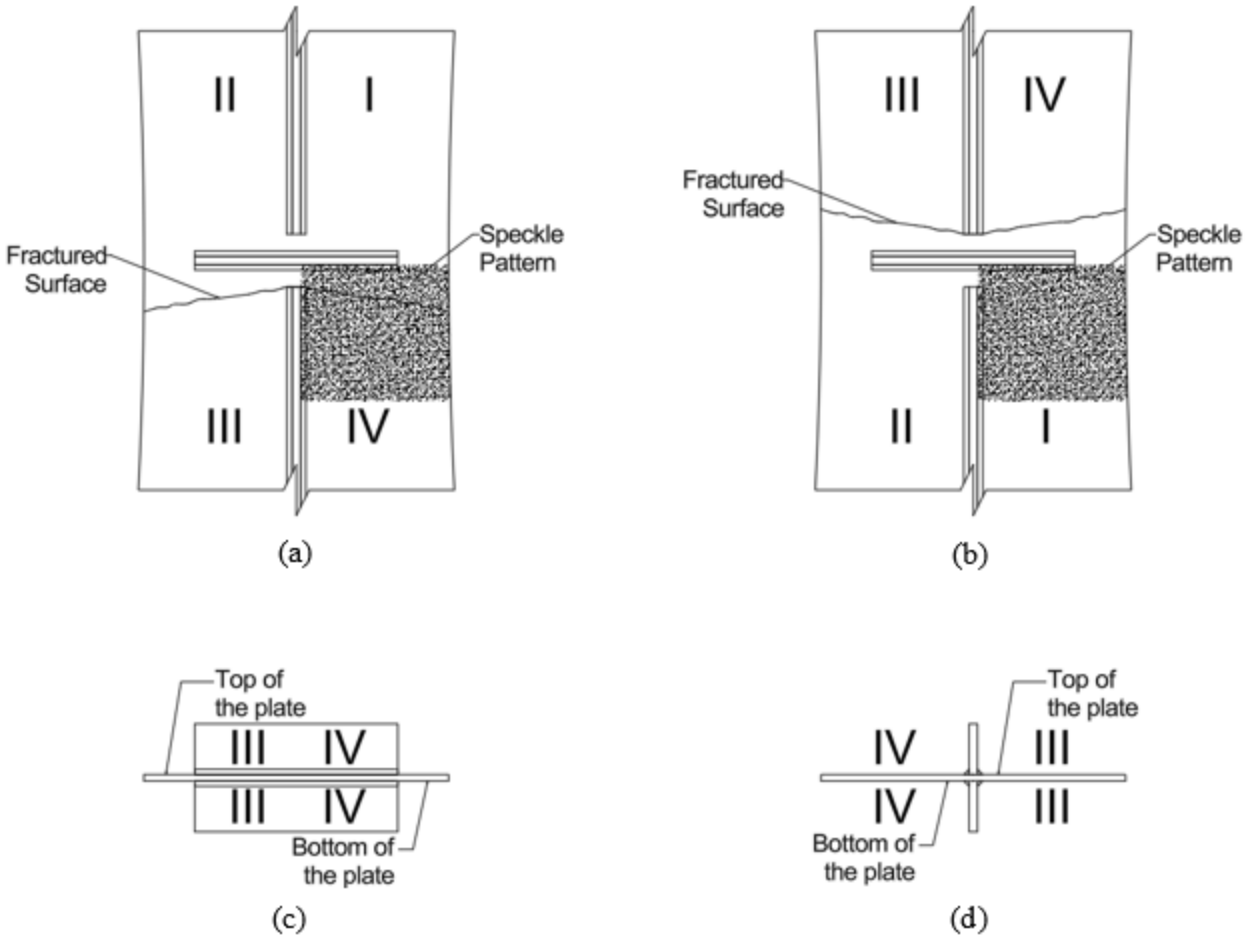

Figure 63. Illustration. Schematic representation of specimen quadrants from the top of the specimen for a) all specimens other than b) DLS0LT-2 and looking at the failure surfaces on the c) transverse-stiffener side and d) opposite fracture surface.

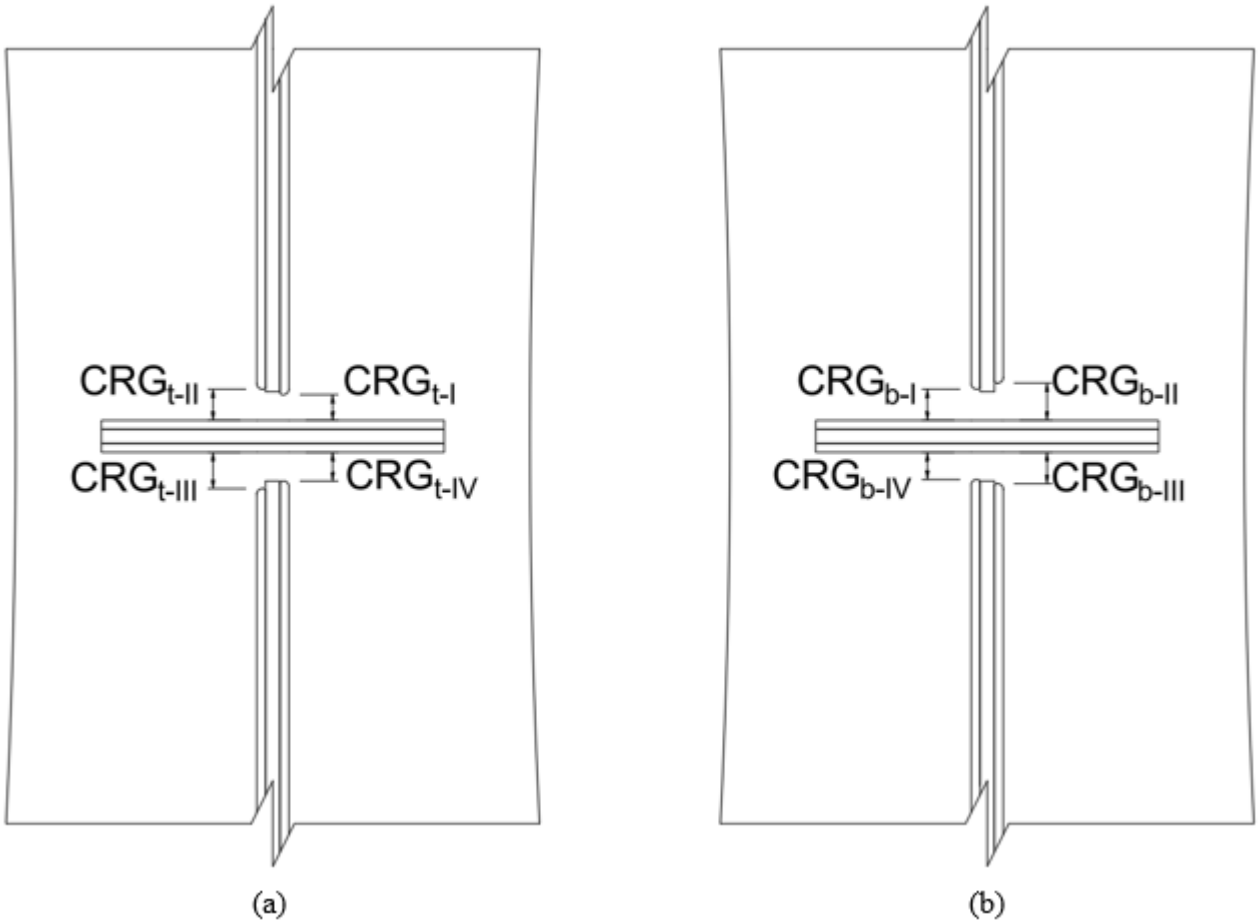

Figure 64. Illustration. Schematic representation of specimen weld termination dimensions from (a) top and (b) bottom surfaces of the specimens.

Table 6-3. Specimen weld termination dimensions.

Specimen	Nominal CRG (inch)	Top CRG_{t-I} (inch)	Top CRG_{t-II} (inch)	Top CRG_{t-III} (inch)	Top CRG_{t-IV} (inch)	Bottom CRG_{b-I} (inch)	Bottom CRG_{b-II} (inch)	Bottom CRG_{b-III} (inch)	Bottom CRG_{b-IV} (inch)
DLS0LT-1	0	0	0	0.155	0.242	0	0	0	0
DLS0LT-2*	0	0	0	0	0	0	0	0	0
DLS1/4LT-2	1/4	0.253	0.153	0	0.254	0.201	0.155	0.027	0.057
DLS1/4RT-2	1/4	0.240	0.236	0.132	0.091	0.152	0.092	0.107	0.160
DLS1/2LT-1	1/2	0.306	0.517	0.528	0.681	0.386	0.449	0.735	0.730
DLS1/2LT-2	1/2	0.423	0.498	0.449	0.230	0.475	0.451	0.477	0.508
DLS1LT-2	1	0.948	0.839	0.836	0.785	0.881	1.149	1.013	0.992
DLS1RT-2	1	1.004	1.034	1.275	1.120	0.690	0.645	1.104	1.402

* On DLS0LT-2, welds from the longitudinal stiffeners overlapped with the transverse stiffener welds.

6.3.2.2 Specimens DLS0LT-1 and DLS0LT-2

Images of the fractured DLS0 specimens, taken from the top, are shown in Figure 65 and Figure 66. Fracture surfaces for DLS0LT-1 and DLS0LT-2 are shown in Figure 67, Figure 68, Figure 70, Figure 71, and Figure 72. Specimens were cooled to -60 °F prior to loading, and fractures occurred at temperatures of -27 ºF and -23 ºF for DLS0LT-1 and DLS0LT-2, respectively. Failure loads for the two specimens were 209 kips and 341 kips, respectively.

These specimens were fabricated from different heats of steel but were otherwise nominally identical. Details of as-built dimensions for all DLS specimens are presented in Table 6-3. For DLS0LT-1, the longitudinal stiffeners were not well-aligned between the top and bottom surfaces of the specimen, and were offset approximately $^3/_8$ inch. For DLS0LT-1, initiation occurred at the termination of the longitudinal stiffener weld, coinciding with the toe of the transverse stiffener weld, on the bottom side of the specimen in Quadrant III, as indicated in Figure 67 and Figure 68. As noted in Table 6-3, the longitudinal stiffener welds overlapped the transverse stiffener welds on specimen DLS0LT-2. On this specimen fracture initiation occurred at the toe of the transverse stiffener weld, underneath the longitudinal weld. Initiation occurred on the bottom of the plate in Quadrant III, as noted in Figure 71 and Figure 72, and propagated through the longitudinal welds.

Figure 73 shows the output for T_1 and T_2 from a finite element model of specimen DLS0LT-1 constructed using the same meshing techniques and nonlinear materials used in the parametric study described in Chapter 4, loaded to its experimentally-observed fracture load of 209 kips. There are a couple of items of note: (1) the fracture path observed in the physical specimen closely follows the shape of the T_2 distribution at the detail; and (2) the point of maximum triaxiality in the model matches the point of fracture initiation at the termination of the longitudinal stiffener weld. The values denoted in the figure for T_1 and T_2 are maxima, and both occurred at the termination of the longitudinal stiffener weld.

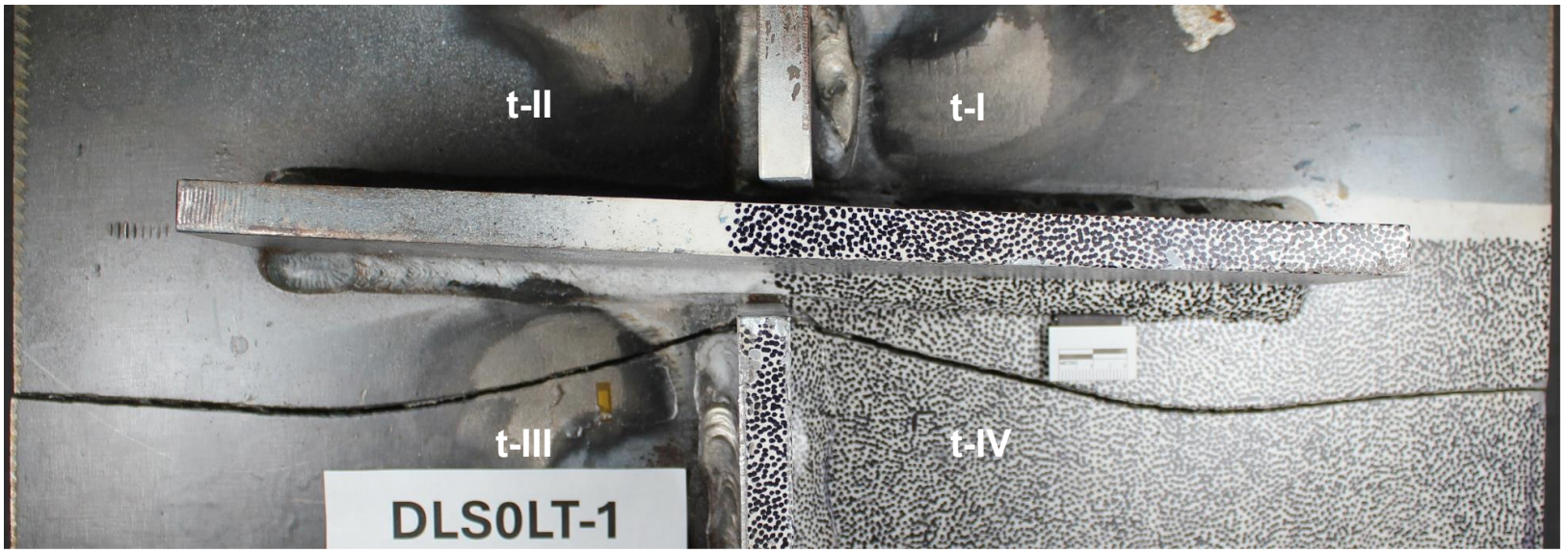

Source: FHWA.

Figure 65. Photograph. DLS0LT-1: top view of fractured specimen.

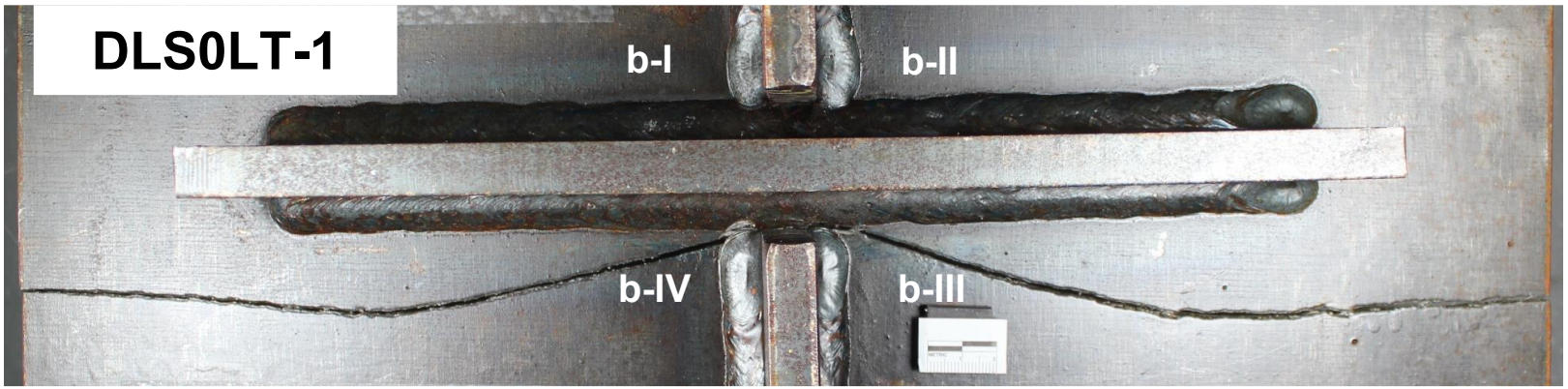

Source: FHWA.

Figure 66. Photograph. DLS0LT-1: bottom view of fractured specimen.

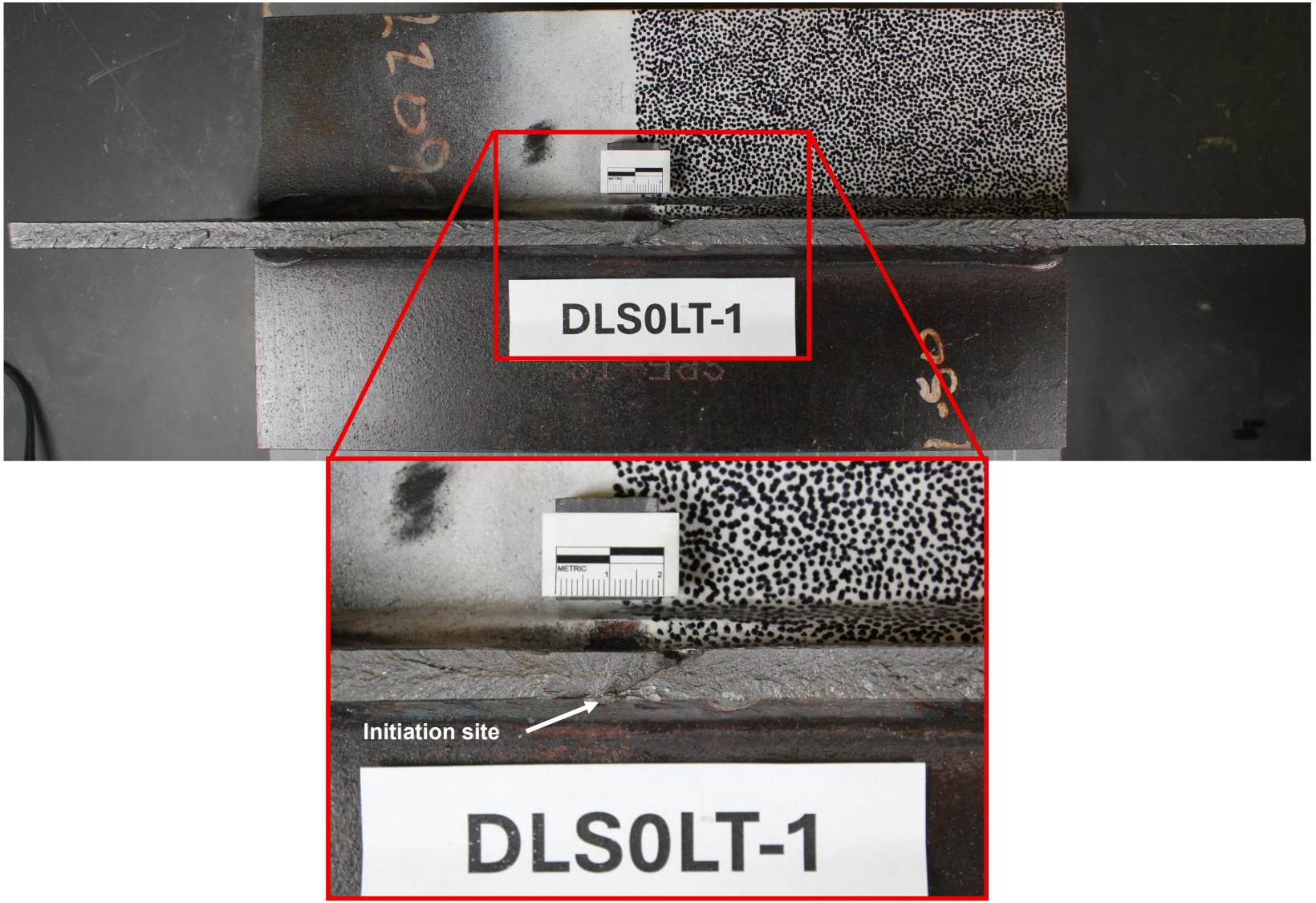

Source: FHWA.

Figure 67. Photograph. DLS0LT-1: transverse-stiffener side of fracture.

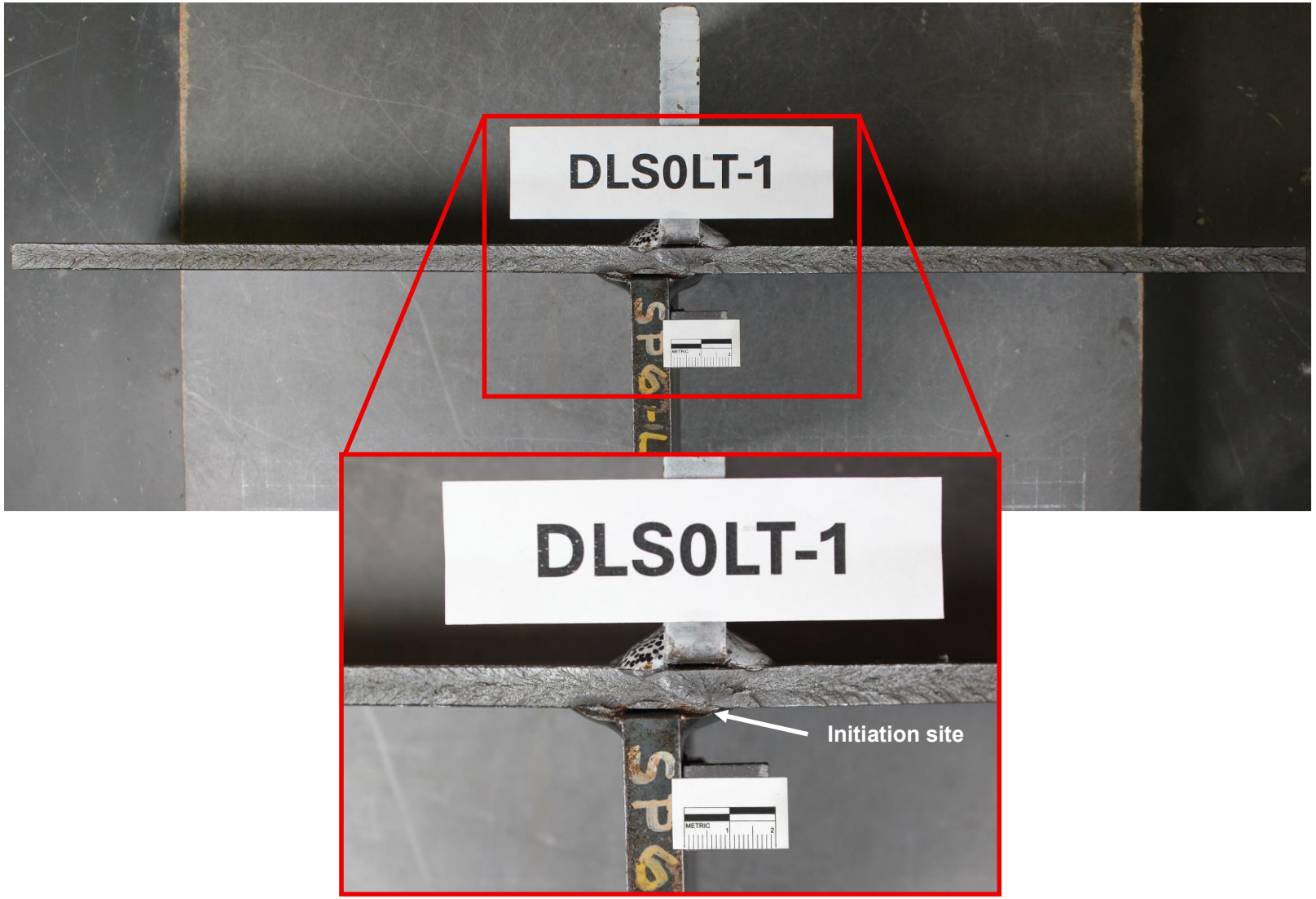

Source: FHWA.

Figure 68. Photograph. DLS0LT-1: opposite fracture face.

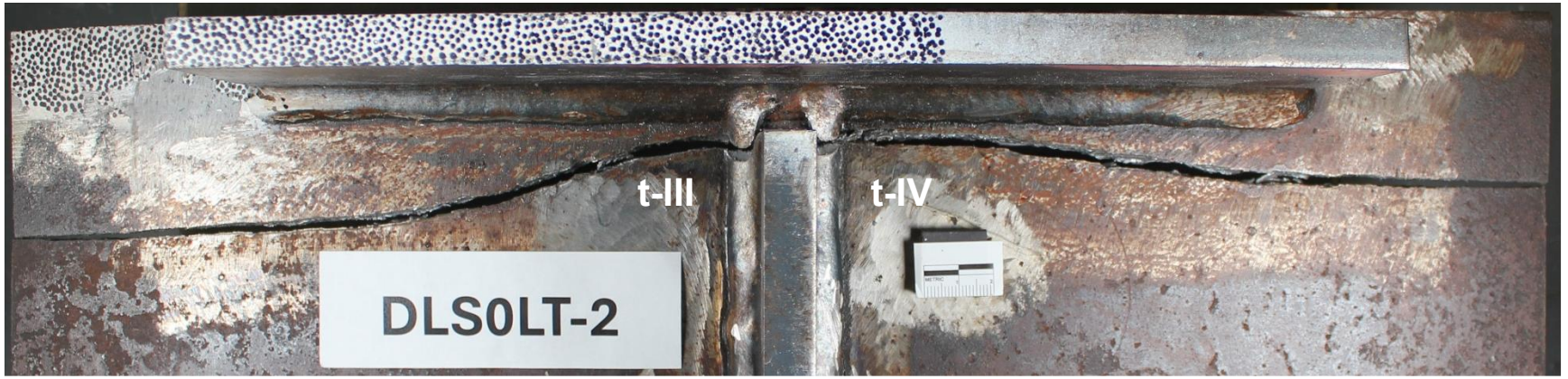

Source: FHWA.

Figure 69. Photograph. DLS0LT-2: top view of fractured specimen.

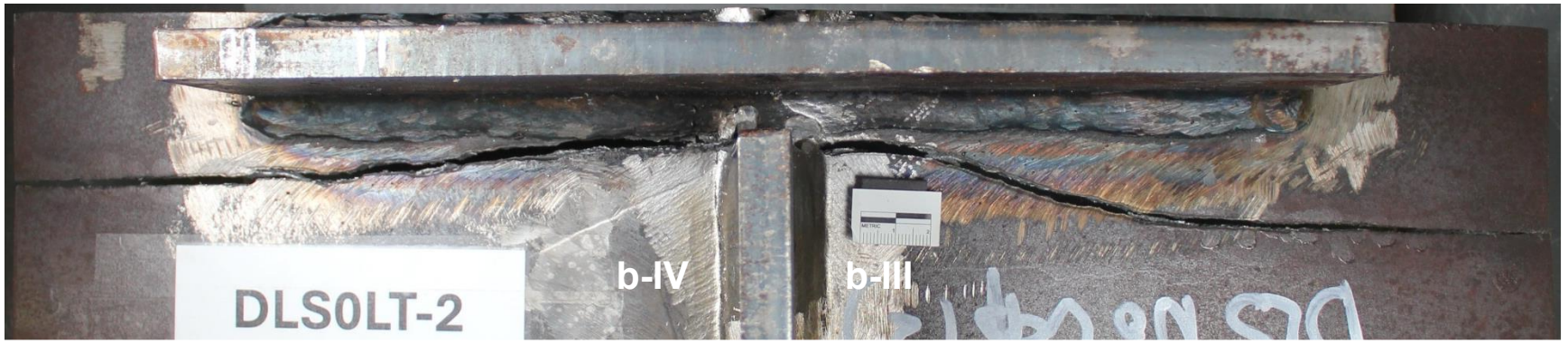

Source: FHWA.

Figure 70. Photograph. DLS0LT-2: bottom view of fractured specimen.

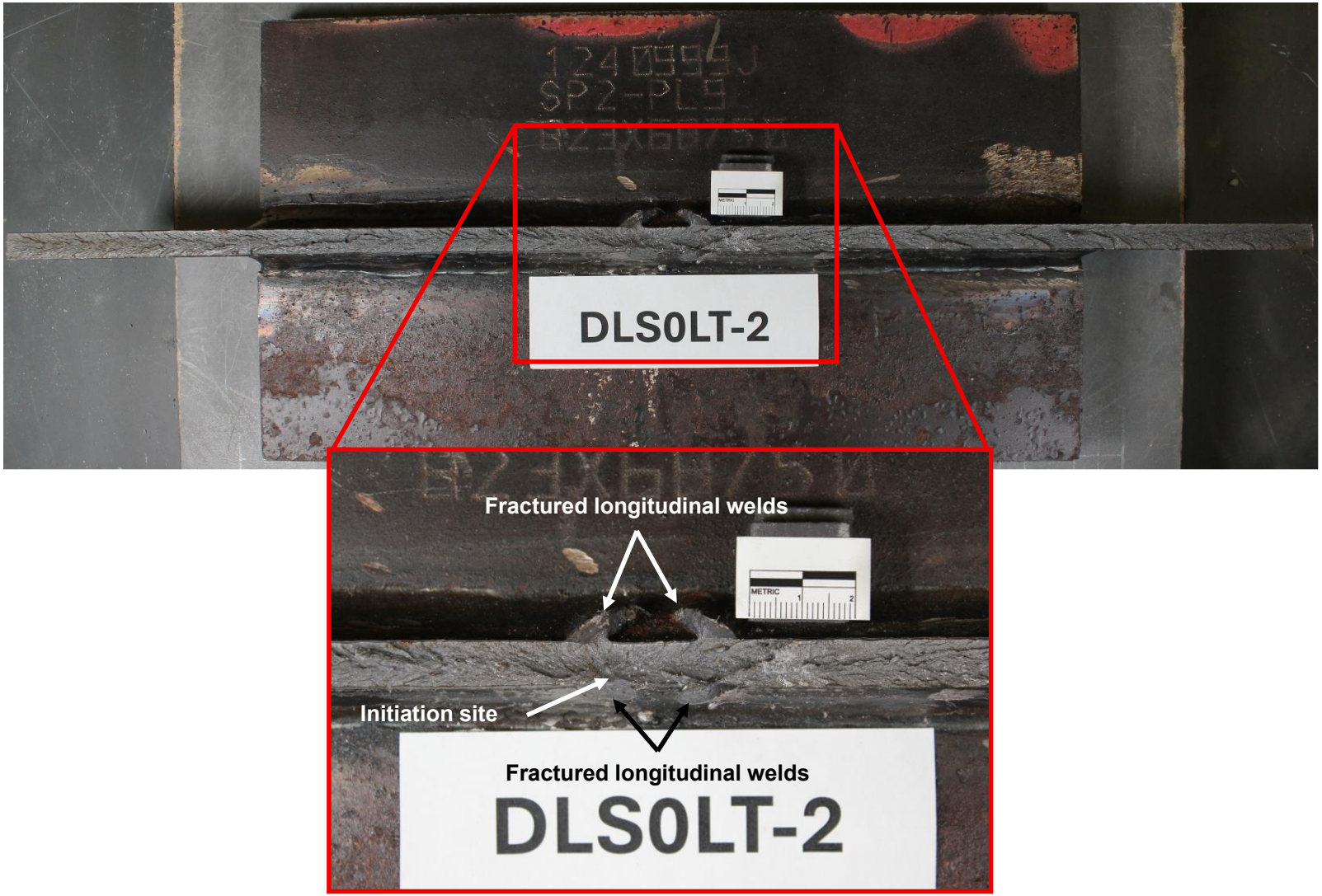

Source: FHWA.

Figure 71. Photograph. DLS0LT-2: transverse-stiffener side of fracture.

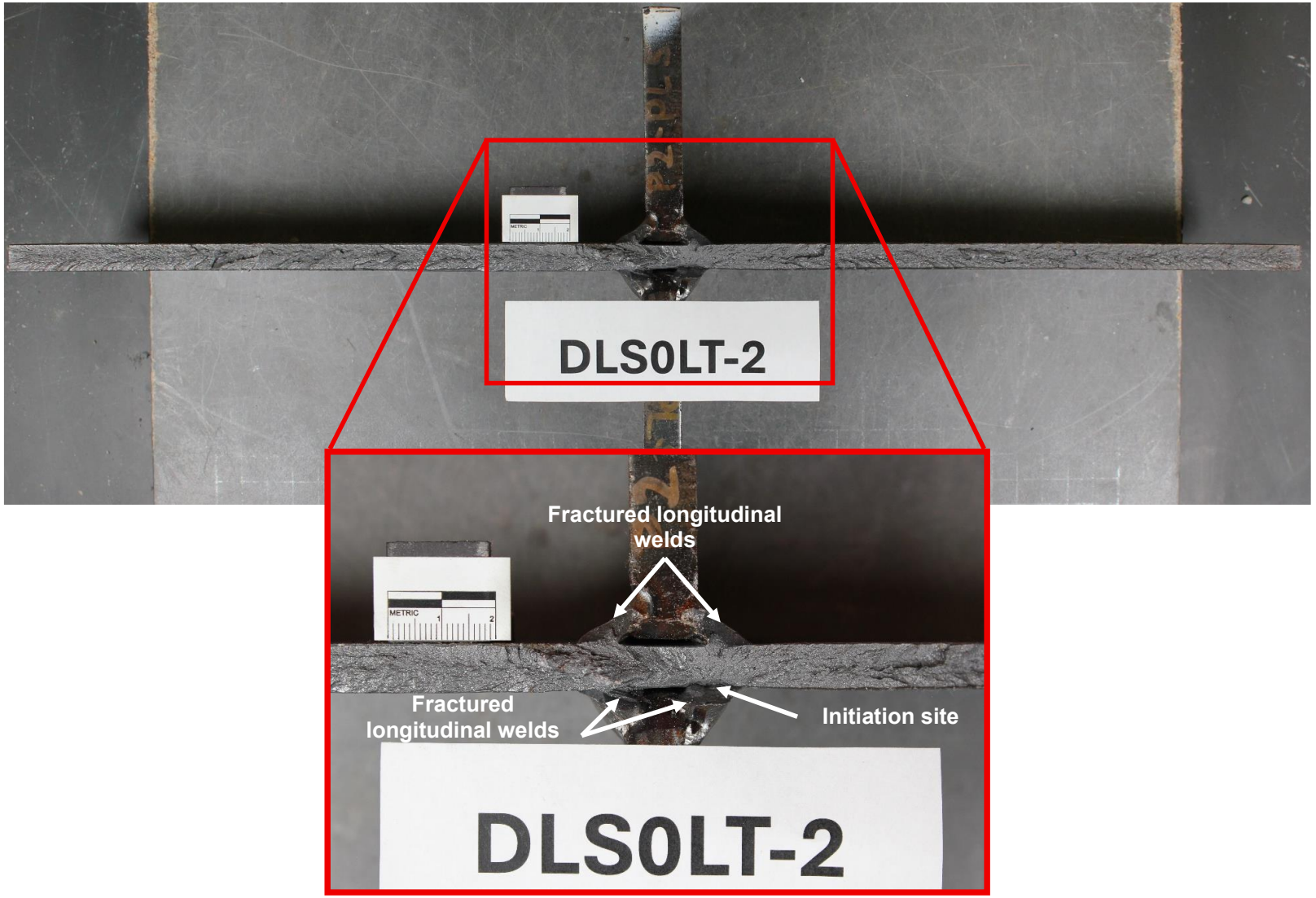

Source: FHWA.

Figure 72. Photograph. DLS0LT-2: opposite fracture face.

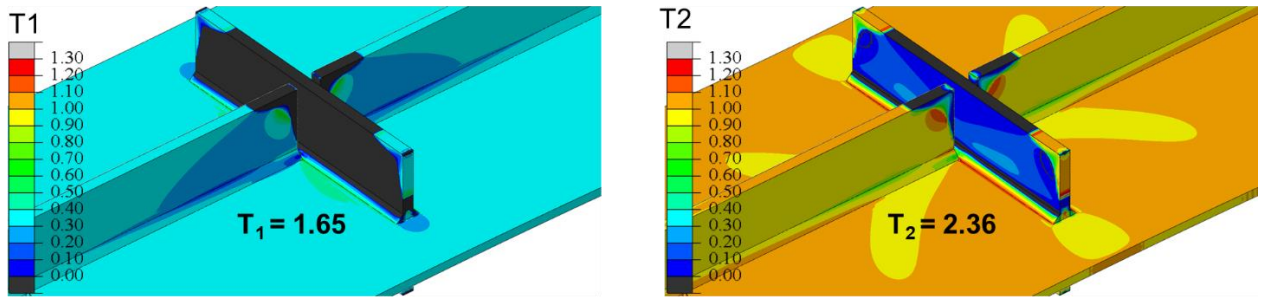

(a) (b)

Source: FHWA.

Figure 73. Illustration. FEA results for DLS0LT-1 subjected to fracture load $P_{fracture}$ = 209 kips.

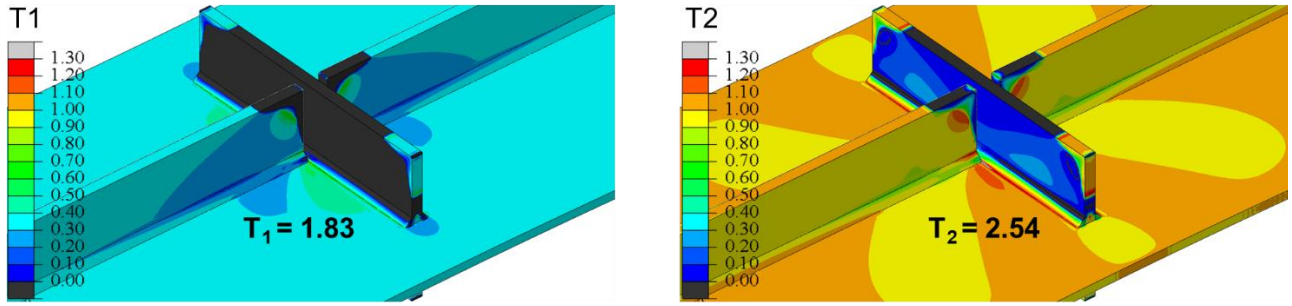

(a) (b)

Source: FHWA.

Figure 74. Illustration. FEA results for DLS0LT-2 subjected to fracture load $P_{fracture}$ = 341 kips.

6.3.2.3 Specimen DLS1/4LT-2 and DLS1/4RT-2

DLS1/4LT-2 and DLS1/4RT-2 were both fabricated from the same heat of steel (Batch 2) but were tested at different temperatures. DLS1/4LT-2 was soaked at -60 °F before testing and was at a temperature of -52 °F when fracture occurred. DLS1/4RT-2 was tested at room temperature and was at a temperature of 71 °F at time of fracture. Nonetheless, the two specimens fractured at very similar load levels: 277 kips for DLS1/4LT-2 and 287 kips for DLS1/4RT-2. In both cases, the initial fractures were pop-in, meaning the fractures self-arrested in the web material and loading was continued before complete cross-section separation was achieved. Top views of the DLS1/4LT-2 and DLS1/4RT-2 specimens are presented in Figure 76 and Figure 80. Arrest locations of all pop-in fractures are identified in Figure 78 and Figure 79 for DLS1/4LT-2 and in Figure 82 and Figure 83 for DLS1/4RT-2.

Both specimens were specified to have $^1/_4$-inch gaps between the longitudinal weld termination and the toe of the transverse stiffener weld. However, the as-fabricated dimensions showed significant variability as Table 6-3, the longitudinal stiffener weld termination on one side of the transverse stiffener coincided with the toe of the transverse stiffener weld, shown in Figure 75. For the DLS1/4LT-2 specimen, the gap in quadrant III was fabricated at 0 inches on the top surface, meaning the weld terminations were touching. The other measured gaps for this specimen varied from 0.027 inches to 0.254 inches. For the DLS1/4RT-2 specimen, the measured gaps ranged from 0.091 inches to 0.240 inches across both surfaces. Unfortunately, fractures for both DLS1/4LT-2 and DLS1/4RT-2 initiated from pre-existing flaws rather than from the CRG details. The flaws are identified in in Figure 78 and Figure 79 for DLS1/4LT-2 and in Figure 82 and Figure 83 for DLS1/4RT-2. It is unclear how these flaws originated, as the specimens were only tested monotonically with no applied cyclic loading. Existence of these flaws makes the interpretation of DLS1/4 specimen results difficult.

Figure 84 and Figure 85 show the output for T_1 and T_2 from finite element models of specimens DLS1/4LT-2 and DLS1/4RT-2, respectively. The models were constructed using the same meshing techniques and nonlinear materials used in the parametric study described in Chapter 4, and they were loaded to experimentally-observed fracture loads of 277 kips and 287 kips, respectively. The values denoted in the figures for T_1 and T_2 are maxima, and both occurred at the termination of the longitudinal stiffener weld.

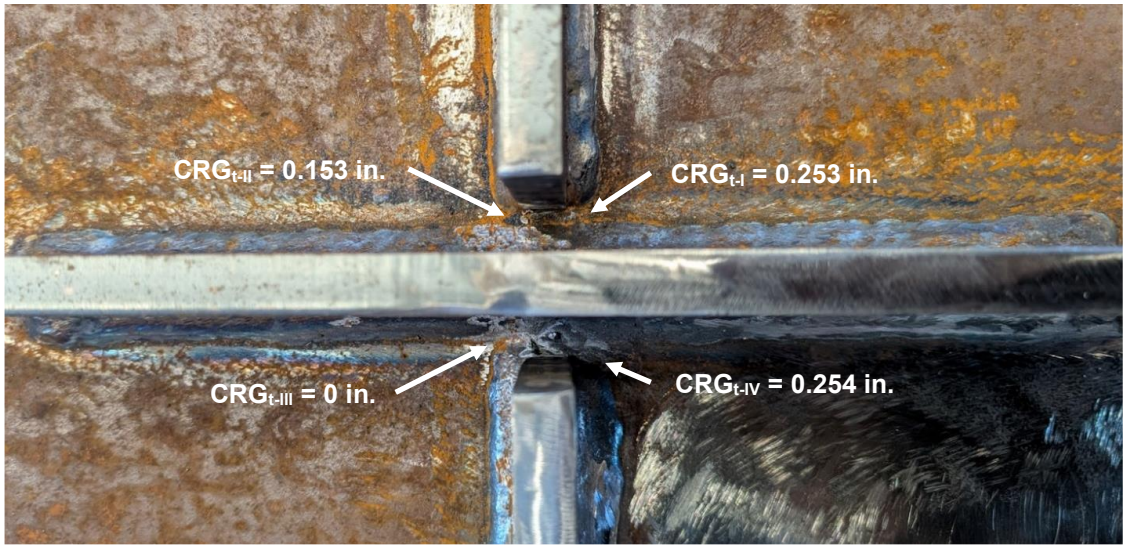

Source: FHWA.

Figure 75. Photograph. View of DLS1/4LT-2.

Source: FHWA.

Figure 76. Photograph. DLS1/4LT-2: top view of fractured specimen.

Source: FHWA.

Figure 77. Photograph. DLS1/4LT-2: bottom view of fractured specimen.

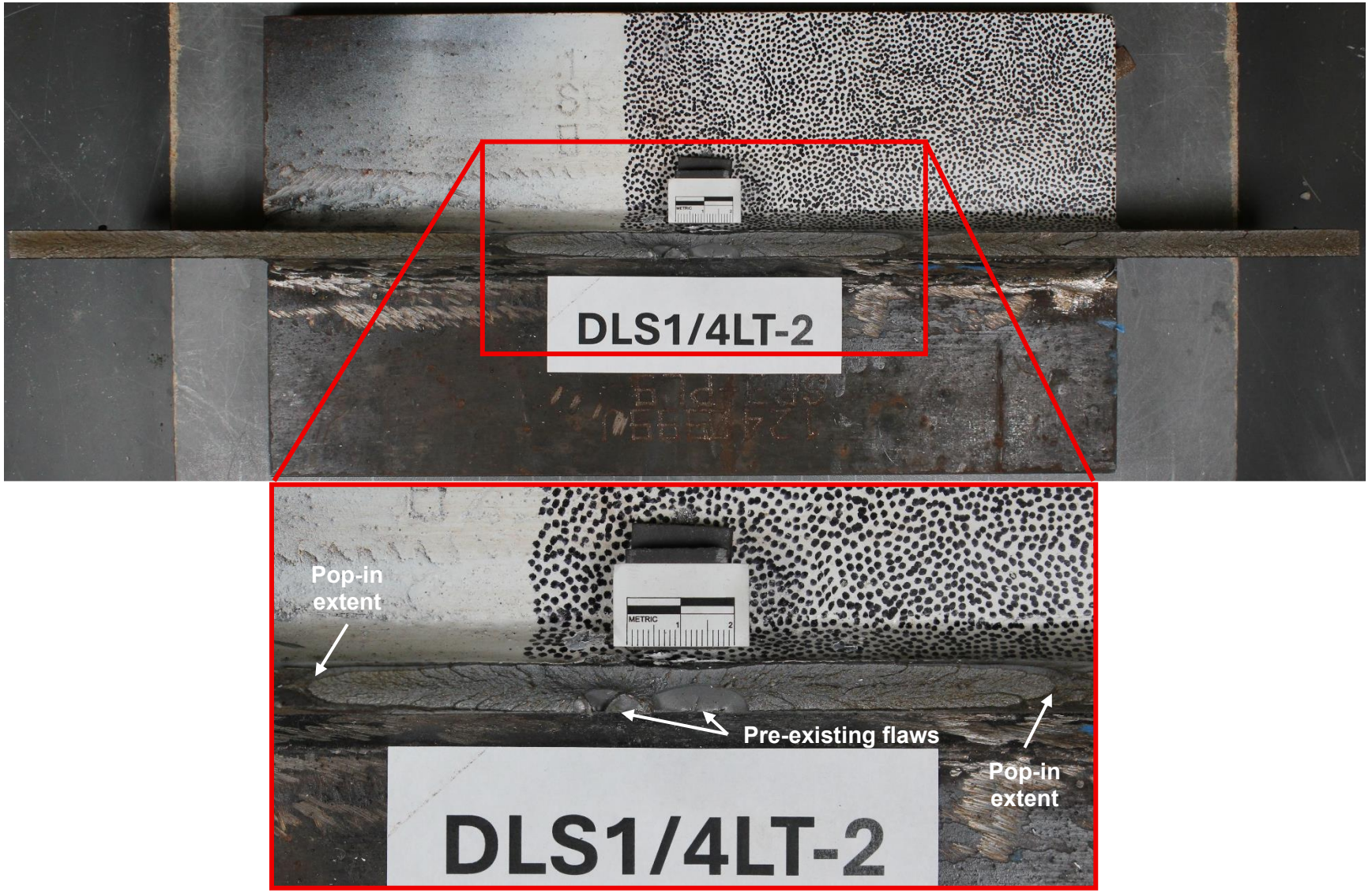

Source: FHWA.

Figure 78. Photograph. DLS1/4LT-2: transverse-stiffener side of fracture.

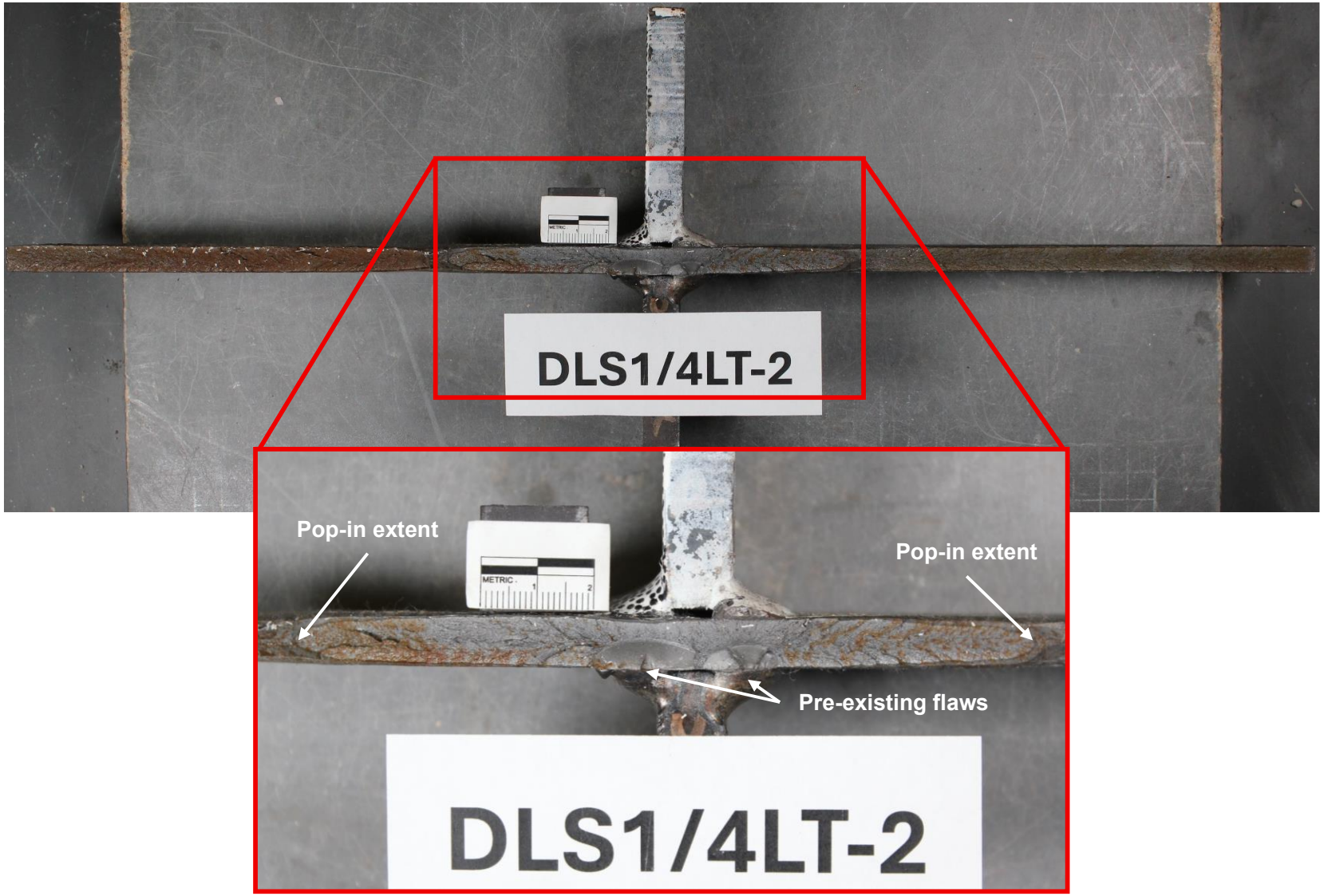

Source: FHWA.

Figure 79. Photograph. DLS1/4LT-2: opposite fracture face.

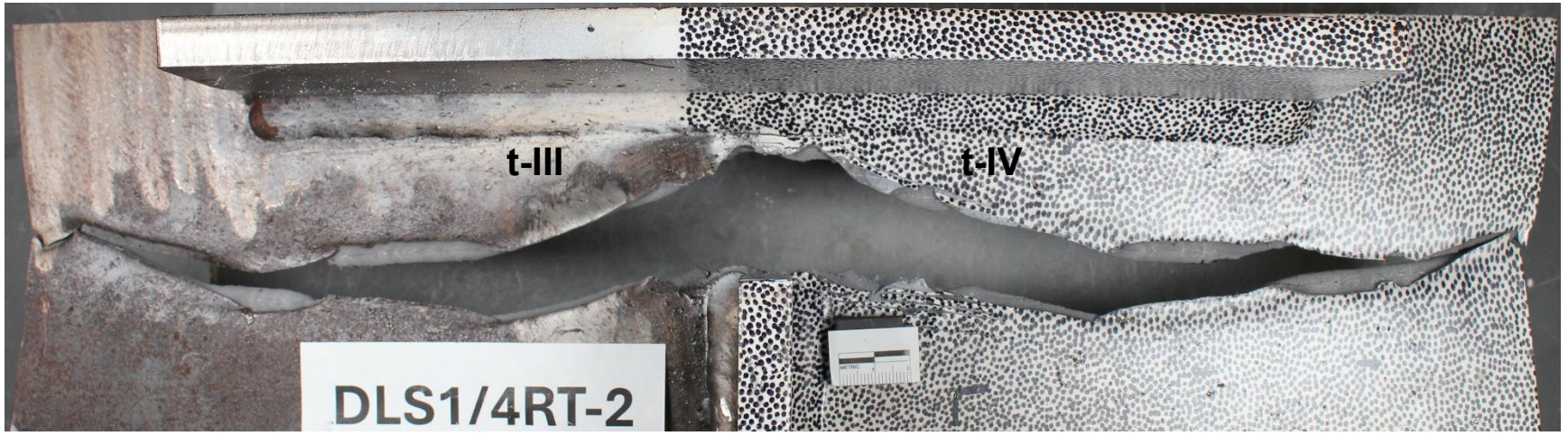

Source: FHWA.

Figure 80. Photograph. DLS1/4RT-2: top view of fractured specimen.

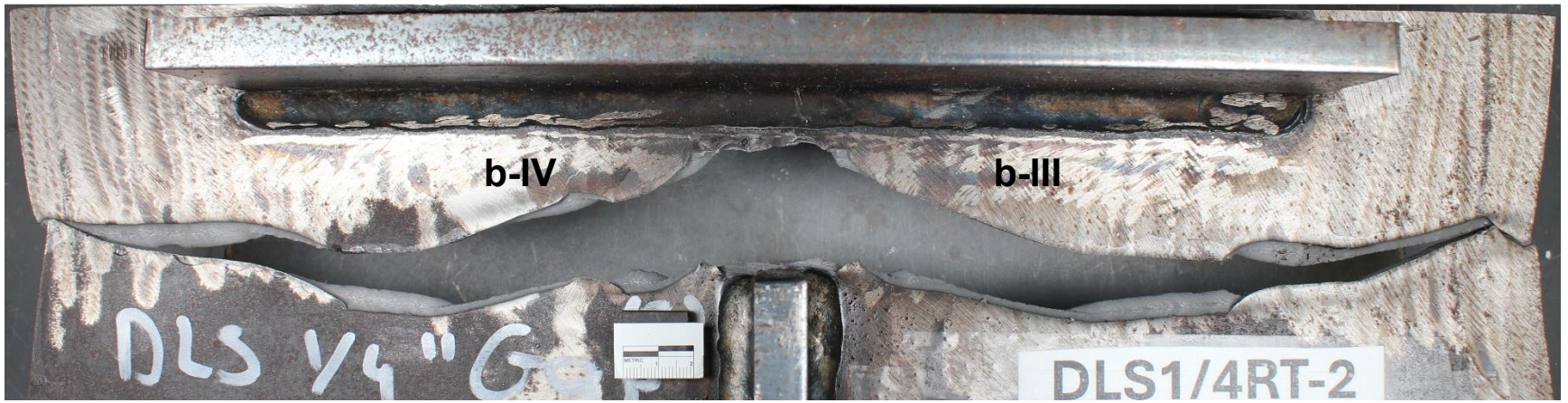

Source: FHWA.

Figure 81. Photograph. DLS1/4RT-2: top view of fractured specimen.

Source: FHWA.

Figure 82. Photograph. DLS1/4RT-2: transverse-stiffener side of fracture.

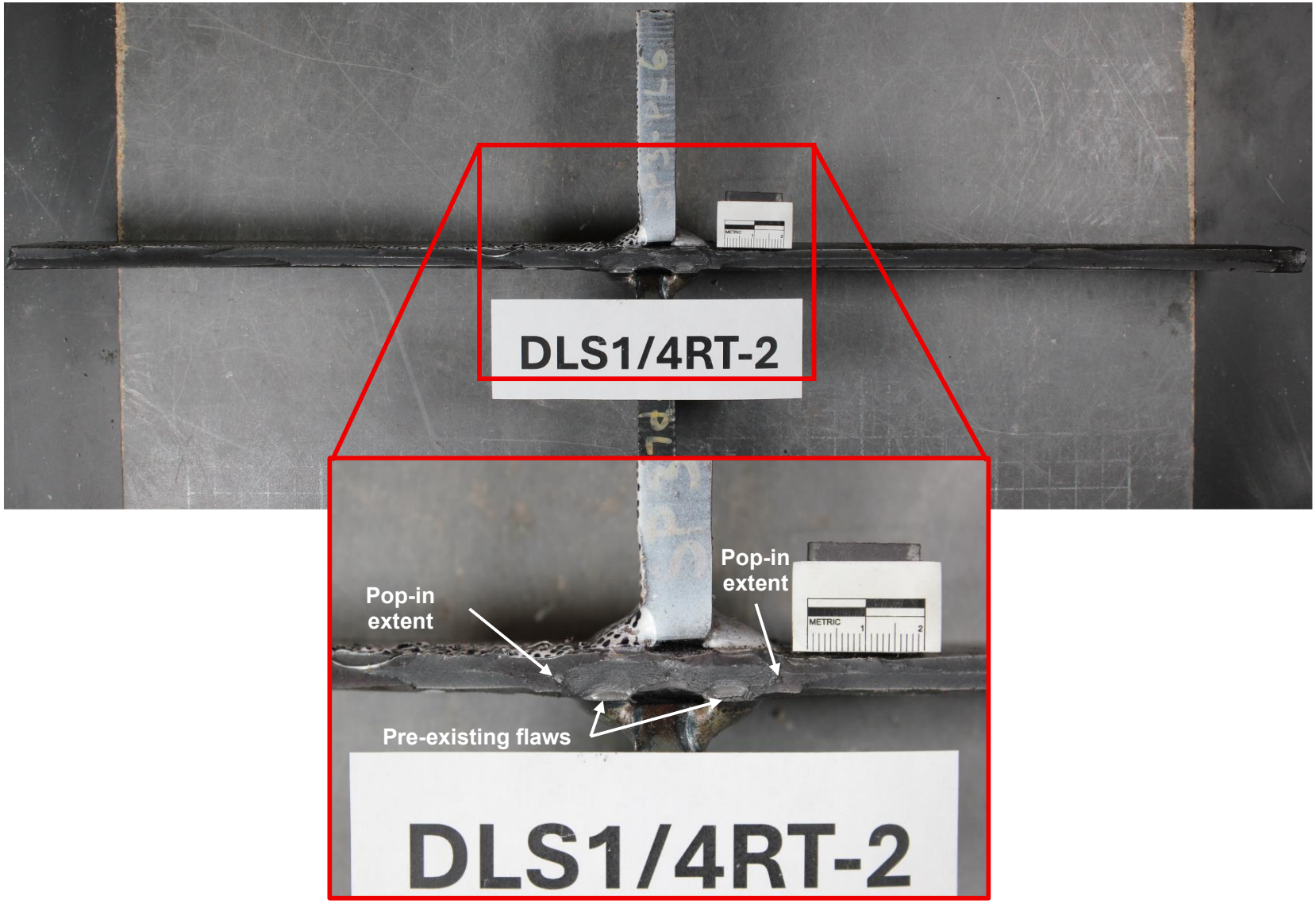

Source: FHWA.

Figure 83. Photograph. DLS1/4RT-2: opposite fracture face.

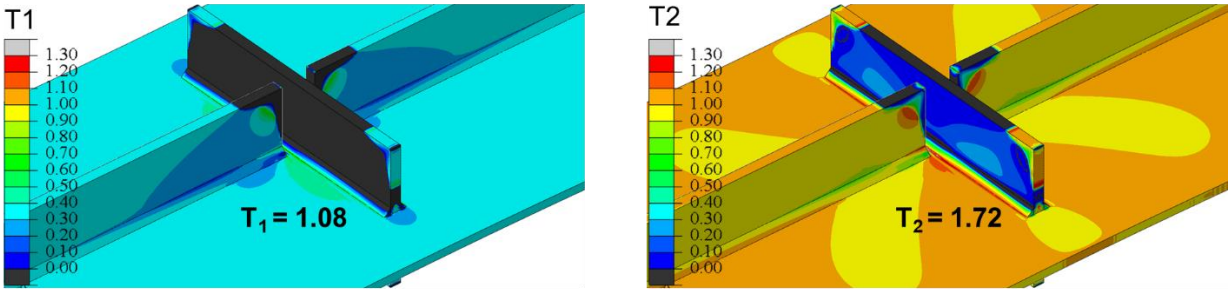

(a) (b)

Source: FHWA.

Figure 84. Illustration. FEA results for DLS1/4LT-2 subjected to fracture load $P_{fracture}$ = 277 kips.

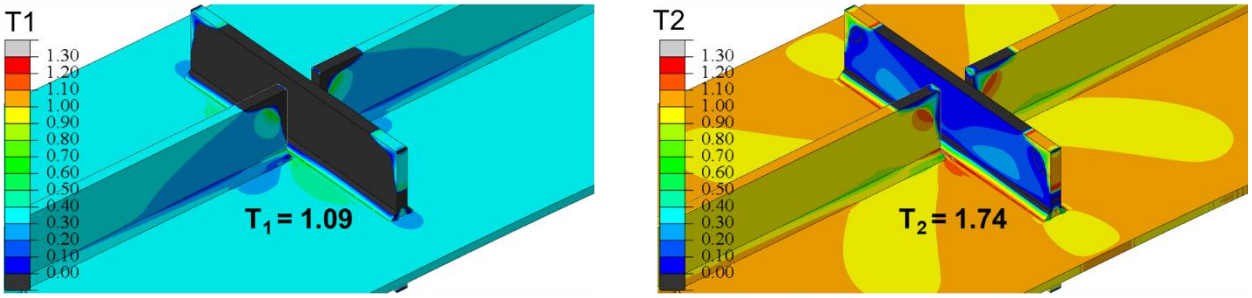

(a) (b)

Source: FHWA.

Figure 85. Illustration. FEA results for DLS1/4RT-2 subjected to fracture load $P_{fracture}$ = 287 kips.

6.3.2.4 Specimen DLS1/2LT-1 and DLS1/2LT-2

DLS1/2LT-1 and DLS1/2LT-2 were both tested at low temperature (soaked at -60 °F and were at temperatures of -10 °F and -32 °F, respectively, at times of failure). Failure loads for DLS1/2LT-1 and DLS1/2LT-2 were 305 kips and 330 kips, respectively. Fabricated to the same nominal dimensions, the specimen materials originated from different heats of steel.

Broken specimen photographs of each specimen, taken from the top, are shown in Figure 86 and Figure 90. In both cases, the initial fractures initiated at the termination of the longitudinal stiffener welds and propagated completely through the gross section of the specimen. For DLS1/2LT-1 fracture initiated at the termination of the longitudinal weld on the top of the primary plate in quadrant III. This can be seen in Figure 88 and Figure 89. The as-built CRG at this initiation location was 0.528 inches (Table 6-3). For DLS1/2LT-2, the fracture also initiated from the top of the plate, but from the longitudinal weld termination in quadrant IV, as shown in Figure 92 and Figure 93, where the as-built distance between welds was 0.230 inches.

Figure 94 and Figure 95 show the output for T_1 and T_2 from finite element models of specimens DLS1/2LT-1 and DLS1/2LT-2, respectively. The models were constructed using the same meshing techniques and nonlinear materials used in the parametric study described in Chapter 4, and they were loaded to experimentally-observed fracture loads of 305 kips and 330 kips, respectively. The values denoted in the figures for T_1 and T_2 are maxima, and both occurred at the termination of the longitudinal stiffener weld.

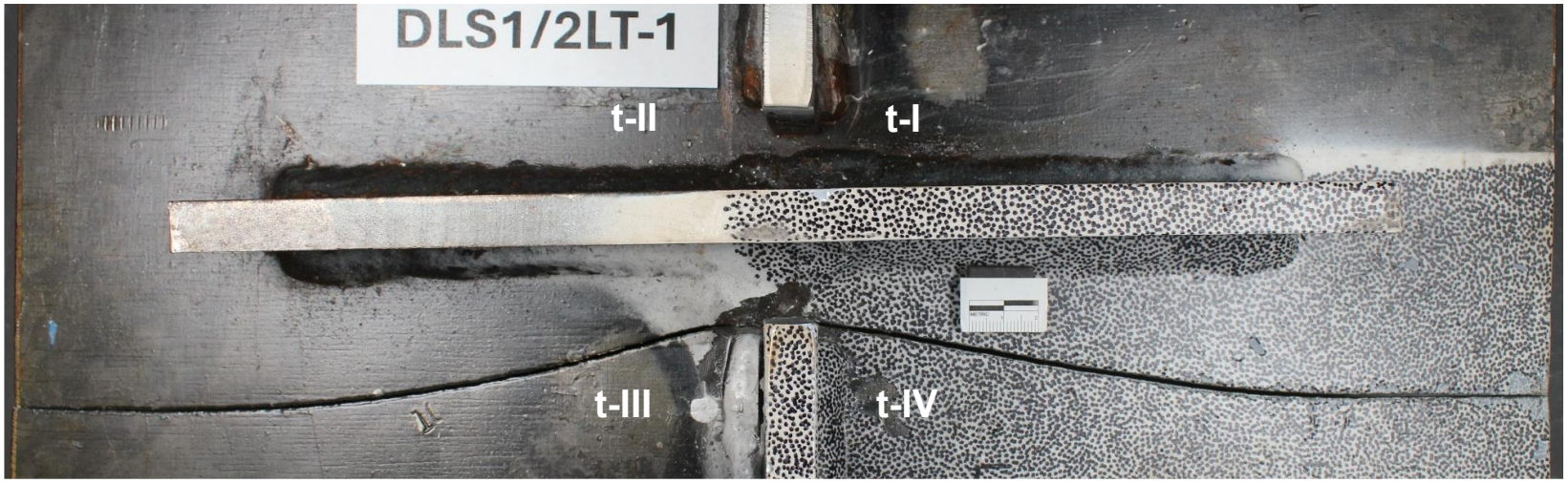

Source: FHWA

Figure 86. Photograph. DLS1/2LT-1: top view of fractured specimen.

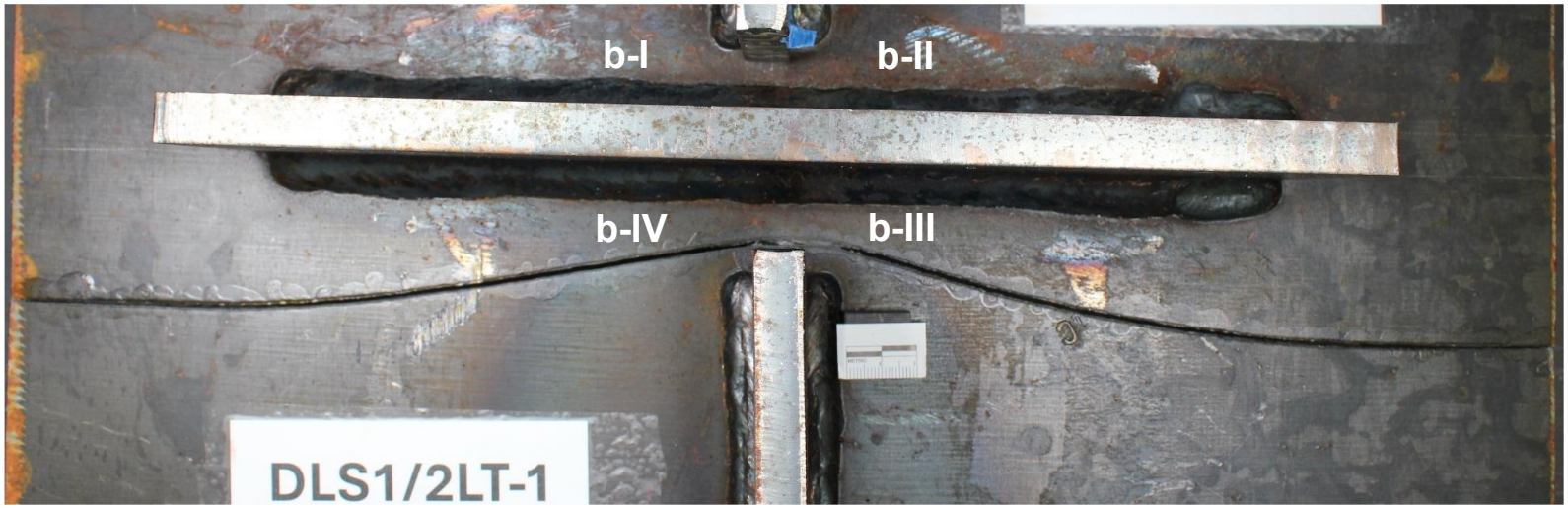

Source: FHWA

Figure 87. Photograph. DLS1/2LT-1: bottom view of fractured specimen.

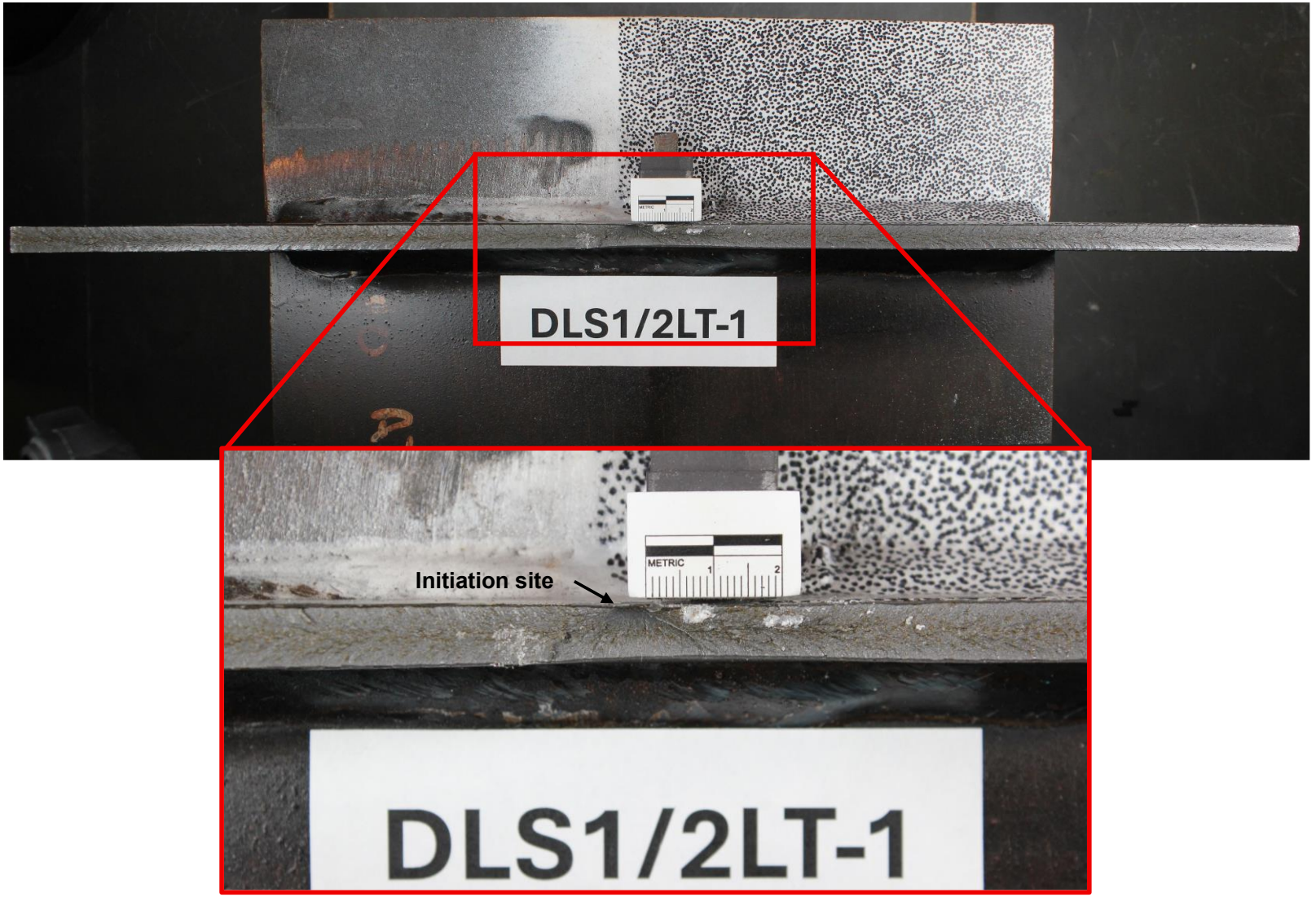

Source: FHWA

Figure 88. Photograph. DLS1/2LT-1: transverse-stiffener side of fracture.

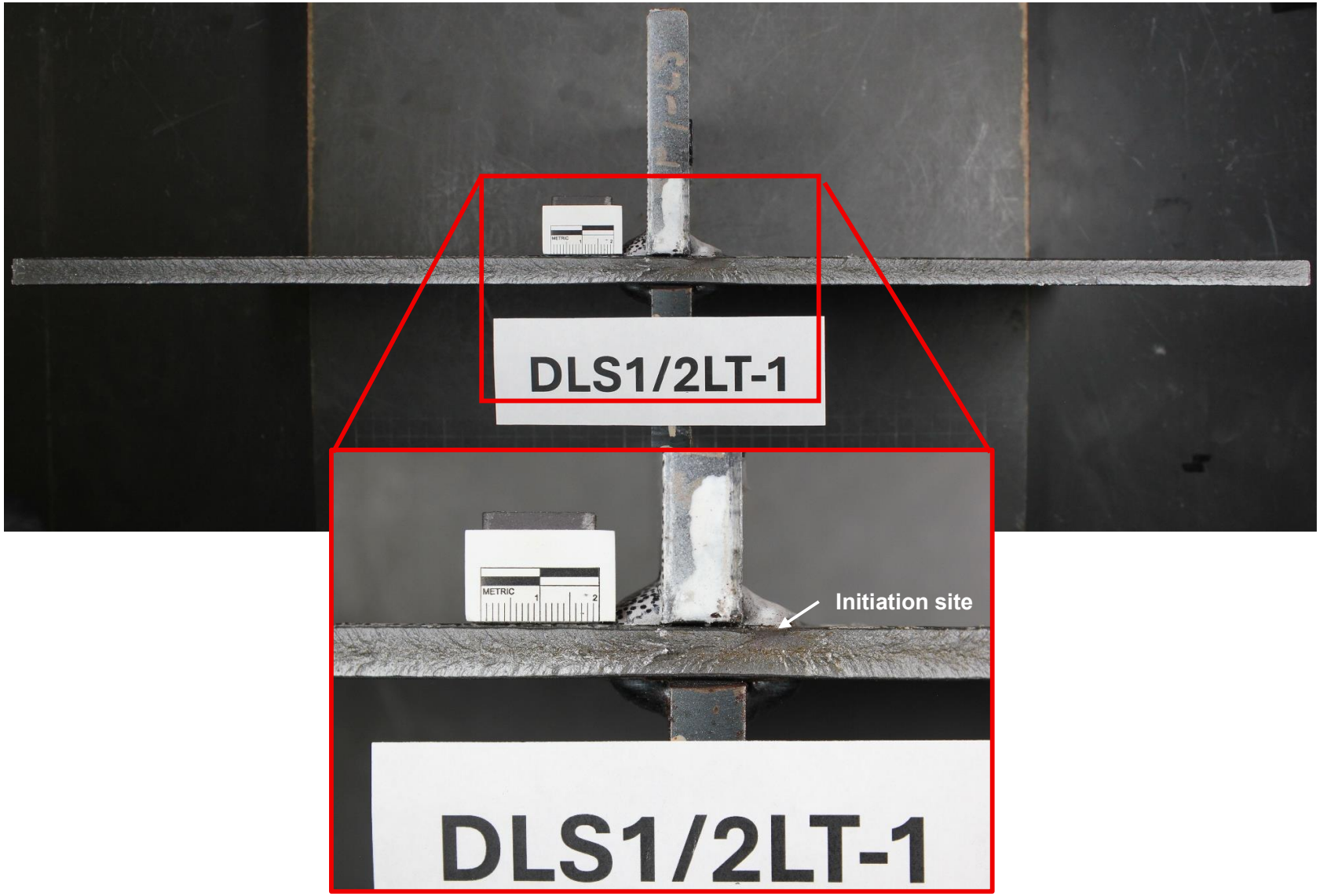

Source : FHWA

Figure 89. Photograph. DLS1/2LT-1: opposite fracture face.

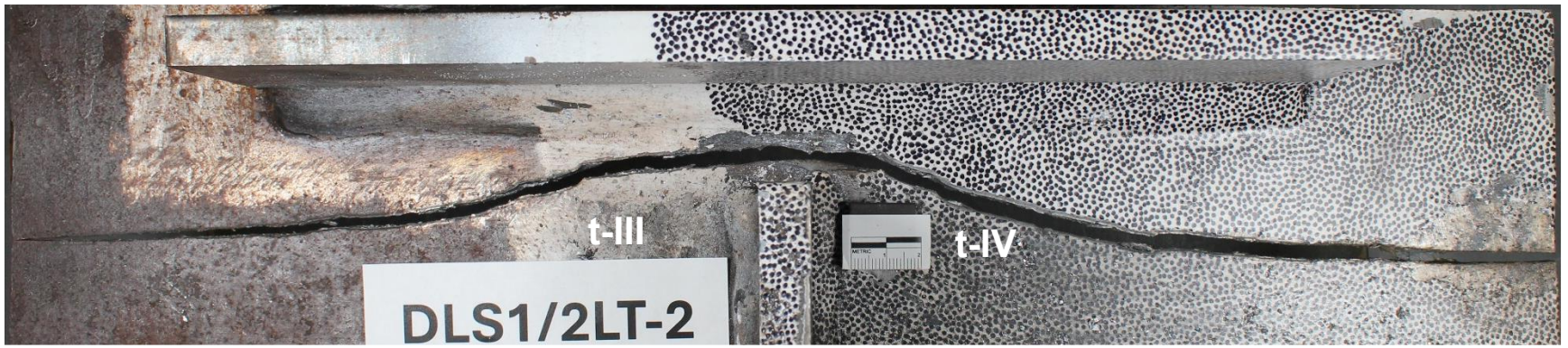

Source: FHWA

Figure 90. Photograph. DLS1/2LT-2: top view of fractured specimen.

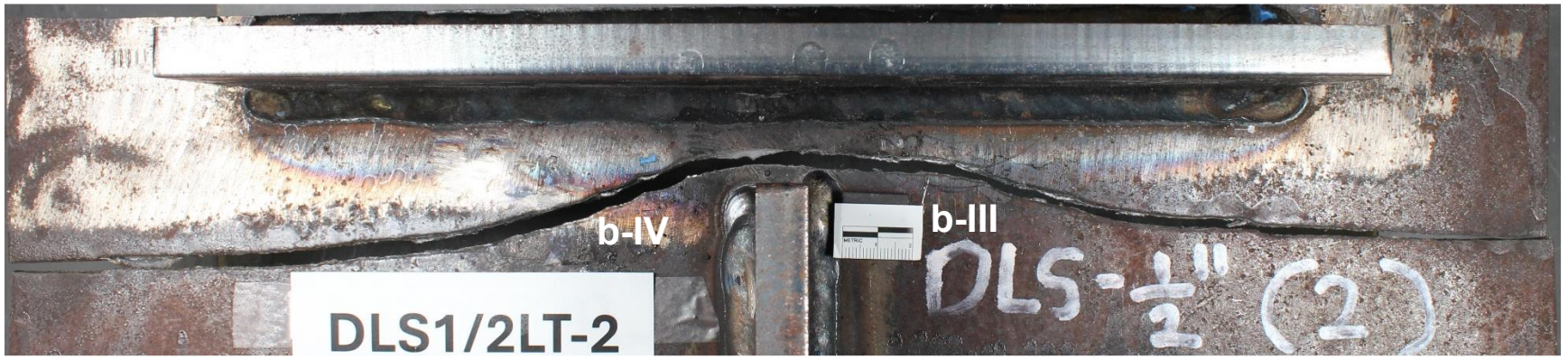

Source: FHWA

Figure 91. Photograph. DLS1/2LT-2: bottom view of fractured specimen.

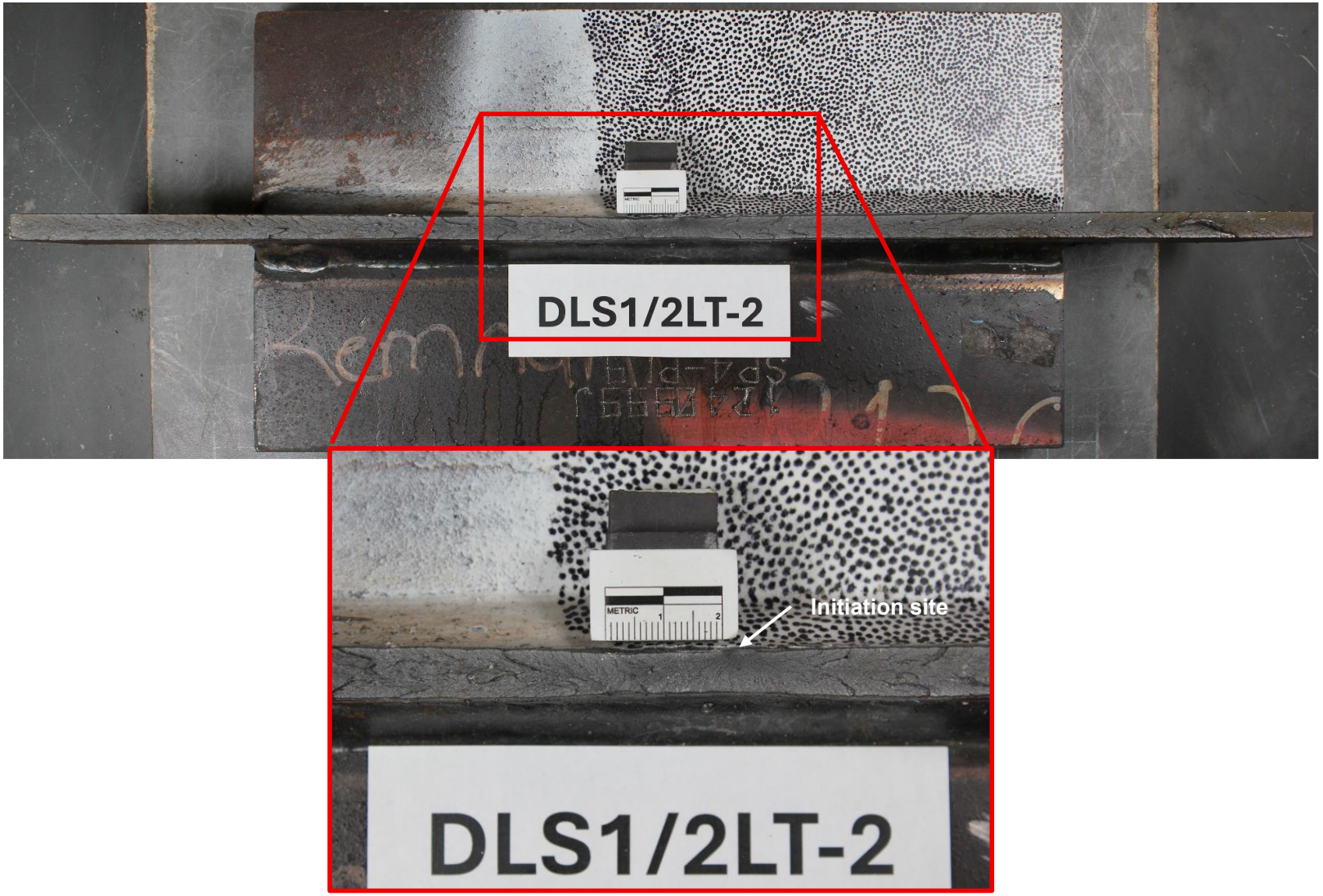

Source: FHWA

Figure 92. Photograph. DLS1/2LT-2: transverse-stiffener side of fracture.

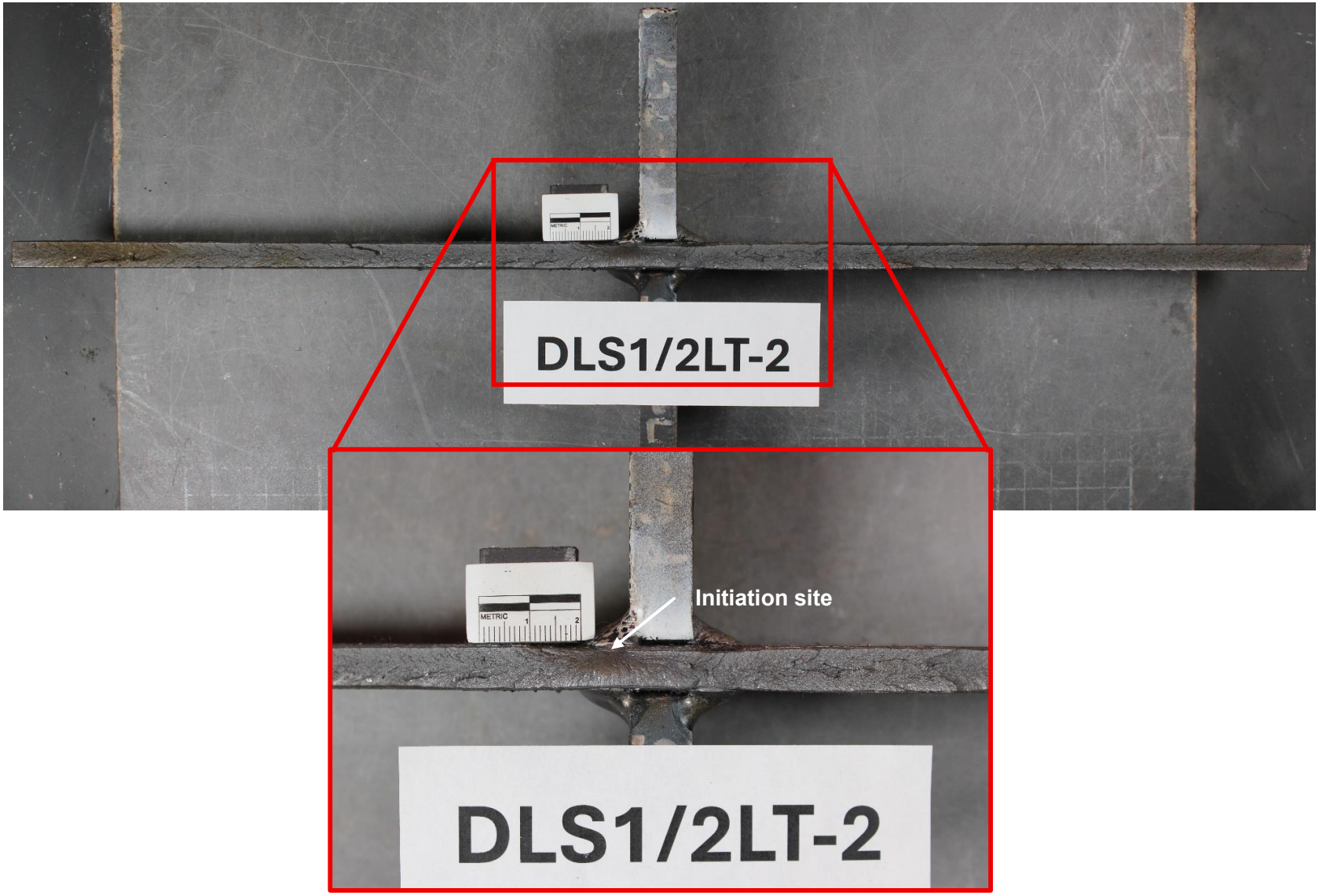

Source : FHWA

Figure 93. Photograph. DLS1/2LT-2: opposite fracture face.

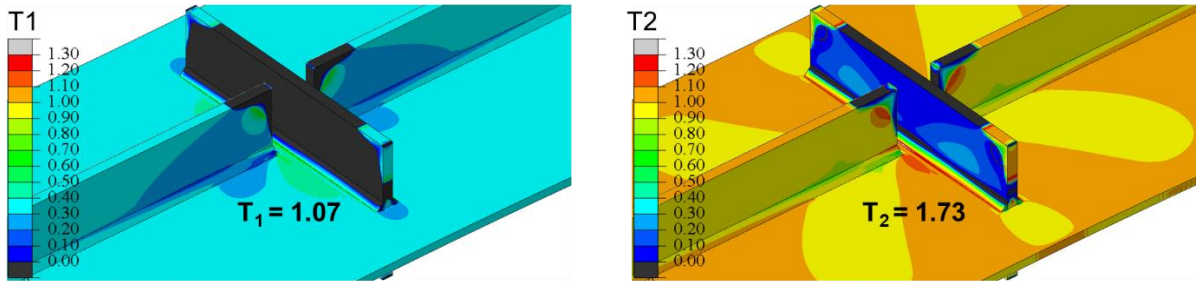

(a) (b)

Source: FHWA.

Figure 94. Illustration. FEA results for DLS1/2LT-1 subjected to fracture load $P_{fracture}$ = 305 kips.

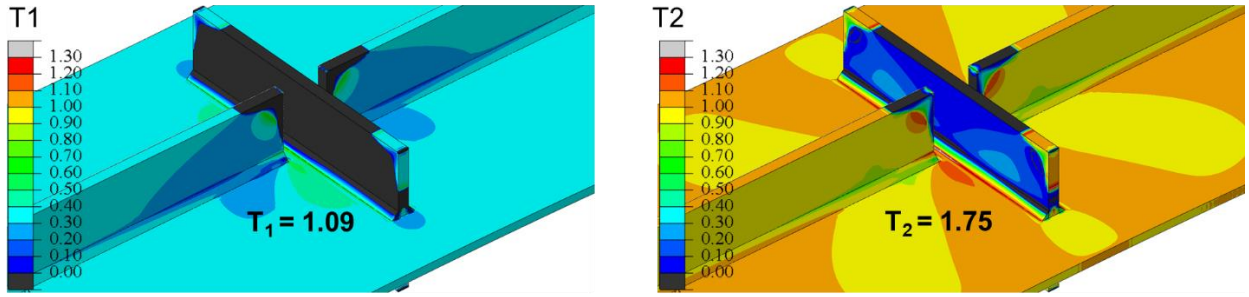

(a) (b)

Source: FHWA.

Figure 95. Illustration. FEA results for DLS1/2LT-2 subjected to fracture load $P_{fracture}$ = 330 kips.

6.3.2.5 Specimen DLS1LT-2 and DLS1RT-2

DLS1LT-2 and DLS1RT-2 were both fabricated from the same heat of steel, but were tested at different temperatures. DLS1LT-2 was soaked at -60 °F and was at -35 °F at the time of fracture. DLS1RT-2 was tested at room temperature and was at 74 °F at time of fracture. The specimens failed at similar load levels despite the temperature difference: 348 kips for DLS1LT-2 and 321 kips for DLS1RT-2.

Top views of broken specimens DLS1LT-2 and DLS1RT-2 are seen in Figure 96 and Figure 100, respectively. Fracture in DLS1LT-2 appears to have initiated from two locations on the top of the plate, at both longitudinal weld terminations in quadrants III and IV where the as-built CRG values were 0.836 inches and 0.785 inches, respectively. These two initiation sites are identified in Figure 98 and Figure 99. The fracture in DLS1RT-2 was a pop-in fracture that self-arrested, the extent of which is identified in Figure 102 and Figure 103. Following pop-in fracture, loading continued until complete failure of the specimen was achieved. The failure surface of DLS1RT-2 presents as an inclined shear surface, even in the location of the pop-in fracture, precluding exact determination of the initiation site, as well as the identification of the extent of the pop-in. It is likely fracture initiated from one of the longitudinal weld terminations, possibly on the top of the plate in quadrant III. Due to this uncertainty no initiation sites are identified in Figure 102 or Figure 103.

Figure 104 and Figure 105 show the output for T_1 and T_2 from finite element models of specimens DLS1LT-2 and DLS1RT-2, respectively. The models were constructed using the same meshing techniques and nonlinear materials used in the parametric study described in Chapter 4, and they were loaded to experimentally-observed fracture loads of 348 kips and 321 kips, respectively. The values denoted in the figures for T_1 and T_2 are maxima, and both occurred at the termination of the longitudinal stiffener weld.

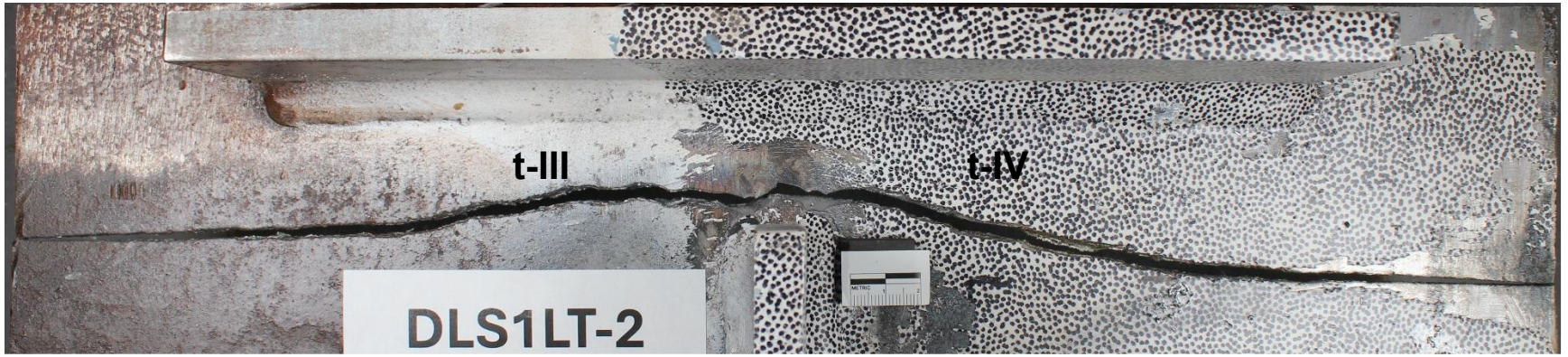

Source: FHWA

Figure 96. Photograph. DLS1LT-2: top view of fractured specimen.

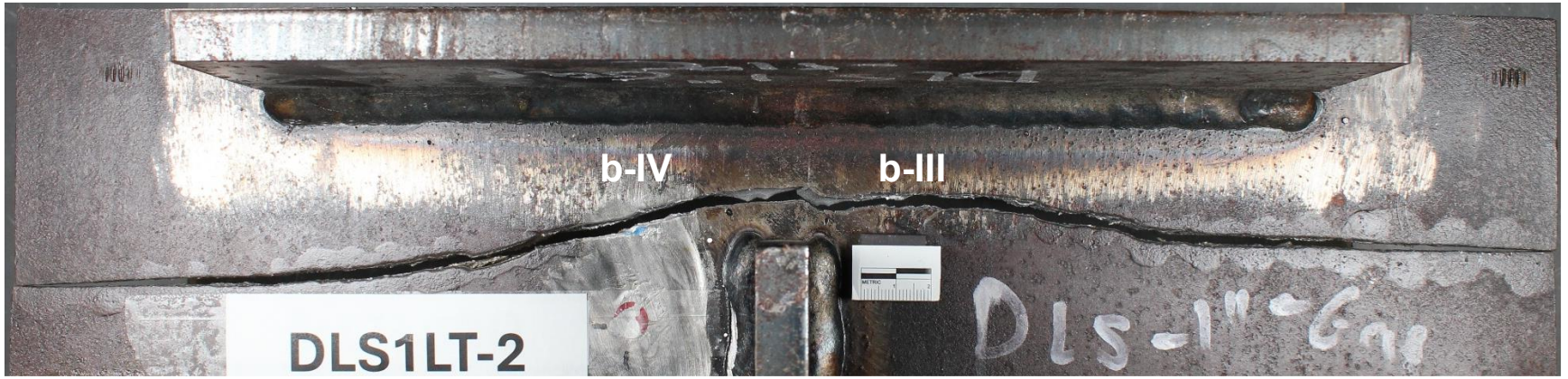

Source: FHWA

Figure 97. Photograph. DLS1LT-2: bottom view of fractured specimen.

Source: FHWA

Figure 98. Photograph. DLS1LT-2: transverse-stiffener side of fracture.

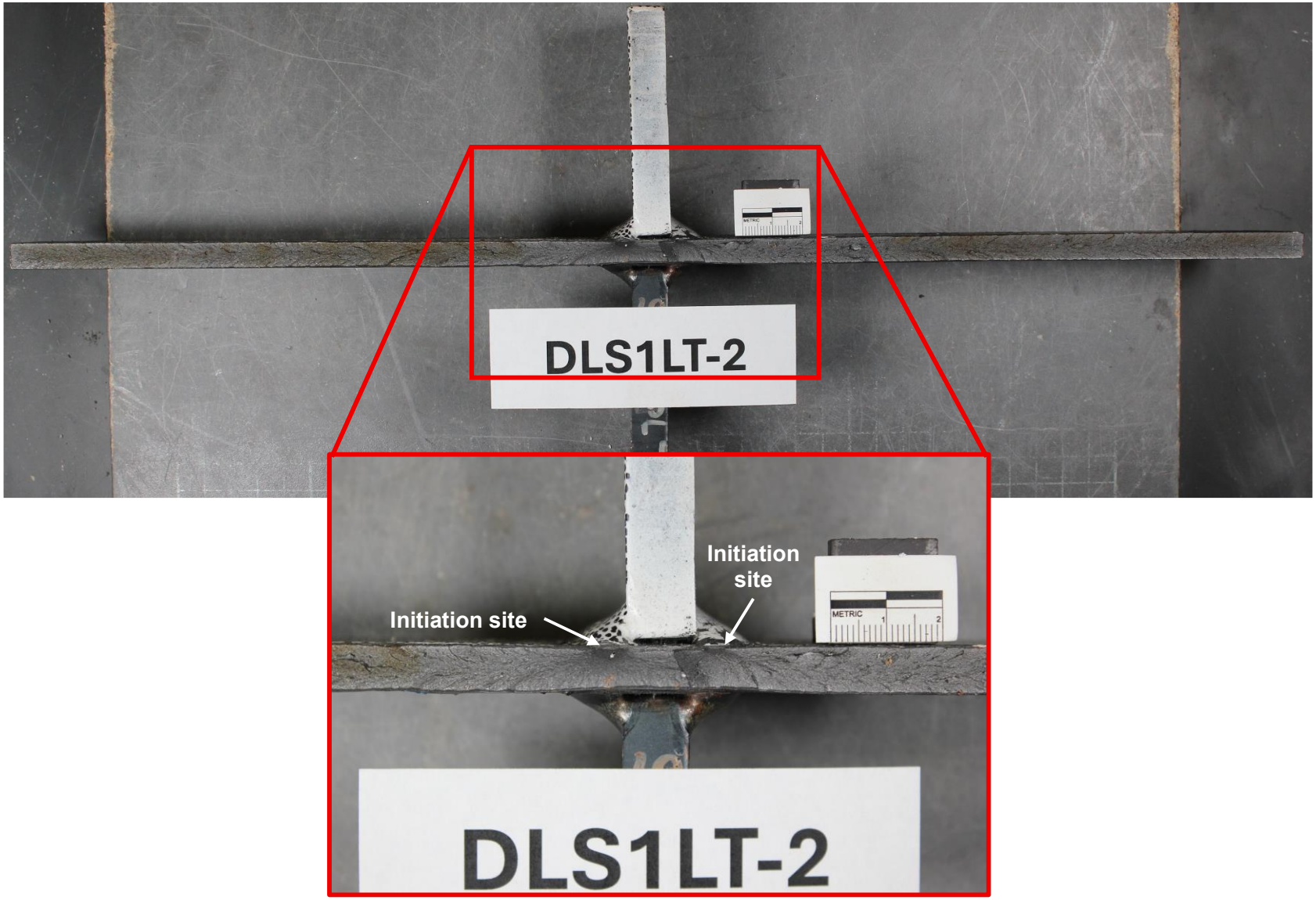

Source: FHWA

Figure 99. Photograph. DLS1LT-2: opposite fracture face.

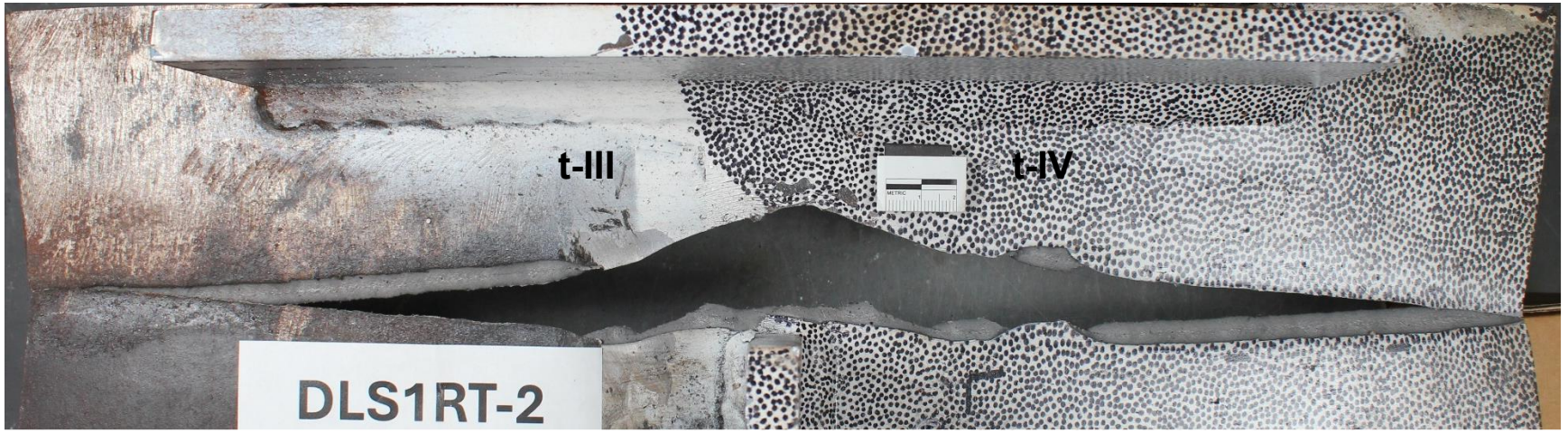

Source: FHWA

Figure 100. Photograph. DLS1RT-2: top view of fractured specimen.

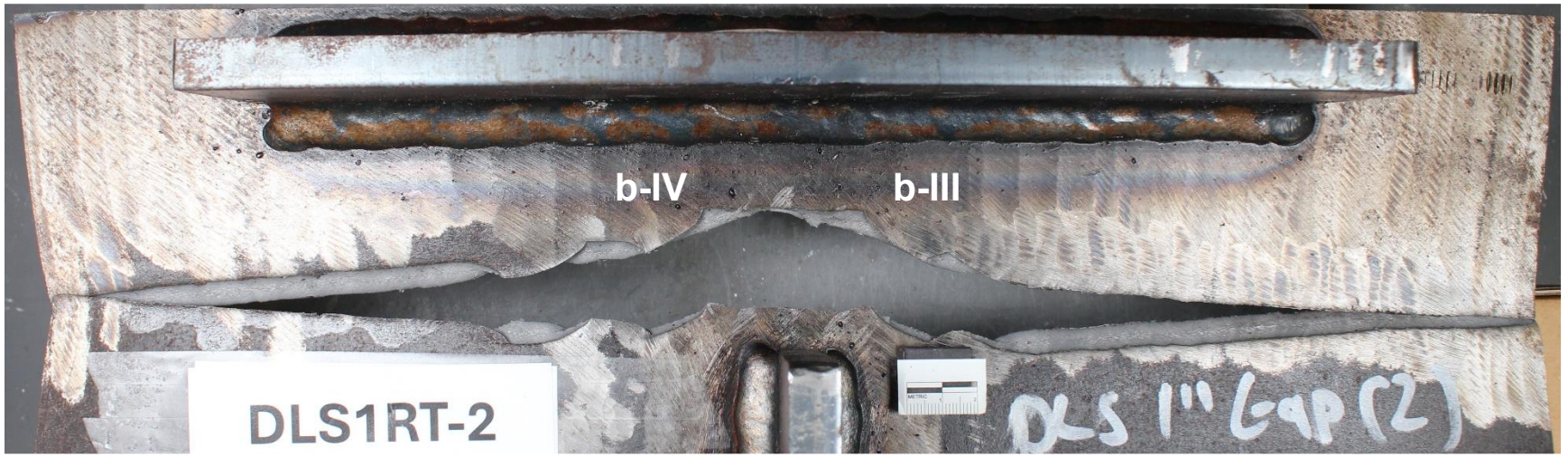

Source: FHWA

Figure 101. Photograph. DLS1RT-2: bottom view of fractured specimen.

Source: FHWA

Figure 102. Photograph. DLS1RT-2: transverse-stiffener side of fracture.

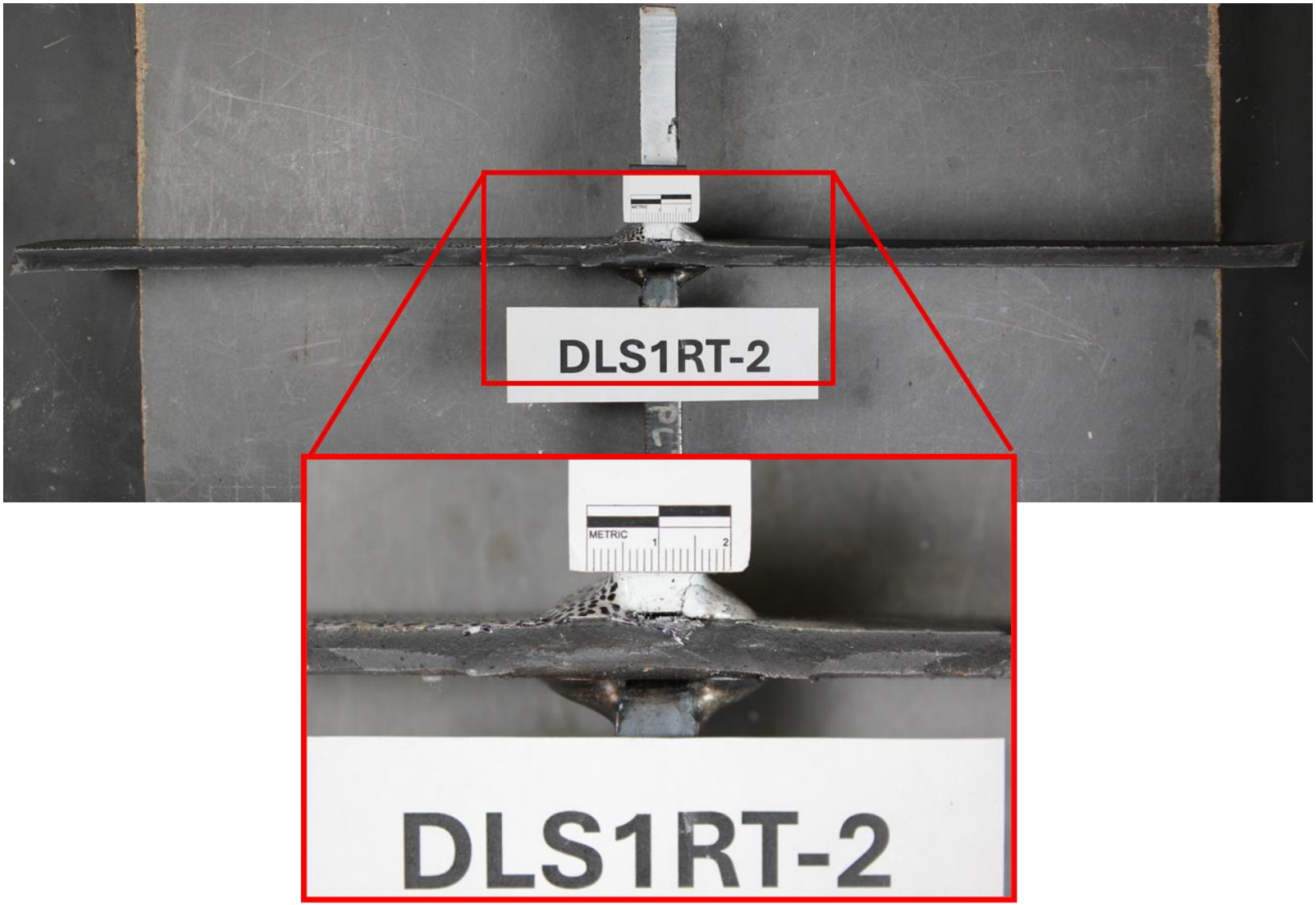

Source : FHWA

Figure 103. Photograph. DLS1RT-2: opposite fracture face.

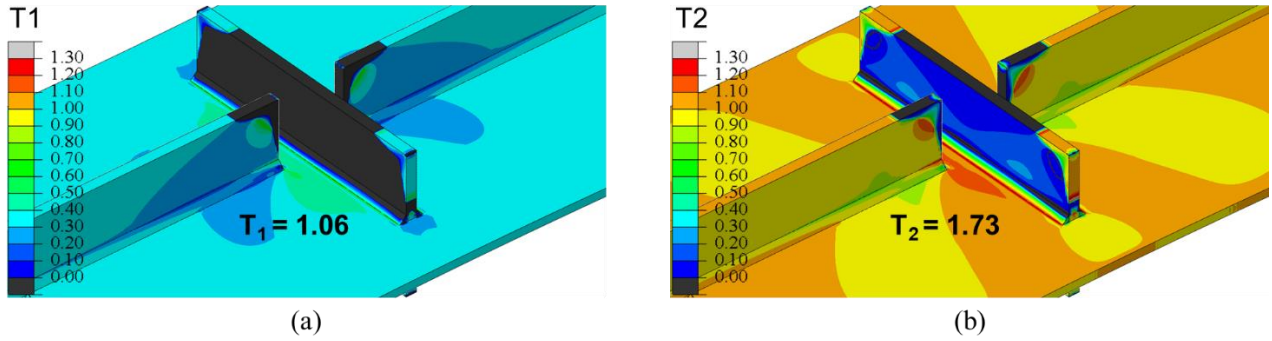

(a) (b)

Source: FHWA

Figure 104. Illustration. FEA results for DLS1LT-2 subjected to fracture load $P_{fracture}$ = 348 kips.

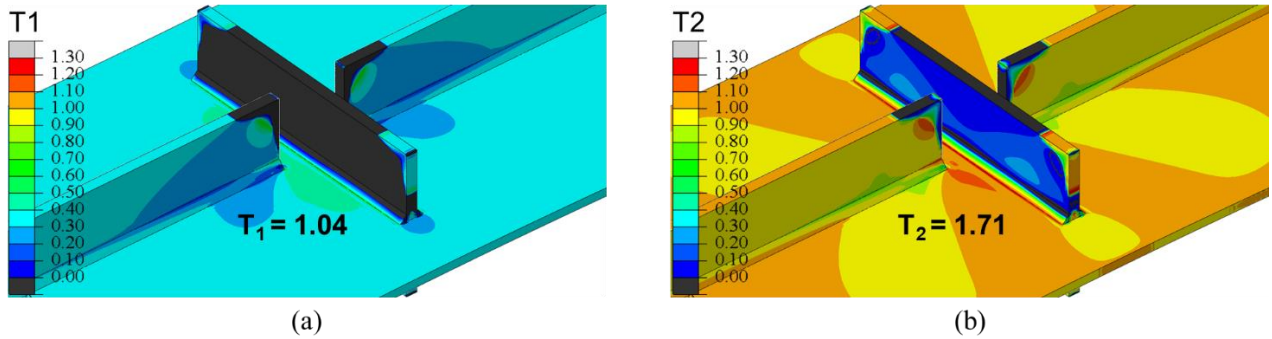

(a) (b)

Source: FHWA

Figure 105. Illustration. FEA results for DLS1RT-2 subjected to fracture load $P_{fracture}$ = 321 kips.

6.4 BEARING STIFFENER DETAIL

Two bearing stiffener specimens were tested: BS0LT-1 and BS1LT-1, pictured in Figure 106. Both were tested at low temperature, soaked at -60 °F before testing. The bearing stiffener specimens were subjected to a static out-of-plane load of 20 kips as an initial loading step. This out-of-plane load was held constant as the specimens were subsequently loaded monotonically in tension along their longitudinal axis. The load-deformation records for BS0LT-1 and BS1LT-1 are presented in Figure 107. Neither specimen experienced fracture; they were each loaded until bearing failure at the steel pins was apparent, at which point the test was stopped.

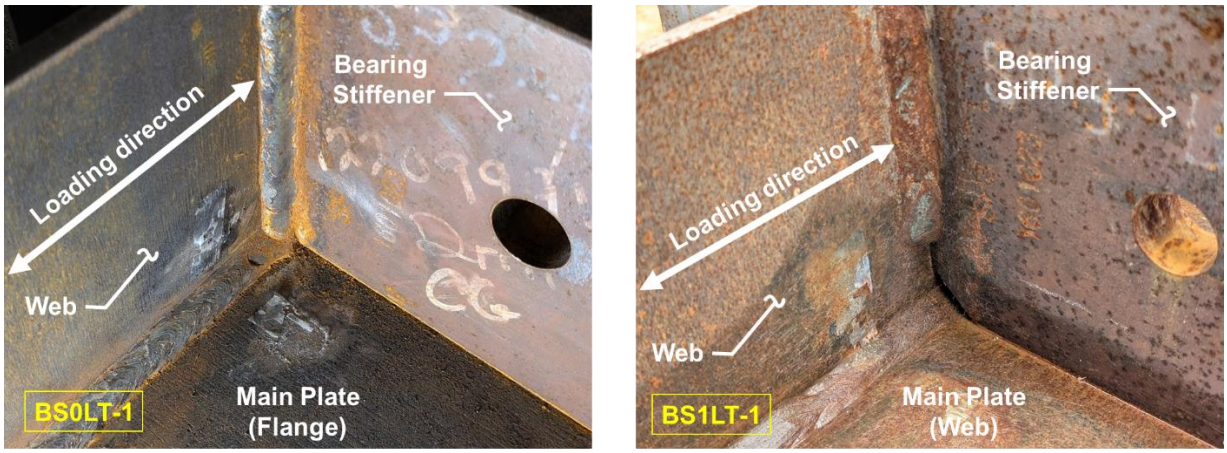

(a) (b)

Source: FHWA.

Figure 106. Photograph. View of bearing stiffener details: (a) no gap, *BS0LT-1*; (b) 1" gap, *BS1LT-1*.

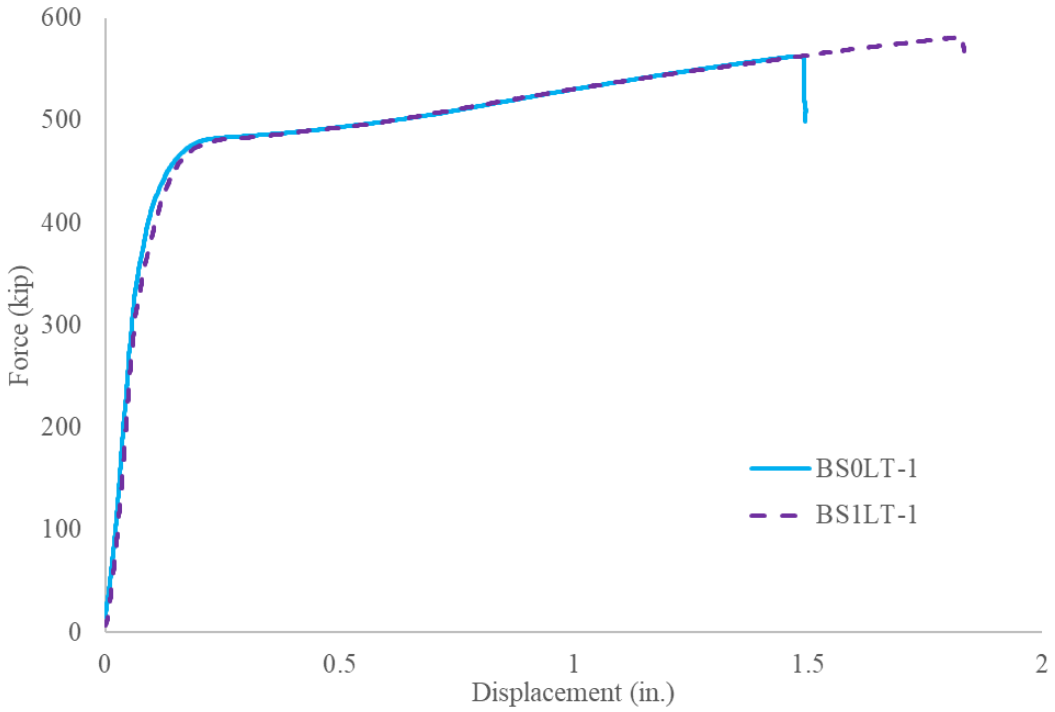

Source: FHWA.

Figure 107. Graph. Load-displacement records for bearing stiffener specimens.

Table 6-2 presents a summary of experimental results for BS0LT-1 and BS1LT-1. For both specimens the comparison between Ro2 and DIC strains agree reasonably well, lending confidence to the DIC strain measurements.

Figure 108 presents the DIC results for strain in the longitudinal direction, ε_1. The DIC measurements show a relatively uniform strain profile along the welds between the bearing stiffener and the web and between the bearing stiffener and the flange, with no isolated severe hot spots.

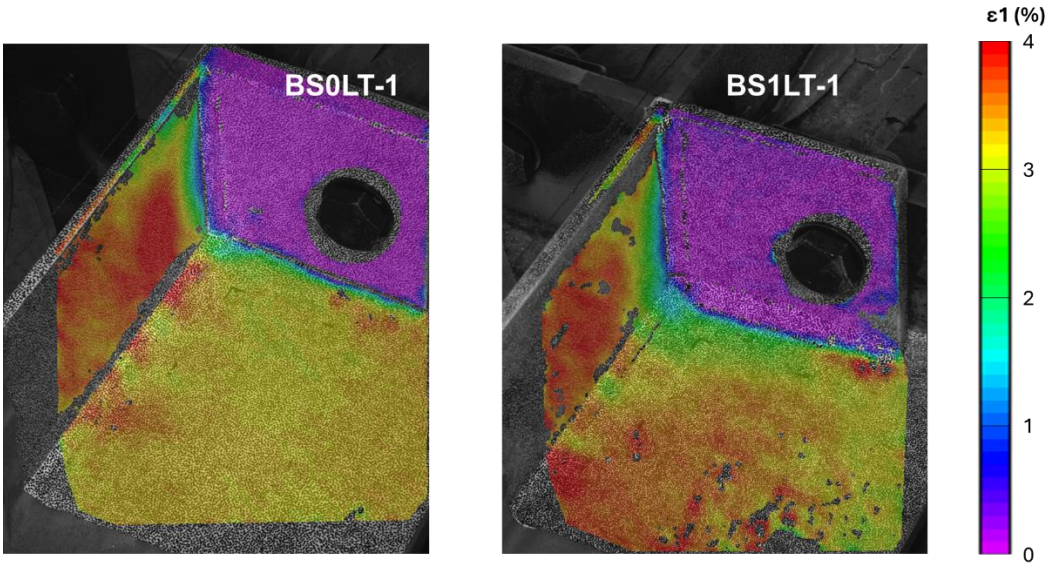

Source: FHWA.

Figure 108. Photograph. Strains at maximum applied load.

6.5 CONNECTION PLATE DETAILS

Four connection plate details were tested: CP0LT-1, CP0LT-2, CP1LT-1, and CP1LT-2 (Figure 109). This suite of four specimens allowed for a comparison of detailing practice (clipped connection plate versus welded through the corner). All four connection plate specimens were tested at low-temperature and were soaked at -60 °F before testing began.

All four specimens were initially loaded with a static out-of-plane load before the specimen was loaded in tension along its longitudinal axis. CP0LT-1 and CP1LT-1 were subjected to an initial out-of-plane load of 20 kips and CP0LT-2 and CP1LT-2 were subjected to an initial out-of-plane load of 30 kips.

The reader may note the additional hole drilled in CP1LT-2 visible in Figure 109; the hole placement drilled by the fabricator was incorrect, so a field correction was made in the KU laboratory to ensure the same out-of-plane loading profile as for the other specimens. It did not affect specimen performance.

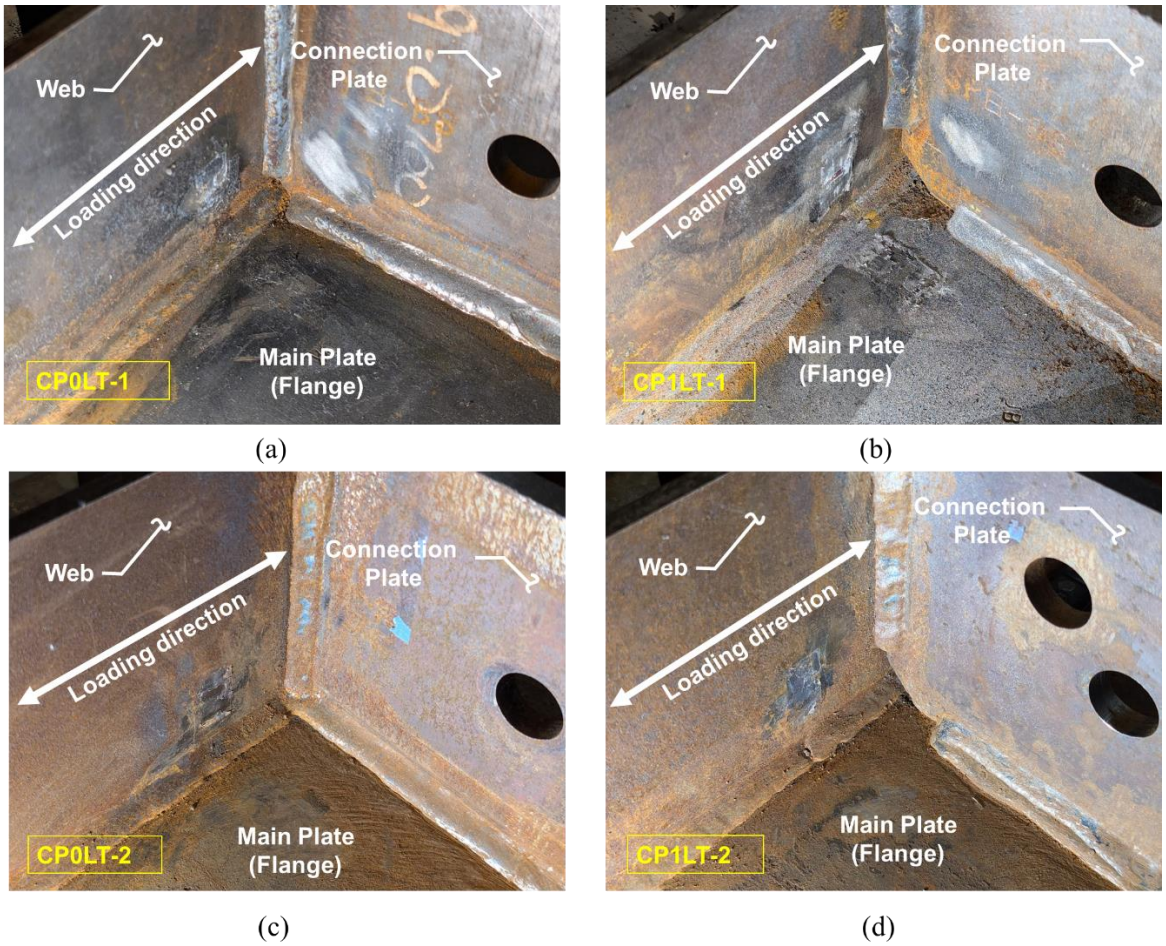

Source: FHWA.

Figure 109. Photograph. Connection plate detail: (a) *CP0LT*-1; (b) *CP1LT-1*; (c) *CP0LT-2*; (d) *CP1LT-2*.

The load-deformation records for the connection plate specimens are shown in Figure 110. All four specimens failed in bearing at the steel pins at the specimen ends; none experienced fracture. Therefore, each of the four tests was stopped when bearing failure was apparent.

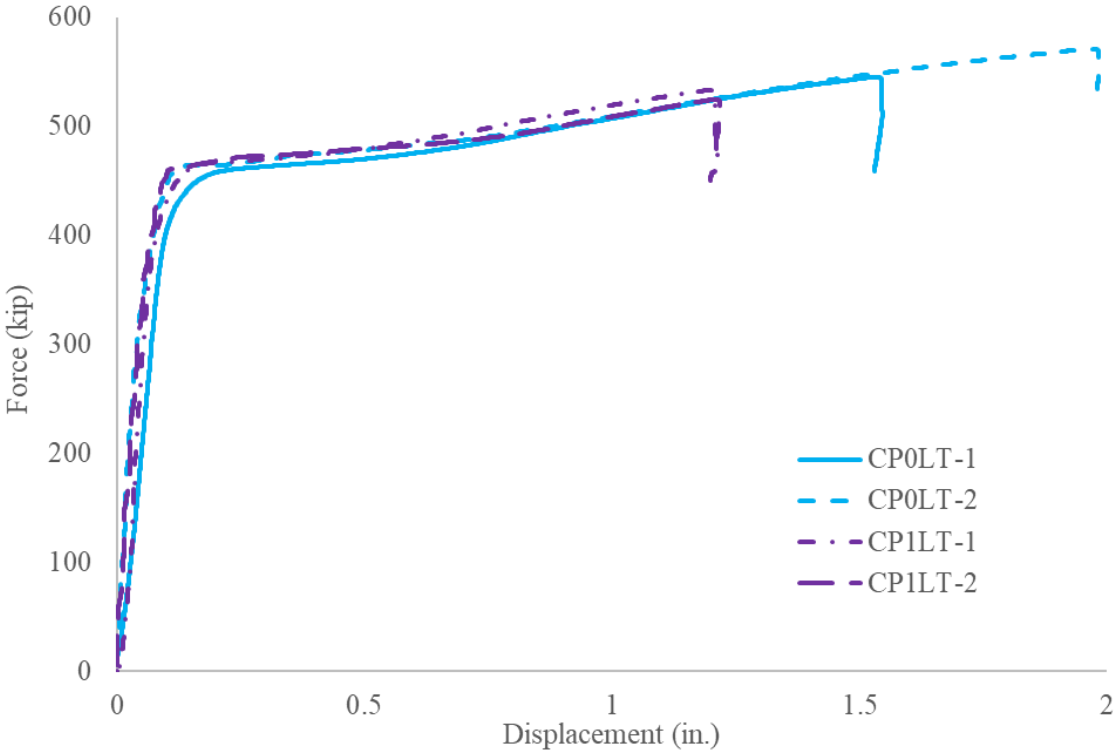

Source: FHWA.

Figure 110. Graph. Load-displacement records for connection plate detail specimens.

Table 6-2 presents the summary of experimental results for the connection plate specimens. A good match is noted between the strain results from the Ro2 gauge and the DIC measurement at the comparable location.

Figure 111 presents the DIC strain fields at a load corresponding with 55%F_y, and Figure 112 shows the DIC strain fields for the connection plate specimens at the point of maximum load. Note that the DIC coating on CP1LT-2 failed before the point of maximum load, and the coating on CP0LT-2 was in the process of failing. Nonetheless, a valuable comparison can be made between CP1LT-1 and CP0LT-1, which shows a very similar strain distribution between the two detailing practices. For both specimens, there are no large isolated hot spots, and the strain distribution is relatively uniform at the connection plate welds.

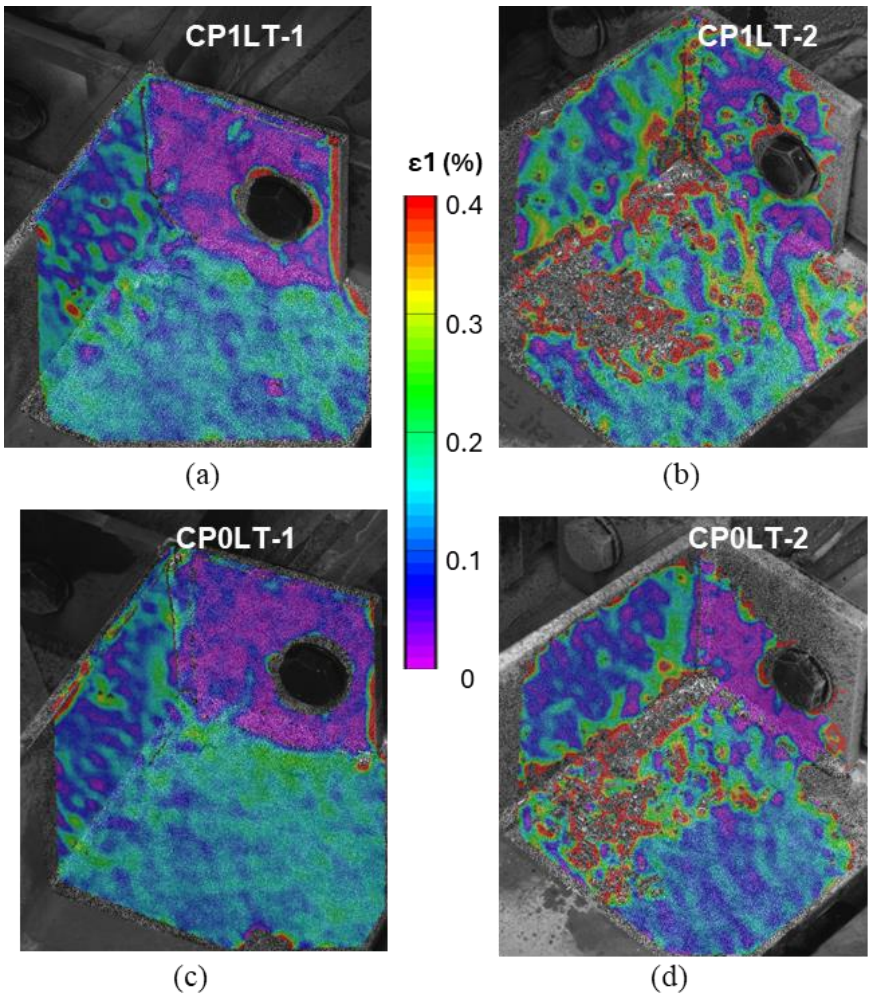

Source: FHWA.

Figure 111. Photograph. Strains at 55%F_y: (a) CP1LT-1; (b) CP1LT-2; (c) CP0LT-1; (d) CP0LT-2.

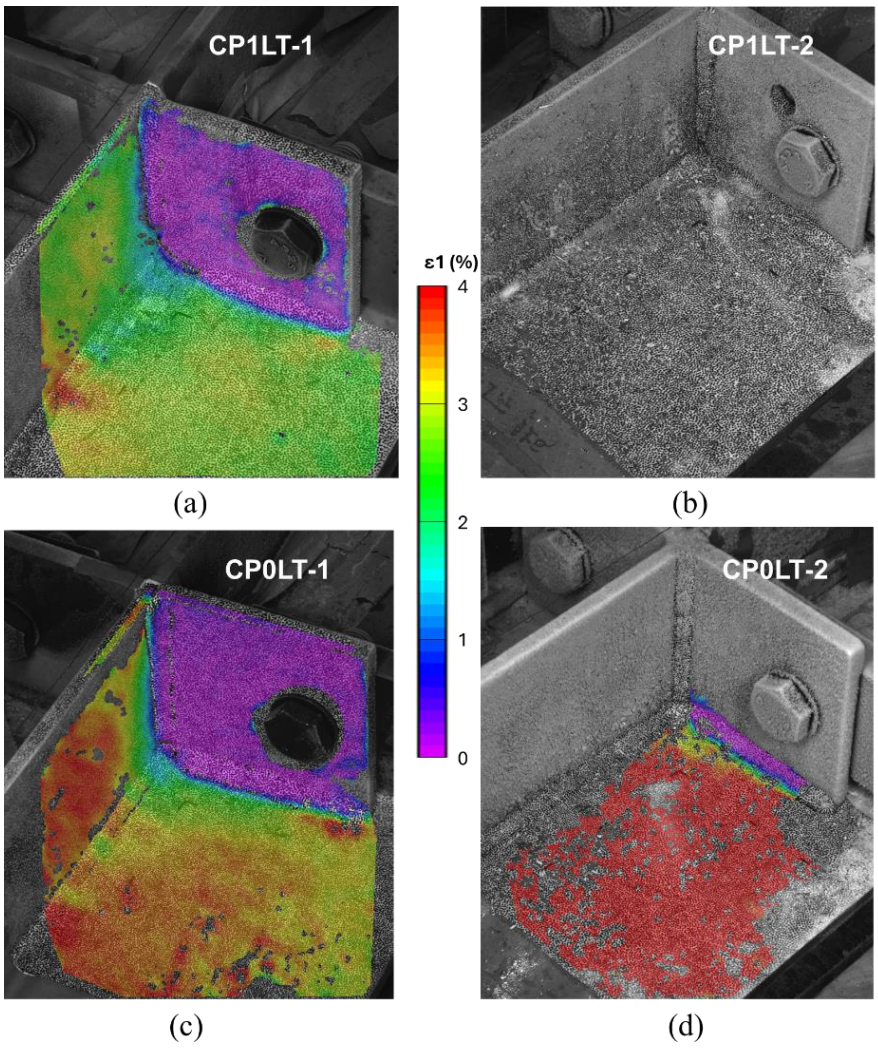

Source: FHWA.

Figure 112. Photograph. Strains at maximum applied loading: (a) CP1LT-1; (b) CP1LT-2; (c) CP0LT-1; (d) CP0LT-2.

6.6 DISCUSSION OF RESULTS

6.6.1 Influence of Constraint-Relief Gap Dimension and Impact Energy on Constraint-Induced Fracture

Figure 113 presents the failure loads for the eight DLS specimens normalized against the nominal yielding capacity of each specimen (P_y = 337.5 kips). The plot also shows the CVN impact energy at the time of fracture, based on the temperature at time of fracture and the average impact energy material characterizations for Batch 1 and Batch 2 steel (Figure 54). Note that Figure 113 presents this information with DLS1/4LT-2 and DLS1/4RT-2 included, and Figure 114 presents the dataset with those specimens excluded. Even excluding DLS1/4LT-2 and DLS1/4RT-2 from consideration, is apparent that there is not an obvious correlation in the data between fracture load and CVN impact energy.

The lack of correlation is particularly apparent when considering DLS1RT-2, which possessed high CVN impact toughness at the time of fracture based on its room-temperature test temperature. However, its fracture load was similar to the fracture load for the other specimen with the same gap size that fractured at low temperature. This finding implies that impact energy (and therefore temperature) does not play a major role in susceptibility to CIF, at least for the DLS geometry. The key difference between these specimens and their counterparts tested at low temperatures is that the specimens tested at room temperature experienced fractures that self-arrested rather than fully propagating through the specimen cross-section.

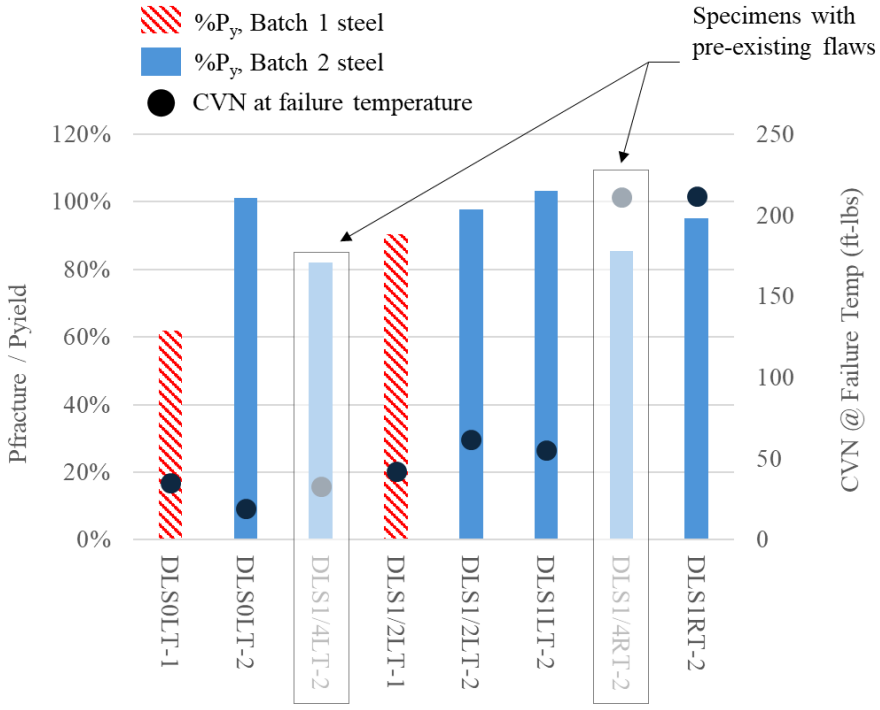

Source: FHWA.

Figure 113. Graph. Failure load and CVN impact toughness at time of fracture for DLS specimens.

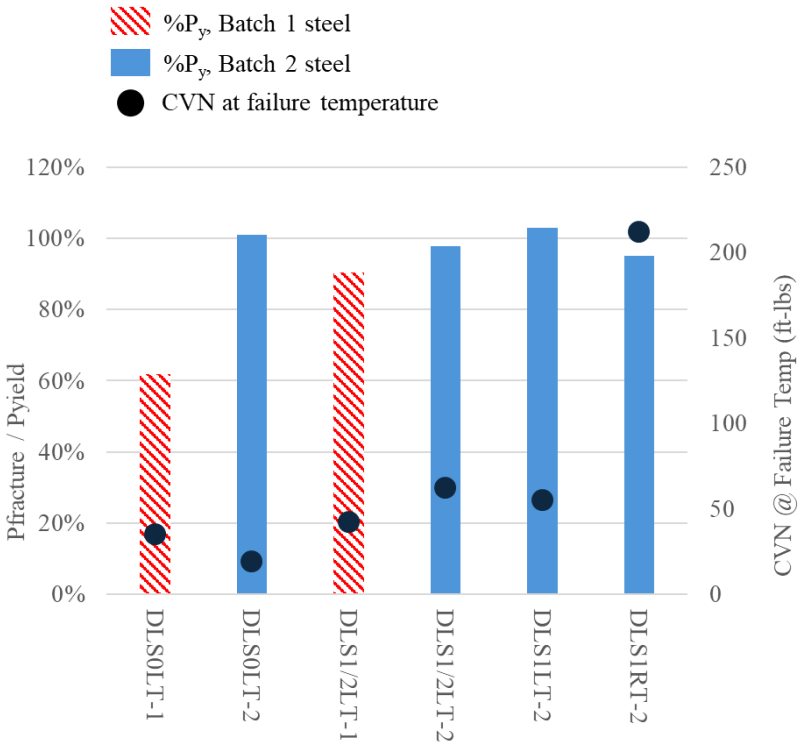

Source: FHWA.

Figure 114. Graph. Failure load and CVN impact toughness at time of fracture for DLS specimens – specimens with pre-existing cracks removed from dataset.

Figure 115 shows the observed relationship between fracture load normalized against the nominal yield strength and nominal constraint relief gap dimension for the DLS specimens. There was large variability in capacity for the two specimens with no constraint-relief gap, with one failing at a load corresponding to just over 60% of material yield strength and the other reaching a load corresponding to more than 100% of yield. While there appears to be a visible trend of increasing capacity with increasing gap size, it should be noted that the DLS1/4LT-2 and DLS1/4RT-2 specimens both had pre-existing flaws, which makes interpretation of their behavior difficult. Additionally, when these data are considered in terms of measured constraint-relief gap dimensions, as shown in Figure 116, this trend is no longer present. Ignoring the DLS1/4LT-2 and DLS1/4RT-2 specimens, which had pre-existing flaws that influenced fracture initiation behavior, all specimens with a constraint-relief gap greater than 0 inches exhibited capacities exceeding 90% of material yield strength. Even the DLS1/4LT-2 and DLS1/4RT-2 specimens, which had actual constraint-relief gaps less than ¼ in. and pre-existing flaws, were able to surpass loads corresponding to 80% of material yield strength. These results indicate that any size constraint-relief gap greater than 0 inches reduces susceptibility to constraint-induced fracture.

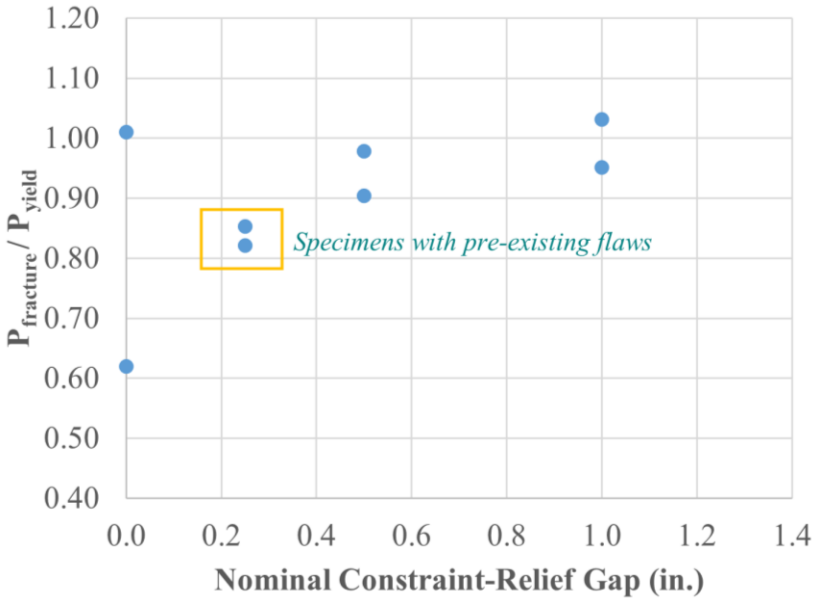

Source: FHWA.

Figure 115. Graph. Fracture load versus nominal constraint-relief gap dimension for DLS specimens.

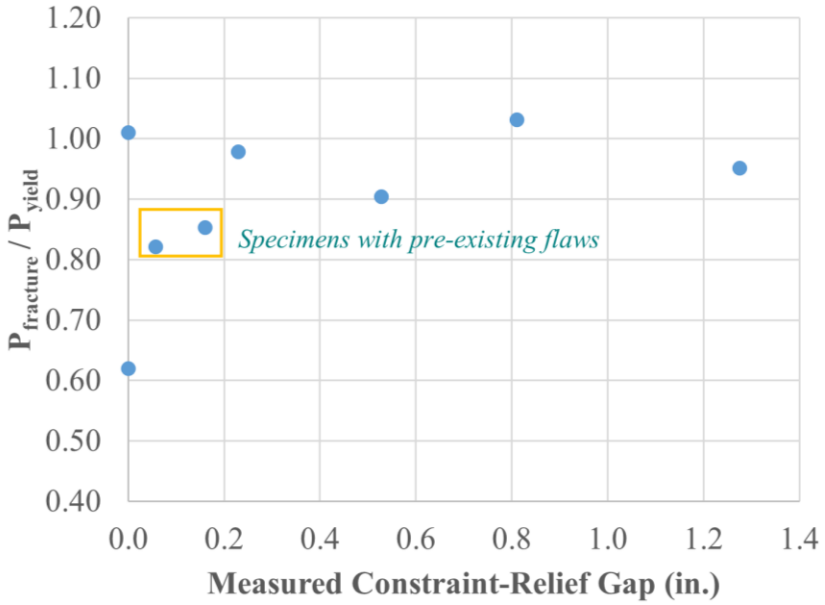

Source: FHWA

Figure 116. Graph. Fracture load versus measured constraint-relief gap dimension for DLS specimens.

Figure 117 presents normalized fracture load against CVN impact energy based on the temperature of the detail at the time of fracture. If CIF resistance correlated with CVN impact energy, one would expect to see a positive relationship in Figure 117 for a given constraint-relief gap. Lines have been added between data points representing specimens with the same nominal constraint-relief gap, and there is no discernable influence of CVN impact energy on CIF performance. This is a surprising and counterintuitive finding.

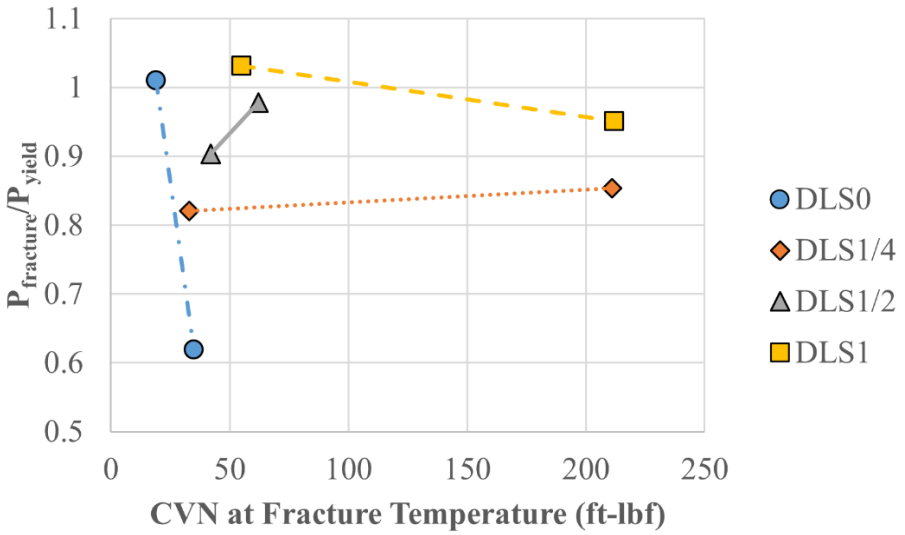

Source: FHWA.

Figure 117. Graph. Fracture load versus CVN impact energy for DLS specimens.

6.6.2 Summary of Triaxiality Factors for Specimens

A finite element model was created for each of the specimens using the meshing techniques and nonlinear materials described in Chapter 4, and each model was executed at the load level corresponding to the experimentally observed fracture load (DLS specimens) or the maximum-applied load (DTS, BS, and CP specimens).

Table 6-4 presents the values of T_1 and T_2 computed from each of the specimen models, along with maximum load, corresponding percent of yield strength, and indication of whether the specimen fractured. Note that models were constructed using nominal constraint-relief gap dimensions rather than as-built dimensions.

Table 6-4. Summary of experimental results for DLS specimens.

Specimen Name	Max load (kips)	%P_y	Fracture?	Computed T_1	Computed T_2
DTS0LT-1	464	137%	N	0.62	1.29
DTS1/2LT-1	452	134%	N	0.62	1.29
DLS0LT-1	209	62%	Y	1.65	2.36
DLS0LT-2	341	101%	Y	1.83	2.54
DLS1/4LT-2	277	82%	Y*	1.08	1.72
DLS1/4RT-2	287	85%	Y*	1.09	1.74
DLS1/2LT-1	305	90%	Y	1.07	1.73
DLS1/2LT-2	330	98%	Y	1.09	1.75
DLS1LT-2	348	103%	Y	1.06	1.73
DLS1RT-2	321	95%	Y*	1.04	1.71
BS0LT-1	562	125%	N	1.04	1.53
BS1LT-1	581	129%	N	1.63	2.20
CP1LT-1	533	118%	N	0.65	1.27
CP1LT-2	525	117%	N	0.81	1.37
CP0LT-1	545	121%	N	0.69	1.35
CP0LT-2	571	127%	N	0.68	1.35

* Indicates pop-in fracture

Figure 118 shows the T_1 and T_2 values extracted from the DLS specimen models. Given that each of the DLS specimens experienced fracture in experimental testing, the values for T_1 and T_2 in Figure 118 could be interpreted as critical magnitudes that corresponded to actual fracture occurrence in these specimens. It is interesting that the values for T_1 and T_2 are not constant for all the specimens, implying that there may not be a single limiting value for either T_1 or T_2 that could be used to predict fracture. However, the results do imply that the DLS specimen is susceptible to CIF when T_2 exceeds 1.7 or T_1 exceeds 1.0.

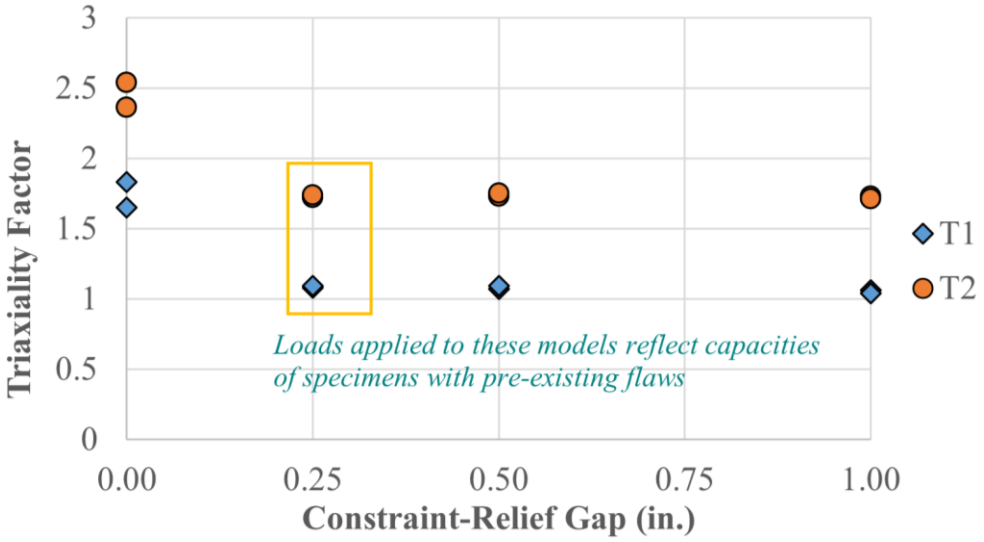

Source: FHWA.

Figure 118. Graph. Computed T_1 and T_2 at experimentally-observed failure loads for DLS specimens.

The range of computed T_2 for the DLS specimens, all of which failed, was approximately 1.7-2.5. For both DTS specimens, neither of which failed, the computed T_2 was approximately 1.3. If failure propensity can be predicted by T_2 alone, this finding implies that failure should occur when T_2 is somewhere between 1.3 and 1.7. However, this breaks down when considering the values computed for T_2 for specimen BS1LT-1, which saw the highest applied load of any specimen (581 kips), and had a computed value of T_2=2.2 at that load. This value for T_2 is well within the range of T_2 values experienced by the DLS specimens that failed.

However, consider the data presented in Figure 119. Here the values for T_2 computed at each specimen's maximum load are normalized against the level of load at which they failed ($\%P_y = P_{fracture}/P_{yield}$). Looking at the data this way captures the fact that one specimen experiencing a T_2 value of, say, 2.0 at a load equal to 60%P_y is worse than a different specimen experiencing T_2=2.0 at a load equal to 120%P_y. In Figure 119, there is a transition between specimens that fractured and those that did not at a $T_2/\%P_y$ value of approximately 1.6.

Note: The reader is cautioned not to use the descriptive $T_2/\%P_y$ inequality for design. This point can be illustrated by imagining a scenario in which an engineer is attempting to limit $T_2/\%P_y < 1.6$. In a design or retrofit, it would make more sense to consider the inequality in terms of stress, $T_2/\%F_y < 1.6$. Assuming a detail in a bridge could be expected to be loaded to a nominal stress equal to $0.55F_y$, this limit would suggest that T_2 should be held to less than 0.88. Based on all the ranges of computed T_2 at various load levels throughout this research, this is unlikely to be possible and doesn't make good sense. The reason this is not sensical is that T_2 does not start at zero with low load; it describes a ratio of maximum principal stress against the von Mises stress.

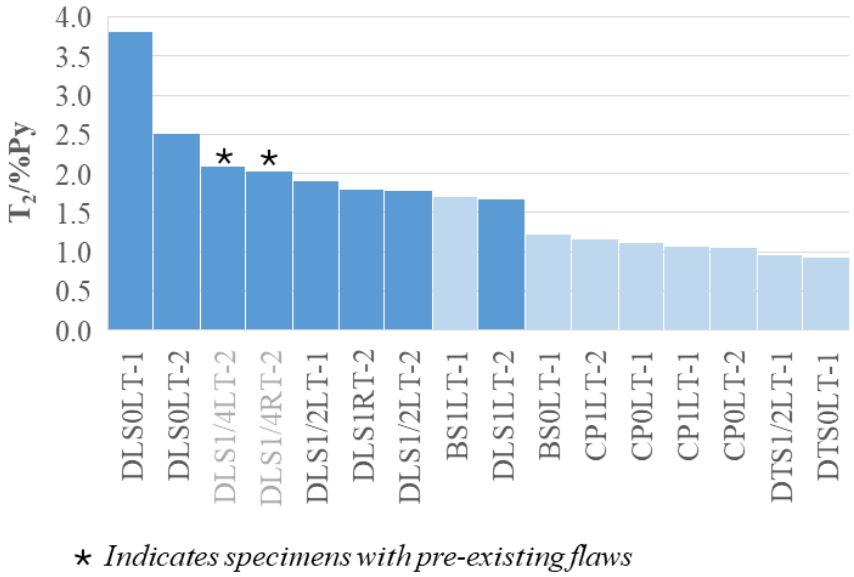

Source: FHWA.

Figure 119. Graph. Normalized T_2 for all tested specimens.

The behavior shown in Figure 119 is further explored in Figure 120, which presents $T_2/\%P_y$ as a function of constraint-relief gap dimension. Presenting the data for all specimens together in Figure 120 takes some liberties with how constraint-relief gap dimensions are treated. Here, the clips in CP and BS details are presented as 1-inch constraint-relief gap dimensions, even though the clip is very different than the gap in a DLS or DTS specimen. Nonetheless, it is helpful to present the data together to examine for trends. The data in Figure 120 do show a clear difference in $T_2/\%P_y$ between the DLS and other specimens tested, with the exception of BS1LT-1.

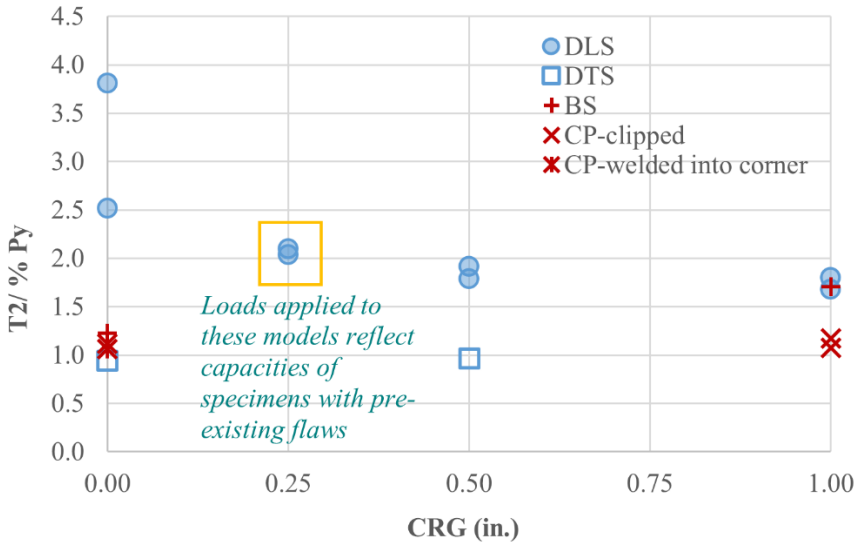

Source: FHWA.

Figure 120. Graph. Normalized T_2 for all tested specimens as a function of nominal constraint-relief gap dimension.

CHAPTER 7 - CONCLUDING REMARKS

This report has described a study characterizing the susceptibility of structural stiffener details in steel bridges to constraint-induced fracture, for cases including: (1) thick bearing stiffeners; (2) different constraint-relief gap distances between intersecting structural components; and (3) continuous welding at the intersection of the flange-web-connection plate.

The research included a suite of nonlinear parametric finite element analyses and a suite of 16 experimental tension tests loaded to failure.

The following observations and conclusions have been reached from the parametric finite element analyses:

1. The DTS detail is not sensitive to changes in local geometry, assessed in terms of triaxiality.

2. Magnitudes for T_1 and T_2 are much lower for the DTS detail than for the DLS detail, indicating a lower susceptibility to constraint-induced fracture for the DTS detail.

3. The three connection plate details studied exhibited similar states of triaxiality when there was no out-of-plane force. For the case with no out-of-plane loading, the magnitude of triaxiality was similar to that for the DTS detail, indicating that susceptibility of all three connection plate details to constraint-induced fracture in the absence of out-of-plane loads is small, on the basis of a good practical performance record of discontinuous transverse stiffeners.

4. In all three connection plate details, there was a large increase in triaxiality with the introduction of out-of-plane loading, for both positive and negative bending cases. Some of these magnitudes were similar to those computed for the discontinuous longitudinal stiffener detail with no constraint relief gap ($T_1 = 1.5$ and $T_2 = 2.1$). This indicates the connection plate details may have elevated susceptibility to constraint-induced fracture in the presence of significant out-of-plane loads, on the basis of a poor practical performance record of details like the discontinuous longitudinal stiffener.

5. Comparing triaxiality in the connection plate details, the data suggest that there is not an increased risk of constraint-induced fracture in transitioning from current or historic connection plate details to the newly-proposed connection plate detailing practice in which welds are allowed to meet at a common point at the connection plate-web-flange junction.

The following observations and conclusions have been reached based on the experimental tests of 16 tension specimens loaded to failure:

4. All the DLS specimens experienced brittle fracture during tension loading. Fracture occurred even in tests conducted at room-temperature. Test results did not appear to be correlated with material impact energy, suggesting an insensitivity to temperature at time of fracture.
5. For DLS specimens, a constraint-relief gap of any size reduces susceptibility to CIF, although there is no clear correlation between constraint relief-gap size and CIF resistance. There is a high degree of variability in CIF behavior in DLS details with no constraint-relief gap, with the no-gap specimens reaching fracture loads corresponding to just over 60% of yield up and over 100% of material yield strength. Any gap size at all provided relief from CIF susceptibility, with all specimens fabricated with a constraint-relief gap surpassing loads corresponding with 90% of material yield strength. Even specimens that had pre-existing flaws and constraint-relief gaps of less than ¼ inch were able to exceed loads corresponding to 80% of the material yield strength.
6. All the DLS specimens exceeded an applied load of $0.55F_y$ (nominal design stress level) before fracturing, with the lowest load at fracture corresponding to $0.62F_y$ and a zero-gap geometry. All

specimens having at least a ¼-inch gap exceeded a load corresponding with $0.80F_y$ before fracturing.

7. The DLS specimens that fractured had T_2 values between 1.7-2.5 immediately before fracture, based on finite element models of the specimens executed at the experimentally-observed maximum load. The fact that there was a range of T_2 values at fracture suggests that there are other factors not reflected in T_2 that contribute to CIF. It also suggests that if there is a useable T_2 threshold for the DLS specimens corresponding with fracture, that it is less than 1.7.
8. None of the DTS specimens fractured under tensile loading. All the DTS specimens were loaded well above nominal yield. This finding reinforces current practice in recommending the DTS detail when a conflict exists between a longitudinal and transverse element, and is further corroborated by results from the parametric finite element model suite.
9. None of the bearing stiffener specimens fractured under tensile loading. Both bearing stiffener specimens were loaded well above nominal yield and had out-of-plane forces acting on the stiffeners equal to 20 kips. This finding suggests low susceptibility to CIF for the bearing stiffener details studied. However, the experimental interpretation requires a little nuance – the T_2 values corresponding to the no-gap and 1-inch clipped bearing stiffener details, respectively, were 1.5 and 2.2, which were the largest T_2 values computed outside of the suite of DLS specimens. The fact that the 1-inch clipped bearing stiffener had an elevated T_2 value that corresponded with failure in other specimens raises unresolved questions as to whether there are other as-of-yet unquantified predictors of CIF not captured here.
10. None of the connection plate specimens fractured, although all four of the connection plate specimens were loaded well above nominal yield. The connection plate specimens also had large out-of-plane forces acting on the stiffeners at a magnitude of 20 kips or 30 kips. This experimental finding suggests low susceptibility to CIF for the connection plate details studied and supports implementation of the CP detail that welds the stiffener directly into the junction of the web/flange.

The following suggestions are offered:

1. Based on the experimental and analytical results, it is suggested that a minimum constraint-relief gap dimension of $^1/_4$-inch be adopted for discontinuous longitudinal attachment/stiffener details currently present in the inventory of steel bridges. Experimental tests showed that the average capacity for specimens with no constraint relief gap (weld toes touching) was lower than that for every other gap size tested. Furthermore, the analytical investigation showed a clear decrease in constraint between a no-gap case and a ¼-inch gap case, which is consistent with the experimental finding. Finally, even specimens with pre-existing flaws and nominal ¼-inch constraint-relief gaps were able to reach applied loads corresponding with stresses above 80% of material yield strength, which is greater than the $75\%F_y$ limit currently allowed by the Manual for Bridge Evaluation (MBE) (AASHTO, 2018).

2. This research supports adoption of the proposed detailing practice for connection plates where practical, in which the connection plate is welded directly into the flange-web junction. Care should be taken to ensure fusion between weldment and base metal, and to avoid the presence of notches or discontinuities in the intersecting weld.

3. Study the performance of other methods of quantifying susceptibility to constraint-induced fracture, beyond the quantities examined here (triaxiality factors, stress, strain) should be considered. Given some surprising findings regarding high triaxiality predictions in bearing stiffener/connection plate details weighed against excellent experimental performance, it is possible that other quantifiable variables exist to further "sharpen the pencil" for constraint-induced

fracture susceptibility prediction. It is specifically suggested to examine stress concentration factor along with triaxiality factor in future work, as a means to capture both constraint and planar discontinuity effects together.

REFERENCES

AASHTO. (2017). AASHTO LRFD Bridge Design Specifications, 8th Edition. Washington, DC: American Association of State Highway and Transportation Officials.

AASHTO. (2018). The Manual for Bridge Evaluation: Third Edition (with interim revisions 2019 & 2020). Washington, DC: American Association of State Highway and Transportation Officials.

ASTM. (2024a). A709: Standard specification for structural steel for bridges. West Conshohocken, PA: ASTM International.

ASTM. (2024b). E23: Standard test methods for notched bar impact testing of metallic materials. West Conshohocken, PA: ASTM International.

Bowman, M. (2002). *Fatigue Behavior of Beam Diaphragm Connections with Intermittent Fillet Welds, Part II: Brittle Fracture Examination of the I-64 Blue River Bridge. Final Report FHWA/IN/JTRP-2001/10-II*.

Coletti, D., Chavel, B., Ream, A., Bennett, C., Connor, R., Frank, K., Grubb, M., Hubbard, F., Medlock, R., Miller, D., & Russo, F. (2021). *Evaluation of Steel Bridge Details for Susceptibility to Constraint-Induced Fracture*. FHWA.

Connnor, R., Kaufmann, E., Fisher, J., & Wright, W. (2007). Prevention and mitigation strategies to address recent brittle fractures in steel bridges. *Journal of Bridge Engineering*, *12*(2), 164-173.

Cooper, J. (2001). ACTION: Hoan Bridge Failure Investigation. *Memorandum. U.S. Department of Transportation, Federal Highway Administration, July 10., Washington DC*.

Ellis, R., Connor, R., Medhekar, M., MacLaggan, D., & Bialowas, M. (2013). Investigation and Repair of the Diefenbaker Bridge Fracture. 2013 Conference of the Transportation Association of Canada, Winnipeg, Canada.

Fisher, J., & Kaufmann, E. (2010). *Fracture at Web Gap of the Iowa I-80 Bridge over the Cedar River (unpublished technical report)*. Wiss, Janney, Elstner Associates, Inc.

Hodgson, I., Sause, R., & Chen, Y. (2018). *Pilot Retrofit Study for the Norman Wood Bridge over the Susquehanna River, Final Report to the Pennyslvania Department of Transportation*. ATLSS.

Mahmoud, H., Connor, R., & Fisher, J. (2005). Finite element investigation of the fracture potential of highly constrained detailed in steel plate members. *Computer-Aided Civil and Infrastructure Engineering*, *20*, 383-392.

Russo, F., Mertz, D., Frank, K., & Wilson, K. (2016a). *Design and Evaluation of Steel Bridges for Fatigue and Fracture – Reference Manual* (FHWA-NHI-16-016). Michael Baker International.

Russo, F., Mertz, D., Frank, K., & Wilson, K. (2016b). *Design and Evaluation of Steel Bridges for Fatigue and Fracture, FHWA Report No. 016*. FHWA.

Schafer, B., Ojdrovic, R., & Zarghamee, M. (2000). Triaxiality and Fracture of Steel Moment Connections. *Journal of Structural Engineering*, *126*(10), 1131-1139.